Engineering Interfacial Effects and Layered Behavior in 2D Materials

Nathan P. Wilson

A dissertation
submitted in partial fulfillment of the
requirements for the degree of

Doctor of Philosophy

University of Washington
2020

Reading Committee:

Xiaodong Xu, *Chair*
David Cobden
Jiun-Haw Chu

Program authorized to offer degree:

Physics

University of Washington

Abstract

Engineering Interfacial Effects and Layered Behavior in 2D Materials

Nathan P. Wilson

Chair of the Supervisory Committee:
Professor Xiaodong Xu
Physics

The rise of two-dimensional (2D) materials over the last one-and-a-half decades can be attributed to two separate reasons. The first is the discovery of new materials with unique properties that derive partially, if not entirely from their low dimensionality, as is the case for 2D Chern insulators. The second is the ability to combine 2D materials together arbitrarily through van der Waals stacking to form custom layered structures with engineered properties. But more than just offering a new knob for controlling materials, van der Waals heterostructures have produced to breakthrough discoveries in basic science, helping us create new electronic phases and explore topology in new ways. Central to producing these effects are the different types of interactions between layers, from the most trivial effects like dielectric screening to more complex interactions like interlayer charge transfer and exchange interactions. Consequently, learning how to control interlayer interactions and predict the physical outcomes they produce has become a key scientific challenge in the 2D materials community.

In this dissertation, several approaches to engineering, controlling, and harnessing the power of interlayer and interfacial effects in various 2D material systems are explored. First, we introduce a new, powerful spectroscopic tool for understanding the effects of quantum confinement on excitons, optically excited and bound electron-hole pairs, in 2D semiconductors, and use it to explore the intricacies of the Hamiltonian of these 2D excitons. We then discuss the novel properties of heterobilayers of 2D semiconductors which host *interlayer* excitons in which the electron and hole reside in opposite layers, and present a simple approach to enhancing the beneficial properties of these interlayer excitons for studying their many-body physics by modifying the interlayer interaction with a tunneling barrier. Finally, we use various optical and spectroscopic probes to investigate a new type of behavior found in layered magnetic van der

Waals materials, layered magnetism, which results from the fundamental anisotropy of the materials. We analyze a simple approach to engineering the interlayer magnetic coupling in such materials, and uncover a deep, underlying connection between the layered magnetic order and the optical excitations in a newly discovered 2D magnetic semiconductor.

Contents

This page left intentionally blank.

List of Figures

Terminology and Abbreviations

3D: Three-dimensional

2D: Two-dimensional

vdW: van der Waals

QW: Quantum well

CQW: Coupled quantum well

PL: Photoluminescence

hBN: Hexagonal boron nitride

TMDC: Transition metal dichalcogenide (typically the four semiconducting TMDCs)

NIR: Near infrared

PC: Polycarbonate

PDMS: Poly-dimethyl siloxane

Si/SiO_2 wafer: A substrate consisting of a doped silicon wafer coated with a layer of SiO_2

AFM: Atomic force microscope/microscopy

VBM [CBM]: Valence [conduction] band maximum [minimum]

FM [AFM]: [Anti-] ferromagnetic

SAF: Synthetic antiferromagnet

IEC: Interlayer exchange coupling

IX: Interlayer exciton

Acknowledgements

It is difficult to overstate my gratitude to Xiaodong and just how lucky I feel for having had the opportunity to learn from my advisor. In fact, it was partly by chance that I came to work in his lab. When hunting for graduate programs, I set out determined to become a cold-atom physicist and had no real experience with condensed matter physics. He introduced himself to me at the UW recruiting dinner and, through sheer enthusiasm, persuaded me to change my entire career direction and join his lab. Whether by fate or by chance, this meeting reshaped my life in myriad positive ways. Xiaodong is a uniquely talented practitioner of professional science. With his limitless creativity, he has conjured from thin air innumerable imaginative ideas for research projects of great scientific value. His remarkable ability to connect with other scientists has spawned countless collaborative projects that have broadened my intellectual horizons and opened many doors for me. His relentless optimism and excitement about my projects have made the long hours in a pitch-black basement lab, no matter how tedious, feel impactful and inspired. As an advisor, he has always prioritized my learning, professional development, and wellbeing above all else. He has helped me unlock my potential as a researcher and leverage my unique skill set to great advantage. He has given me the opportunity to practice the skills I will need in the future as a professional scientist by engaging me with grant writing, presenting at program meetings, and much more. My education under Xiaodong's advisory was more comprehensive and profound than almost any of my peers. I have enjoyed my time in Xu lab immensely and could not have asked for a better experience.

Secondly, it goes without saying that I have benefited greatly from the support and advice of my other committee members, Professors Kai-Mei Fu, Jiun-Haw Chu, David Cobden, Deep Gupta, Boris Spivak, and Daniel Gamelin. Kai-Mei and Dave have been incredible resources whenever I've needed to take a deep dive into authoritative literature on topics outside of my comfort zone. Deep played a huge role in getting me to UW in the first place. Jiun-Haw has given me immense appreciation for the synthesis side of condensed matter physics. Boris's unique insights and deep, intuitive understanding of fundamental physics in solid state systems have bolstered my own theoretical understanding of my work.

I have been fortunate to work with numerous brilliant collaborators over the years, perhaps too many to name in a paragraph, but I want to highlight several who have contributed greatly to

the work within this dissertation. I especially want to thank Scott Crooker and Andreas Stier. Scott is the type of scientist that I would like to be; careful, meticulous, and conscientious. Andreas has really been like a second advisor to me. He helped guide me through my first couple of completed projects and publications and has pushed me to be more creative, more resourceful, and to act decisively. I would like to thank all my collaborators at Columbia University, Xiaoyang Zhu, Xavier Roy, Kihong Lee, Avalon Dismukes, Cory Dean, and En-Min Shih. I would also like to thank the crystal growers who have been instrumental in achieving my scientific goals: Jiaqiang Yan, Michael McGuire, David Mandrus, and Fazel Tafti. Without you, none of this would have been possible.

The members of Xu Lab, past and present, have had a tremendous impact on my life and career. Working with them has been a great pleasure and I owe a great deal to many of them. Pasqual Rivera and Kyle Seyler were amazing mentors. They taught me much of what I know and helped me hone my experimental skills. I sincerely miss coffee walks with Pasqual, and our long discussions about new ideas for devices or experiments. Kyle was a great deskmate and always radiated positivity, and I strive every day to emulate his inexhaustible patience for difficult experiments and finnicky lasers. Bevin Huang, who has been a good friend and colleague throughout grad school, from first year classes and qualifying exams to writing our dissertations, is a stellar scientist and wonderful coworker who can always put a smile on your face. He is always eager to help out, even when it means spending endless hours elbow-deep in the glovebox exfoliating samples. Tiancheng Song and Minhao He are among the most dedicated and resourceful scientists I know, and I can't wait to see what you do in your careers after grad school. To the next generation of students, John Cenker, Kyle Hwangbo, Jordan Fonseca, Eric Anderson, Jiayi Zhu, Jiaqi Cai, and Yinong Zhang, it has been a pleasure to get to know you all and I hope I've been able to pass down to you the techniques and skills you'll need to succeed in your research. Last but certainly not least, I want to thank Essance Ray. Working with you was always a pleasure, and your skill in 2D fabrication is unmatched and was absolutely instrumental in so much of my work. As you are now entering grad school, I know your determination, stellar work ethic, and attention to detail will help you thrive.

Grad school doesn't always leave much time for socialization, but I am lucky to have made some fantastic friends over the last few years. Shua Sanchez is the person in grad school I've

known the longest (we were roommates during visiting weekend) and is one of the most generous and adventurous people I know. He spent countless hours hanging out with me in the shop after hours so I could work on my steam engine projects. He cooked me delicious fajitas. He edited this very dissertation. We studied and did homework together. He officiated my wedding. We did political organizing together. He always pushed me to leave my comfort zone and open my mind, and I can't imagine what grad school would've been like without him.

I owe so much to my Mom and Dad, who pushed me to succeed scholastically my whole life, gave me so much support growing up and helped support me through undergrad, nurtured my interests, and made all of this possible. I'm humbled by the lives they have lived, by their wisdom and experience, and am eternally grateful that they both worked so hard to give me the best possible life. And finally, I want to thank Ian. As of writing this, we have spent almost every day of the last eight years together, and it has been the highlight of my life. You have done more than anyone to support me and keep me sane through the rollercoaster of grad school, and I am so proud to now call you my husband.

Dedication

Dedicated to Rich, Sharlene, Dave, and Steve,

the teachers who put me down this path.

This page left intentionally blank.

1 - Introduction to 2D materials

1.1 Physics in two dimensions

Most physicists grapple with the concept of physics in lower dimensions in their very first physics class. This is usually in the context of a discussion about Coulomb's law, which describes the electrostatic potential of an electric charge at a distance *r* away from the charge, and follows 1/*r* dependence in 3-dimensions (3D) or log(*r*) dependence in 2-dimensions (2D). A young physicist might be inclined to think, "We live in 3D, so what's the point of studying this potential in 2D?" Then perhaps the following year, in their statistical mechanics class, they learn that the heat capacity of a gas (whether classical or quantum) takes a different form in 3D versus 2D. And again, they might be inclined to think, "What in the real, 3D world, could this possibly apply to?"

Then come the boundary value problems in the advanced E&M course: charges on the surface of a conductor, charges confined to dielectric slabs, and in fact a whole class of problems in which the behavior is much more like the 2D case than the 3D case. What the young physicist failed to consider in their early years is that there are ways of *tricking* nature into behaving like it exists in a different number of spatial dimensions. This is the story of 2D materials. They are crystals which exist in three spatial dimensions, having appreciable extent in along all three. The catch is that, along one spatial direction, the crystal lattice is interrupted after each period of the lattice by a narrow gap, typically of a few Ångstroms[1]. The lattice is stitched together across this gap, not by covalent, ionic, or polar bonds, but by the van der Waals force. This decouples the layers of the material to some degree electronically, mechanically, thermally, and in every other physical sense, confining their excitations to within a layer and endowing them with genuinely 2D properties.

Since the discovery of the quantum Hall effect in graphene[2], for which the 2010 Nobel Prize in physics was awarded to Andre Geim and Konstantin Novoselov, the study of 2D materials has blossomed into a subfield of solid state physics in its own right. But like most endeavors in modern physics, this decade-and-a-half old pursuit is firmly rooted in history. In 1924, William Bragg and John Bernal performed x-ray crystallography measurements of graphite and confirmed the long-standing assumption that the bulk material was in some way comprised of a layered

structure[1], which made it flexible and allowed it to be easily cleaved and peeled apart along a specific plane. But what they discovered was that this was the *ultimate* layered structure, a stack of atomically thin sheets composed of carbon atoms arranged on a 2D honeycomb lattice. The force which holds the layers together was not well understood for another three decades, when in 1955 Evgeny Lifshitz performed the first detailed calculations and accurately described the van der Waals force[3]. It is for this reason that 2D materials are often referred to by the moniker "van der Waals materials".

Further motivation to study 2D materials comes from a somewhat more recent subfield of solid state physics, the study of thin films and quantum wells (QWs). These material systems are thin, usually epitaxially grown layered structures of conventional 3D materials. The motivation for studying such systems are twofold: first, to lower the density of bulk states relative to the surface states, thus allowing surface physics to dominate the material's behavior; second, to confine the bulk excitations of a material to a great degree along the out-of-plane direction as a means of quantum engineering. The quantum mechanical description of a particle existing and moving freely through 3D space is more or less the same as that of a classical particle (notably, the dispersion of the particle will generally differ if the particle is moving through any sort of potential structure, whether periodic or disordered). But by confining the particle along one or more dimensions on a length scale approaching its de Broglie wavelength, its quantum nature is revealed immediately and will manifest, for example, a discretized energy spectrum. This is one of the first quantum mechanics problems a young physicist will encounter, the canonical "particle in a box". The quantum confinement can reshape the particle's wavefunction, and in doing so break or reduce symmetries. For example, a particle in 3D free space in its center-of-mass frame of reference will have a continuously rotationally symmetric wavefunction about all axes. Confinement of the particle along one dimension, i.e. within a sheet, will destroy the rotational symmetry about two of the axes, replacing it with π rotational symmetry instead. Confinement along *two* directions (i.e. within a wire) will restore the rotational symmetry about the axis lacking confinement.

It's also worth noting that a large number of 2D materials, including many of the most ubiquitous members of that family, have been studied in their bulk forms for many decades. For

example, the study of graphite dates back about a century[1]. The wide-gap semiconductor (or insulator) hexagonal boron nitride (hBN) was characterized by x-ray crystallography in 1950[4]. The band structures of the semiconducting transition metal dichalcogenides (TMDCs) were calculated in the 1960s and 70s[5,6]. The layered ferromagnetic insulator CrI_3 was discovered and characterized in the 1960s[7]. In fact, with the exception of CrI_3, these material all have industrial uses dating back at least a century. Graphite is used as a refractory material, and TMDCs (as well as graphite) excel as industrial lubricants due to their layered structure which allow their layers to slide past each other. But it wasn't until 2004 that the mechanical exfoliation technique used to produce mono- and few-layer samples of 2D materials was discovered[8]. And since then, the family of 2D materials has grown substantially to include almost every class of material, from mundane materials like semi-metals[9], true metals[10], semiconductors[11], insulators[12], and magnets[13], to more exotic materials like superconductors[14], topological insulators[15], and even quantum anomalous Hall materials[16] and candidates for hosting elusive quantum spin liquid physics[17]. These emergent quantum behaviors in most cases are contingent on the 2D nature of the materials, and the manifestation of new physics and phases in low-D materials is reason enough to study them.

1.2 van der Waals heterostructures

A limitation of quasi-2D materials systems such as III-V group semiconductor QWs is the need for lattice matching between the layered structure and the substrate it lies on, as well as any other adjacent crystalline materials which are grown epitaxially as part of the assembled structure[18]. Because layers of such structures are stitched together by chemical bonds rather than by the vdW force, they must be similar enough with one another to bond seamlessly and periodically. The imposition of this condition severely restricts the number of materials which are intercompatible, largely to analogue compounds involving elements of the same (or nearby) group from higher or lower periods (e.g. aluminum and gallium in GaAs/AlAs structures), or alloys.

This limitation is firmly avoided by vdW materials which, due to the lack of interlayer chemical bonding, can be freely combined with each other (as well as with 3D materials, which

are often used as substrates or electrical contacts) to form heterostructures with diverse properties. Stacked layers of disparate materials can interact weakly or strongly, depending on their respective electronic or crystal structures, or other types of ordering.

An example of a weakly interacting heterostructure is graphene on hBN. Since graphene is a gapless semimetal and hBN is an insulator, and the graphene Fermi level is well inside the hBN electronic band gap, charge transfer and the formation of interlayer electronic excitations are forbidden. That is not to say that they don't interact; they do interact physically by means of their crystal lattices, in fact to spectacular effect. The lattices of hBN and graphene are very similar: they have the same honeycomb shape, and their lattice constants differ only by a fraction of a percent. As a result, when their crystal axes are well aligned and they are placed in contact with each other, a long-range superlattice is formed (this can be thought of as a spatial beat pattern between the sublattices.) The 1st order effect of applying such a superlattice to a crystal is the expansion of the unit cell and reduction of the Brillouin zone, and consequently the folding of its band structure to lie within the reduced Brillouin zone. In many cases, where band folding would cause the intersection of two or more bands, new band gaps are opened[19].

An example of a strongly interacting heterostructure is formed by stacking together two distinct members of the family of semiconducting TMDCs, for example WSe_2 and $MoSe_2$. In this case, the two semiconductors have similar band gaps and slightly different work functions, which create a staggered type-II band alignment. This strongly couples their electronic structure and facilitates charge transfer and the formation of interlayer optical excitations called *interlayer excitons*, bound states comprised of an electron in one layer and a hole in the opposite layer[20]. And because the two TMDCs have similar lattices and similar lattice constants, *they too* form a moiré pattern which has been demonstrated to create a periodic potential landscape which can confine these interlayer excitons[21,22].

1.3 Overview of dissertation

Most of physics happens at boundaries, or at least, due to boundaries. Classical and quantum fields without boundaries produce simple and unexciting results most of the time. Boundaries break symmetries and confine fields, paving the way for new types of excitations and

altering the energy structure of a system. It is not surprising, then, that interfacial engineering is ubiquitous in condensed matter physics, and many of the greatest technological accomplishments of the field lie with the engineering of the boundary between dislike semiconducting materials. The understanding of electronic and magnetic excitations at boundaries, the ways in which they can be controlled by interfaces, and the ways in which materials can be combined to produce new structure materials with engineered behaviors are of vital interest to the solid state community. And of course, 2D materials present a plethora of new opportunities to discover and design new phenomena thanks to their van der Waals nature.

In this dissertation, we won't explore a specific material system. We won't focus on any particular type of experiment, or the design, revision, and perfection of a specific type of solid state device. Instead, the intent of this dissertation is to explore some of the peculiar ways in which physical phenomena—often phenomena which have been observed in one way or another in quasi-2D or 3D systems—manifest in 2D materials thanks to their low dimensionality and unique way of interacting with their environment and with each other. We will discuss new ways to engineer and manipulate materials through van der Waals heterostructures, new techniques to probe the physics they host, and strategies to control and design their interactions with one another.

In the second chapter, we will discuss the state-of-the-art in van der Waals nanofabrication of 2D devices. The techniques developed and described in that chapter have become standard practice in many labs thanks to their reliability and high throughput. This will set the stage for the following chapters, in which the fabrication of high-quality multilayer devices is desirable if not crucial to produce the intended result. In the third chapter, an important family of 2D semiconductors, the semiconducting transition metal dichalcogenides, will be introduced. These were among the first 2D materials to be exfoliated and studied extensively due to interest in their unique spin-valley locking and direct band gap in the technologically useful near infrared. The fourth chapter concerns the unique properties of excitons, excited and electrostatically bound electron-hole pairs, in atomically thin transition metal dichalcogenides, where the dimensionality plays an outsized role in shaping the basic quantum mechanical description of their formation and interaction with their surrounding environment. We probe these 2D excitons

optically, making use of massive magnetic fields to reveal their fundamental properties through their diamagnetic shift. In the fifth chapter, we combine different members of the transition metal dichalcogenides together to create heterobilayers which host interlayer excitons, analogous to the spatially indirect excitons of III-V coupled quantum wells, and discuss a powerful approach to tuning their optical and dynamic properties by van der Waals engineering of the interlayer interaction. The sixth and seventh chapters concern the investigation of two brand new layered 2D magnetic materials. First, in chapter six, a family of solid solutions of CrI_3 and $CrBr_3$, a pair of recently discovered 2D magnets, are explored. By mixing the halide constituents to form solid solutions of the two, we demonstrate the ability to control the basic magnetic properties of these materials, most crucially the interlayer interaction in multilayered samples. Then, in chapter seven, we present our discovery of magnetically coupled photoluminescence in the layered ferromagnetic semiconductor CrSBr. The strongly layer-dependent coupling between the magnetism and the electronic degrees of freedom are unique among not just 2D materials, but demonstrate the ultimate potential for layered interactions to control symmetry and produce new physical effects from interlayer interactions. Superficially, these disparate results from numerous material systems might appear unconnected, but it is clear that 2D device engineering, and specifically engineering of interlayer effects, have produced some of the most stunning scientific breakthroughs in the one-and-a-half decade history of 2D materials. This is the thematic thread woven throughout this dissertation, and the results presented within it hopefully represent a useful foundation for future discoveries.

2 - van der Waals nanofabrication

In this chapter, we will describe the step by step process for fabricating samples and layered structures of 2D materials. Particular attention will be paid to the different techniques that can be used to stack 2D materials together to form heterostructures.

2.1 Preparation of atomically thin 2D samples

The first step in preparing a sample of a 2D material is the growth of a bulk crystal. Crystal growth is a complex topic which is beyond the scope of this dissertation. However, the procurement of high quality (as in chemical purity, mechanical and physical quality, and absence of defects and faults) crystals is crucial at every step of 2D materials research. Much gratitude is owed to the skilled crystal growers of the 2D materials community for the availability of such high quality crystals for the research discussed in this dissertation.

Bulk crystals of 2D materials most often take the shape of thin platelets and are generally monocrystalline (fig. 2.1.1 a). They are typically a few square millimeters in lateral size and tens to hundreds of micrometers thick. The flat faces of the platelets are parallel to the planes of the material's layers and are typically very shiny, indicating high chemical, crystal, and thickness uniformity. Certain materials, such as CrSBr, grow as needle or matchstick-like crystals, several millimeters long, one millimeter wide, and a fraction of a millimeter in thickness (fig. 2.1.1 b). The color and opacity of the crystals reflects the band structure of a given material: graphite bulk crystals, as a semimetal, are opaque and highly reflective (fig. 2.1.1 a); the semiconducting TMDCs, with their red/NIR bandgap, are also opaque to visible light but transparent to infrared light; and hBN, with its 6 eV bandgap (fig. 2.1.1 c)[12], or Chromium Chloride with its 3 eV bandgap and mid-gap crystal field states[23,24], are transparent to visible light with some coloration (fig. 2.1.1 d).

The most common approach to produce atomically thin layers of 2D materials in a research setting is by means of mechanical exfoliation. In this technique, pioneered by Andre Geim in the early 2000s[8], bulk flakes of 2D materials are pressed against a few cm long piece of adhesive tape (typically Scotch® tape or similar), and the tape is folded in on itself and peeled apart repeatedly. Each time the tape is folded and peeled apart, the bulk crystal is cleaved in half

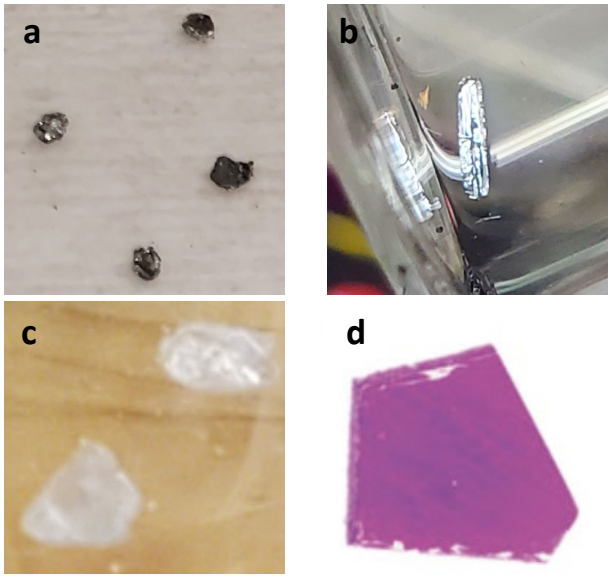

Figure 2.1.1 Bulk crystals of 2D materials. **a** Graphite, **b** CrSBr, **c** hBN, and **d** $CrCl_3$.

and duplicated on the tape (fig. 2.1.2 a). The crystal is typically cleaved in this way between 5 and 10 times, resulting in 2^5 to 2^{10} duplications of the original crystal. The result is a piece of tape which is largely covered with a thin film of cleaved bulk crystal, with typical thickness on the order of 10s of nanometers to a micrometer.

The crystal film covered side of the prepared tape is then carefully placed against a substrate, so as to avoid trapping bubbles between the substrate and the film of cleaved 2D material. The two are then rubbed together a soft, pointed implement (fig. 2.1.2 b). The implement is rastered across the entire tape/substrate with gentle force in order to bring the 2D material into intimate contact with the substrate across the entire interface. The most commonly used implements are round-nosed plastic tweezers, pencil erasers, or the rear of a permanent marker. The relatively large radius of curvature (a few millimeters) and relatively soft materials they are made from ensure that the pressure applied by these implements, and the local strain gradients that would produce within the 2D material and substrate, are small enough to not fracture it. Different implements may also be used for different materials. Durable, pliable materials such as graphene can tolerate much more aggressive agitation such as with a rounded plastic tweezer, while soft and brittle crystals like hBN require a gentler touch, made easier by the use of a more gently curved and softer tool, such as a pencil eraser.

Following this step, the tape is carefully peeled away from the substrate from one end at a rate of 0.1 to 1 mm/s, and the bend angle held between the released tape and the substrate is typically around 45-90° (fig. 2.1.2 c). As the tape is peeled away, a fraction of the 2D material film on the tape that was in contact with the substrate will remain adhered to the substrate and separate from the tape (fig. 2.1.2 d) This is only possible if the van der Waals interaction between

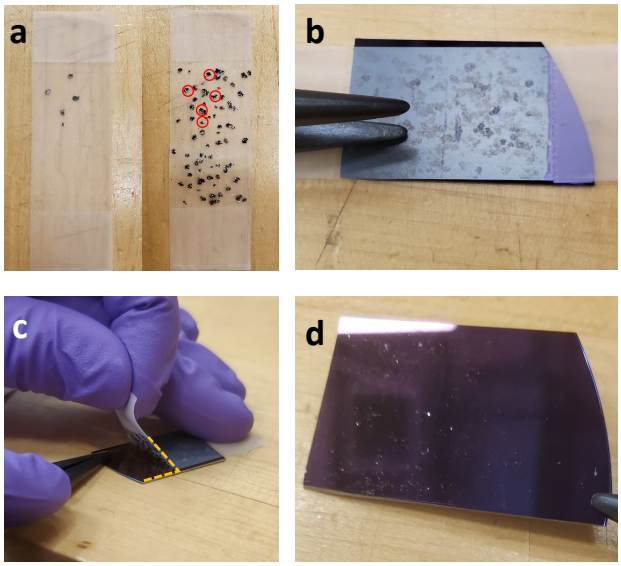

Figure 2.1.2 Mechanical exfoliation process. **a** (left) Five bulk flakes of graphene on a piece of Scotch tape are peeled apart by folding the tape in on itself several times (right). The locations of the original bulk flakes are circled in red. **b** The tape is placed against a piece of Si/SiO_2 wafer and they are rubbed together with rounded tweezers. **c** The tape is peeled away from the substrate at a low angle (marked yellow). **d** A scattering of exfoliated flakes are left behind, giving the substrate a speckled appearance.

the 2D material and the substrate is stronger than the interlayer cleavage energy. There is also a dynamic aspect to this process; if the tape is removed from the substrate too quickly, the density of deposited flakes will generally be lower than if it were removed slowly. And if the tape is peeled away with an extreme bend angle (close to 180°), a large differential strain will be applied to the 2D material film, resulting in the crystals being fractured and damaged.

The substrates used for exfoliation can vary considerably depending on experimental needs, but the most common substrate by far is a chemically doped conductive [0 0 1] silicon wafer covered with a thin (90-300 nm thick) coating of thermally grown amorphous SiO_2 (henceforth, this will be referred to as an Si/SiO_2 wafer or simply by the thickness of the SiO_2 coating, i.e. as *90 nm oxide*). Si/SiO_2 wafers are a good general purpose substrate: they are mass produced for the semiconductor industry and are thus relatively cheap and abundant, the polished finish of the oxide coating is fairly smooth (roughness typically on the order of 5 Å), the vdW attraction of most materials to this substrate is strong enough for a decent yield with exfoliation, and the doped silicon itself is conductive enough to use it as a global electrostatic gate. The choice to use other substrates is dependent on the vdW material being exfoliated or specific experimental needs. For example, if one needs a transparent substrate in order to perform an optical transmission experiment, sapphire, quartz, or polished fused silica wafers are a good alternative. On the other hand, some materials have difficulty adhering to dielectric substrates, in which case the use of a metal coated Si/SiO_2 wafer can improve exfoliation[25]. Examples of materials which exfoliate poorly on Si/SiO_2 but exfoliate well on films of gold or other

noble metals include TMDCs and $MnBi_2Te_4$. Exfoliation onto a soft, transparent polymer called polydimethylsiloxane (PDMS)[26] is sometimes used in preparation for creating layered- or heterostructures of materials which have temperature sensitivity (this will be discussed in detail in section 2.3), or in special applications which require the use of a flexible substrate[27,28], i.e. for the application of strain to the 2D sample.

The adhesion between 2D materials and Si/SiO_2 wafers can be improved in a number of ways. The simplest is by heating the substrate while the exfoliation tape is attached to it, usually to between 100-120°C for 1-3 minutes[29]. This results in more adhesive residue contaminating the substrate, but also improves exfoliation yield for graphene, transition metal dichalcogenides, and many other materials. It notably does not improve the adhesion of hexagonal Boron nitride. The mechanism for this effect is unknown. Another approach to enhancing adhesion between vdW materials and SiO_2 is oxygen plasma treatment of the substrate[29], which removes hydrocarbon contaminants and makes it strongly hydrophilic, resulting in accumulation of charged OH^+ groups on the substrate which attract van der Waals materials electrostatically. This method is known to degrade some materials, including graphene, following exfoliation onto the treated substrate[30].

2.2 Identification and classification of thin 2D samples

The next step in the production of 2D samples is identification of thickness and classification of the thin flakes of material deposited on the substrate during exfoliation. There are many ways to determine the thickness of flakes which vary in accuracy and difficult. The most commonly used technique is simple brightfield microscopy, in which case the thickness of a flake is determined by comparing its color and optical contrast to those of a flake whose thickness has been determined quantitatively (fig. 2.2.1 a). The optical characteristics of a flake under broadband brightfield illumination derive from a combination of the wavelength-dependent reflection and absorption coefficients and thin-film interference. This latter is especially relevant when Si/SiO_2 wafers which have oxide thickness on the order of hundreds of nm are used as a substrate. The optical contrast of a 2D material flake of a given thickness therefore depends on the substrate used (fig. 2.2.1 b-d). In this case, the fully wavelength dependent complex index of refraction must be taken into account, and the optical contrast can be modeled using the Fresnel

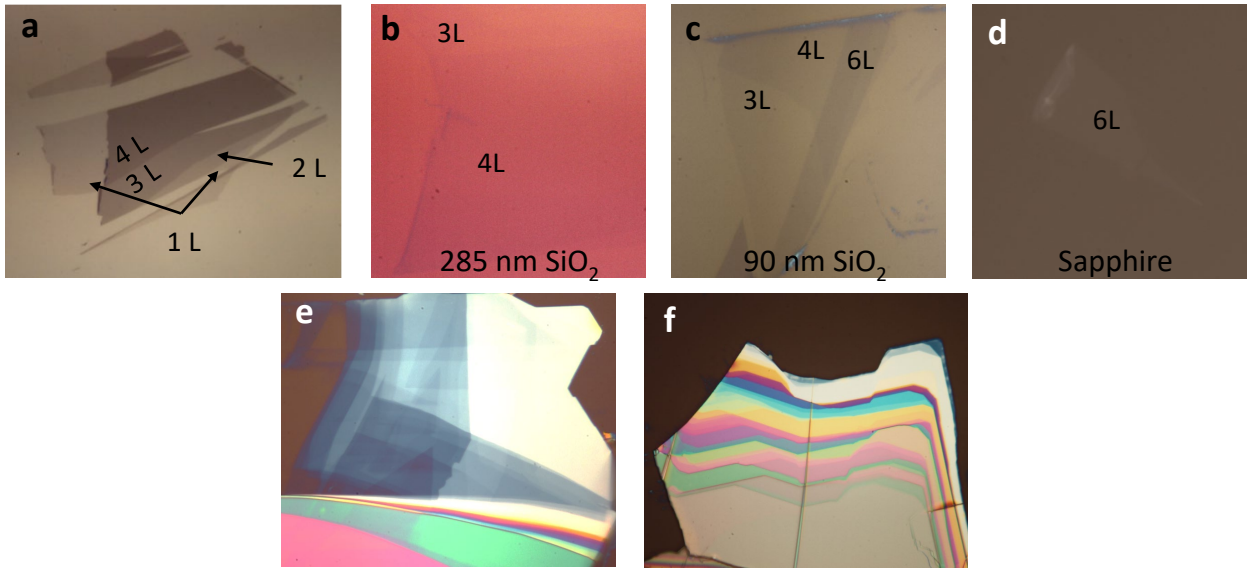

Figure 2.2.1 Brightfield identification of 2D layers. **a** Graphite exfoliated on 90nm SiO_2 on Si. Layer thicknesses are marked. **b** hBN exfoliated on 285 nm SiO_2. Three and four layer thicknesses are barely visible on this substrate. **c** 3-6 layer thick hBN on 90 nm SiO_2. The 3 layer sample is more clearly visible on this substrate. **d** 6 layer thick hBN exfoliated on a sapphire wafer has poor optical contrast due to a lack of thin-film interference effects. **e** A highly graduated flake of hBN, which varies in thickness from a couple nm (faint blue) to white (about 60 nm). Green and pink areas are hundreds of nm thick. **f** Periodicity of colored interference in extremely thick hBN, which ranges from about 60 nm up to several micrometers thick.

equations[13]. Not only will the apparent brightness or darkness of the flake change with thickness, so too will the apparent hue of the sample which is often derived in part from thin film interference from the substrate. The flake of 2D material alters the boundary conditions, adds an additional interface, and changes the effective thickness of the interfering film. This effect is especially pronounced with hBN[31] which is purely refractive at visible wavelengths and is often needed in relatively thick (20-100 nm) flakes which can substantially change the effective thickness of interfering film (fig. 2.2.1 e-f). On highly reflective or highly transparent substrates (i.e. gold films or sapphire, respectively), the optical contrast is generally more straightforward and depends almost exclusively on the reflection or absorption spectrum of the material, respectively. Comparison of optical contrast by a trained eye is possible and usually reliable, especially for relatively thin samples which absorb light strongly, such as graphene or TMDCs. However, this still relies on the brightfield microscope having a light source with a consistent emission spectrum, and if the micrograph is being monitored by a camera, on having a consistent white balance and exposure.

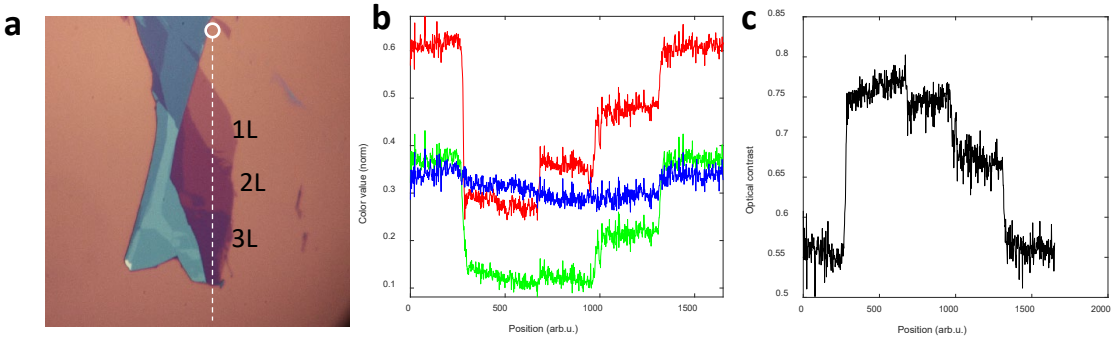

Figure 2.2.2 Quantitative measurement of optical contrast. **a** Image of a multi-thickness exfoliated WSe_2 flake. Layer thicknesses are labeled. **b** Image brightness resolved into the three primary color channels (red, green, blue) along the white dashed line in panel a, starting at the white circle (position 0). **c** Optical contrast calculated as the average *darkness* of the color channels. Note the uneven step height. By comparison, the step height of the red channel in panel b is consistent from layer to layer, because WSe_2 absorbs red light while blue/green are refracted/reflected to a larger degree. Contributions to the color in the blue/green parts of the spectrum are largely from thin film interference effects, giving rise to the contrast nonlinearity in those color channels.

In cases where it is difficult to identify a sample by eye, a quantitative measurement of optical contrast can be performed by taking an image of the micrograph (done with a digital camera attached to the microscope) (fig. 2.2.2 a) and using image analysis software to analyze the pixel data of the image (fig. 2.2.2 b). This data can be normalized and corrected for differences in illumination or white balance based on the color of the substrate (fig. 2.2.2 c). If the dielectric function of a given material is known across visible frequencies, the layer dependent optical contrast can be calculated with the Fresnel equations and projected onto the color space of the camera. Thus it is possible to classify the thickness of a given flake entirely from brightfield microscopy, without needing to compare it to a reference flake of known thickness. This is not generally done, though, since measuring the full complex dielectric function is a considerable experimental effort and in many cases the dielectric function depends again on the thickness of the sample, thus reintroducing the need to determine the thickness of the sample by some other quantitative means.

A straightforward approach to determining the thickness of a sample is to use atomic force microscopy (AFM) to measure the sample topography. If one knows the interlayer spacing of the material and the size of the vdW gap between the material and the substrate, the

measured AFM height can be used to calculate the number of layers constituting the sample. The interlayer spacing (or period) of a given material and its substrate-sample spacing can be determined by numerical simulations, or they can be determined empirically using the following method.

First, a number N of exfoliated flakes of varying thickness must have their thickness measured by AFM. The measured thicknesses will have the form $T_{meas} = LT + \tau + E_{AFM}$, where L is the number of layers in a given flake, T_{layer} is the interlayer spacing, τ is the van der Waals gap between the sample and the substrate, and E_{AFM} is the random error of the AFM reading. T is typically 0.3-1.5 nm, τ is typically 0.2-0.5 nm, and E_{AFM} can be as low as 0.1 nm for a careful, high-resolution scan. We define the function $A(T', \tau', T_{meas}) = \mathrm{mod}_{T'}(T_{meas} - \tau')/T'$ and $\bar{A}$ as the average of *A* over all values of T_{meas}. Clearly A should be extremized in the vicinity of T'=T and τ'=τ. This analysis makes it fairly simple to accurately estimate both T and τ.

Measurement of a sample's AFM topography has the added benefit of also determining if there are any superficial contaminants on the exfoliated flake, such as polymer residue left from the exfoliation tape or nanoscopic fragments of the 2D material itself. The AFM tapping phase, which, in a sense, measures deviations in the anharmonicity of the interaction potential between the tip and the sample, is even sensitive to molecular adsorbates like water[32]. Superficial contamination can alter optical and electronic properties of a sample and are especially problematic when stacking contaminated layers together to form heterostructures, which will be explored more thoroughly in section 2.3 of this dissertation.

Intrinsic layer-dependent properties of some 2D materials can be used to determine their thickness. A common technique for specifically identifying monolayers of materials which have Raman-active interlayer phonon modes is to perform Raman spectroscopy, in which case the absence of the interlayer mode in the Raman spectrum indicates that the sample is a monolayer[33,34]. Other, less general examples include the use of photoluminescence (PL) spectroscopy to identify TMDC monolayers[11], which have a direct band gap (and thus emit PL) only in the monolayer thickness, or the use of the magneto-optical Kerr effect (MOKE) or magnetoresistive effects to measure the magnetization of of CrI_3, whose monolayer has a simple

hysteresis loop ferromagnetic response to an applied perpendicular magnetic field which evolves into staircase magnetization in thicker samples[13,35].

2.3 van der Waals transfers

Among the most useful and novel properties of exfoliated 2D materials is the ability to stack them and combine them with each other without restriction to form functional heterojunctions. A simple example of this is a hexagon boron nitride (hBN) encapsulated graphene field effect device, shown schematically in figure 2.3.1 a. This device is made from four separate exfoliated flakes of 2D materials, including a monolayer flake of graphene at the center of the device which is the current channel, two thick (few to 10s of nm) flakes of hBN which serve as atomically flat substrates for the graphene as well as dielectric barriers, and a few-layer graphene flake to serve as conductive gate on top of the device, to which a voltage may be applied in order to capacitively charge the graphene layer. The use of hBN as a substrate is very common in multilayer samples for a number of reasons. Because they are atomically flat monocrystals cleaved along crystal planes, they are an exceptionally smooth substrate, providing an environment for samples placed on top which has minimal disorder. Boron nitride has a relatively high breakdown voltage along the c-axis due to its wide band gap[36,37], high crystalline quality, and most importantly the presence of van der Waals gaps between layers which act as vacuum tunneling barriers. This makes it an excellent choice to use as a dielectric barrier in capacitive structures. Lastly, it is transparent at optical frequencies[12,31,38], which allows it to be used to encapsulate air-sensitive samples to act as a protective barrier while allowing optical probes and signals to penetrate to the sample and be collected open reflection, transmission, or emission from the sample. Graphite is commonly used as gate electrodes in capacitive structures because it retains good conductivity down to a thickness of about 3 layers (approximately 1 nm)[8,39–42], at which point it transmits around 90% of incident visible and near-infrared light[43,44]. A comparably conductive layer of gold would be around 10nm thick and only transmit about 30% of incident visible light[45,46].

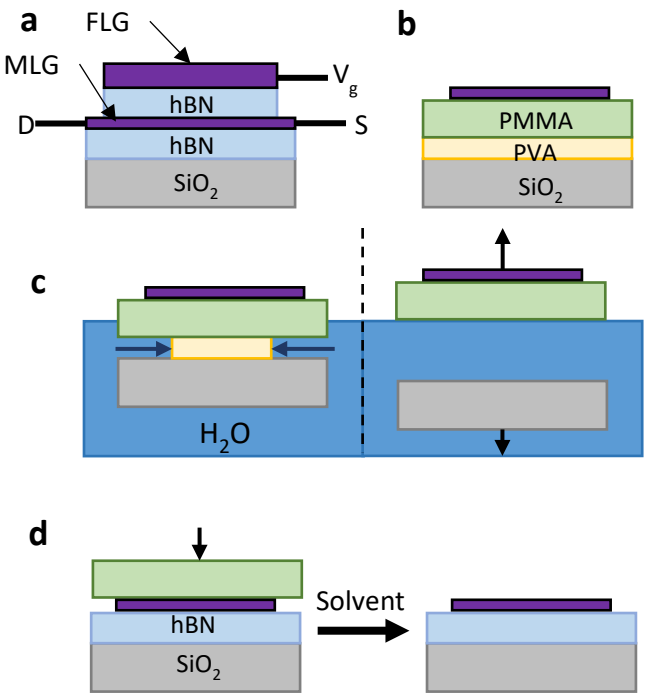

Figure 2.3.1 Wet transfer technique. **a** Schematic of a multilayered vdW field effect device, in which the channel is monolayer graphene (MLG), the dielectric barrier is hBN, and the gate is few-layer graphene (FLG). The source (S) and drain (D) are biased to produce a current while a voltage V_g on the gate tunes the Fermi level. **b** Cross section of a sample exfoliated onto a substrate for wet transfer assembly. **c** The substrate is placed into water, which dissolves the PVA layer, after which the sample floats on the water meniscus by surface tension. **d** After being picked up by a wire loop, the PMMA layer with attached 2D material are placed onto a target vdW layer for stacking. The PMMA is then removed by solvent.

The assembly of multilayered vdW structures is accomplished by means of a van der Waals transfer. There are several different types of transfers used which will be described below, but all rely on the same basic principle of temporarily attaching an exfoliated 2D material to a polymer substrate, placing this in contact with a second layer, and then removing the polymer by some means. For modern transfer techniques, the pick-up/set-down process can be repeated many times to build many-layered structures.

The first transfer technique developed is the so-called wet transfer process[47]. In this early technique, the substrate *is* the adhesive polymer layer, and consists of an Si/SiO_2 wafer with a spin-coated layered structure of poly-vinyl alcohol (PVA), a water soluble polymer, then a layer of poly-methyl methacrylate (PMMA), which is not water soluble. The 2D materials are directly exfoliated onto the PMMA layer and suitable exfoliated flakes are identified (fig. 2.3.1 b). The wafer is then cleaved to a smaller size (approximately 5 x 5 mm) with the 2D flake centered. The wafer is then gently lowered into a beaker of water which gradually dissolved the PVA, leaving behind just the PMMA membrane with the 2D material attached (fig. 2.3.1 c). Finally, the floating membrane is picked up with a wire ring, inverted, and placed on top of a second 2D material flake under a microscope before dissolving the PMMA away with acetone or dichloromethane

(DCM) to leave a bare stacked 2-layer structure (fig. 2.3.1 d-e). This technique has several serious drawbacks. First, it is incompatible with materials that are sensitive to water or solvent. Second, it exposes both surfaces of the transferred flake to either water or polymer, potentially contaminating it. Finally, it can only be used to stack one layer at a time, requiring time-consuming and risky repeated transfers to assemble multilayered structures. Despite these shortcomings, this technique was used to produce several important breakthroughs in the early days of research into van der Waals heterostructures.

The next transfer process that was widely adopted by the 2D materials community was the polycarbonate (PC) dry transfer[47,48], which sought to resolve many of the problems with the wet transfer process. The PC dry transfer begins with samples exfoliated directly onto an inorganic substrate like Si/SiO_2 wafers, fused silica, quartz, sapphire, or any other smooth, chemically inert substrate. This flexibility is one of the key advances with the PC dry transfer process. The transfer is carried out using a sacrificial polymer substrate called a *stamp* (fig. 2.3.2 a), which consists of a small (3 x 3 x 1 mm) block of poly-dimethyl siloxane (PDMS) adhered to a glass microscope slide. A piece of polyimide double-sided tape with a hole punched in the middle is placed around the PDMS block and adhered to the slide. A piece of Scotch tape with a hole punched in the middle is used to pick up a thin film of PC, which is then stretched over the PDMS block and adhered to the double-sided tape, with the PDMS block centered on the window in the Scotch tape.

The preparation of the PDMS is carried out in advance and is made from a liquid 2-component kit, mixed together thoroughly in a ratio of 10 parts base to 1 part hardener. It is then cast in a flat-bottomed petri dish and placed in a vacuum chamber to remove trapped air bubbles. Finally, it is cured in an oven at 40° C for 24 hours before being cut into small blocks. The PC film is typically prepared fresh from a premade solution of 6-12% (weight) Poly-bisphenol-A carbonate dissolved in chloroform. The solution is removed from its sealed bottle by a disposable pipette and carefully squeezed onto a glass microscope slide in a long line stretching across the entire slide. A second slide is then lowered onto the first slide, causing the PC solution to spread across the entire interface by capillary action. This step must be done promptly as the chloroform evaporates quickly. The viscosity of the PC solution is controlled by its concentration; if it is too

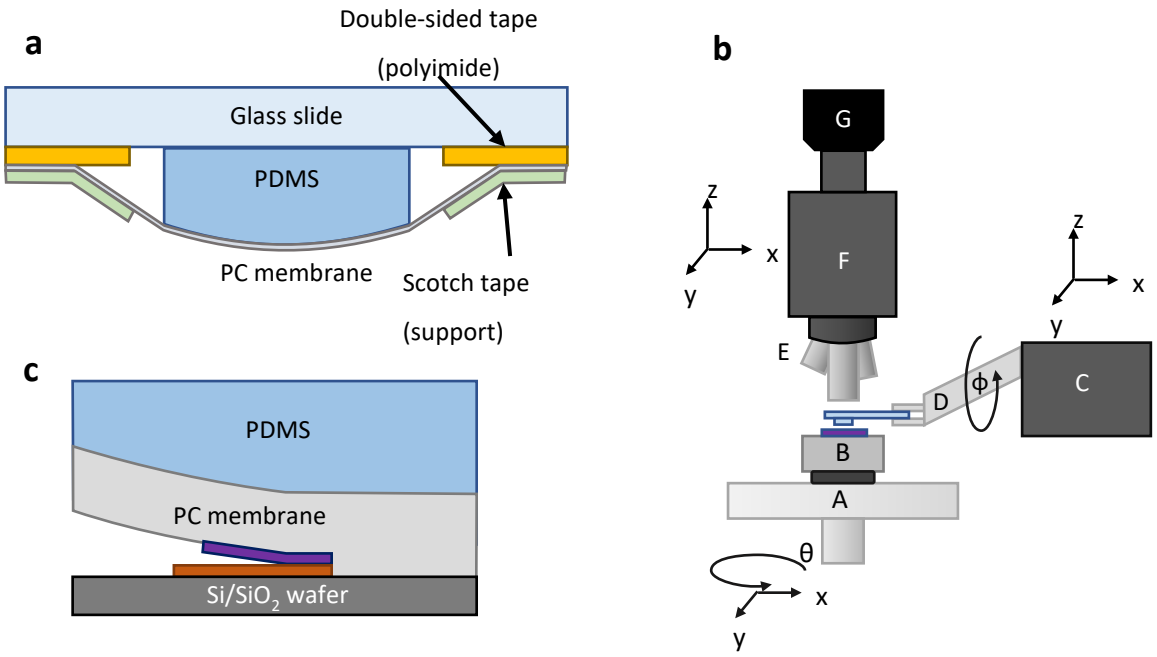

Figure 2.3.2 PC dry transfer process**. a** Cross section view of a dome-shaped PC/PDMS stamp. **b** Schematic of a transfer stage for manipulating and assembling multi-layered stacks. Components are as follows. A: rotating sample translation stage. B: Heated vacuum chuck for securing sample, on a black viton gasket. C: 3-axis micromanipulator for positioning stamp. D: Pivoting stamp holder graps an assembled PC/PDMS stamp on a glass slide (blue). E: Microscope objective turret with long working distance objectives. F: Microscope column with 3-axis positioning. G: imaging camera. Degrees of freedom for each moving part are labeled. **c** The micromanipulator pushes the stamp down against a substrate mounted on the vacuum chuck, pushing into contact a 2D material already attached to the stamp (purple) and a 2D material on the substrate (orange).

viscous, it won't spread fully across the interface, and if it isn't viscous enough, capillary action will squeeze most of it out from between the microscope slides. The slides are then slid apart horizontally (rather than pulling them apart). This must be done quickly and carefully, as the film will dry almost instantly once exposed. The viscosity and quantity of PC squeezed onto the slide initially determines the final thickness of the PC film, and the viscosity and manner in which the slides are slid apart determine the surface quality of the surface exposed to air. On the other hand, the side of the PC film attached to the glass will be as smooth as the glass itself. The PC film is picked up from the glass slide by attaching the aforementioned Scotch tape with a punched hole to the film. They are rubbed together with a smooth implement, much like in 2D material exfoliation, to improve adhesion between them and loosen the PC from the glass. The section of

PC film attached to the tape is then cut free from the film at the edges of the tape using a sharp blade, and the tape and PC are peeled away.

The assembled stamp is then held by a micromanipulator attached to a microscopy probe station which allows for independent x-y-z position control of the stamp, microscopy head, and sample (fig. 2.3.2 b). The probe station is equipped with a heated vacuum chuck, consisting of an aluminum block with a vacuum through port to secure the sample, with an embedded resistive heater and temperature sensor. The transfer is carried out by attaching the 2D sample substrate to the vacuum chuck and heating it to between 60 and 120° C as a means of increasing the adhesion between the PC film and the 2D material. The stamp is then gently placed in contact with the sample. This is either accomplished by using a stepper motor to lower the stamp, or by raising the sample towards the stamp by increasing the temperature of the aluminum vacuum chuck, resulting in thermal expansion. Contact must be made gradually to avoid sample damage and trapping air at the interface. This is done by slightly angling the stamp so that the interface is wedged, or by using a stamp made from a curved PDMS block (see appendix A) (fig. 2.3.2 c). Once contact between the stamp and 2D material is made, a resting period of a few minutes is used to ensure good adhesion between them. The stamp is then slowly lifted away from the substrate (or the aluminum block is cooled, causing it to shrink away from the stamp), taking the 2D material with it. This process can then be repeated any number of times to produce many-layered samples. A depiction of a successful pick-up of a 2D material layer by a domed stamp is shown in figures 2.3.3 a-c.

Once the assembly is complete, the sample must be removed from the stamp. This is accomplished by placing the stamp in contact with a clean substrate (or alternatively, the last layer in the stack), pushing them together so as to contact a large area of the stamp with the substrate, increasing the temperature of the substrate above the plastic point of PC (165° C), and pulling the stamp away. The area of PC in contact with the stamp, in its molten state, tends to stick to the substrate and not to the PDMS, and so it, along with the stacked 2D sample, will be left behind on the substrate (fig. 2.3.2 d). The sample and substrate are then allowed to cool and rest overnight to improve adhesion between the two, before being rinsed in a series of chemical baths to remove the PC membrane on top of the stack. The procedure for chemical processing is

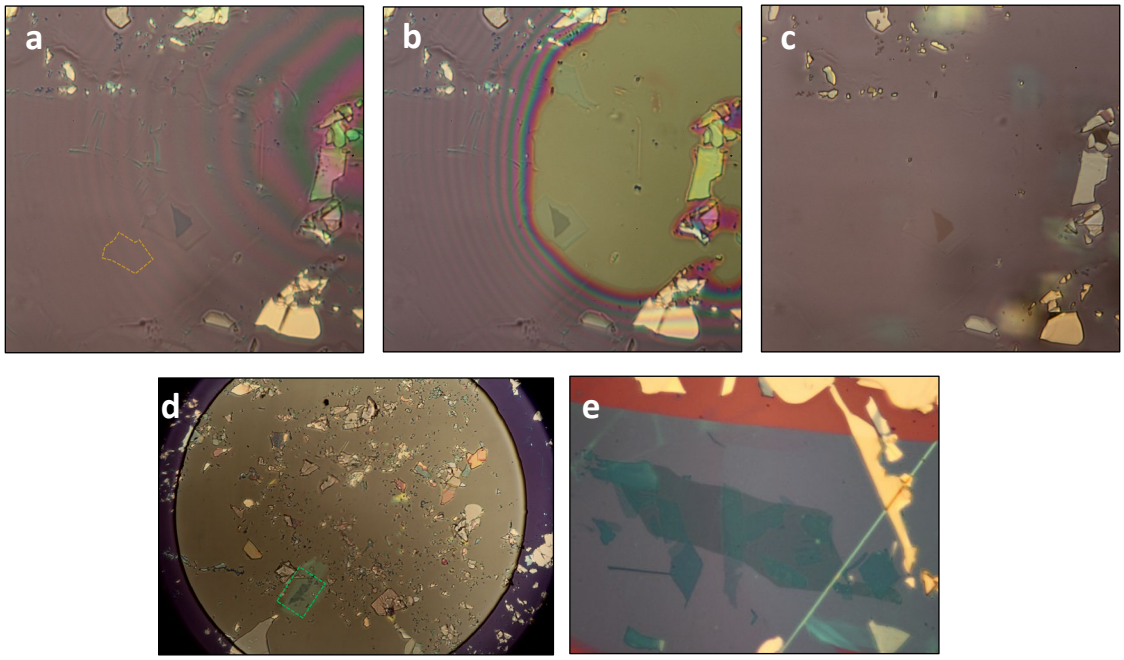

Figure 2.3.3 Fabrication of a multilayer sample by dry transfer **a** A dome-shaped stamp in close proximity to a substrate produces a ring pattern of interference fringes. Note that the spacing decreases away from the center of the dome (right edge) as a result of the angle between the stamp and the substrate increasing radially. The stamp has already been used to pick up a thin layer of hBN (yellow outline), which is nearly invisible on the stamp. A thin flake of graphite to be picked up from the substrate is positioned under it. **b** The stamp is brought into contact with the substrate. The yellow colored area is the region in which the stamp has made contact with the substrate. The hBN flake is now more clearly visible, and the color of the graphite flake has changed slightly as well. **c** The stamp is pulled away from the substrate, lifting the graphite flake with it. Note that the color of the graphite flake has changed once again. The blurred spots are flakes which remained on the substrate plane and are out of the focal plane, located at the raised stamp. **d** The completed sample and PC film (yellow disc) are melted down against a substrate. **e** After a series of solvent baths, the clean assembled multilayer structure is revealed. The area in this picture is represented by the green box in panel d.

as follows: 1 hour in 100 mL chloroform, 4 hours in a second 100 mL bath of chloroform, followed by a final 12 hour bath in isopropanol. The first bath removes the majority of the PC, while the second bath dilutes any PC left on the surface of the substrate in equilibrium with the solution produced in the first bath. The isopropanol bath removes many common contaminants found in standard high purity chloroform. The transfer of the sample into and out of baths must be done carefully and quickly. Fluid force at the meniscus can fold, tear, or remove van der Waals samples from substrates. To minimize the chance of this happening, when transferring the sample

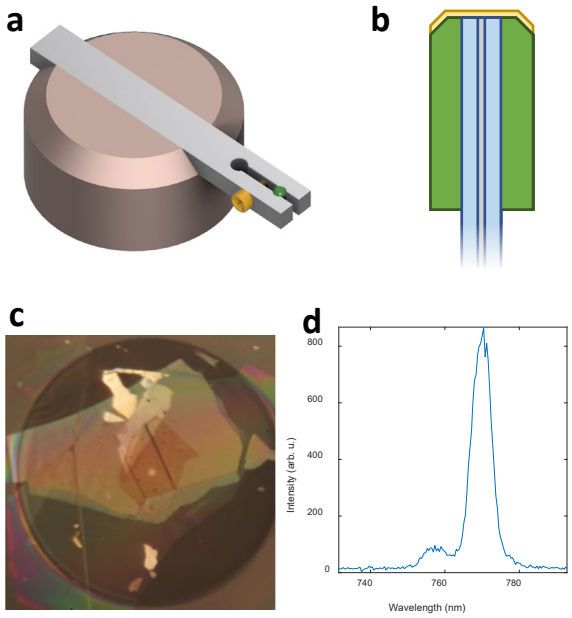

Figure 2.3.4 Transfers onto optical fibers. **a** Fiber chuck assembly for holding an optical fiber for dry transfer. The copper base conducts heat from the heated vacuum chuck of the transfer stage. An aluminum clamping fork is mechanically pressed into a slot in the copper base and tightened against the fiber ferrule (green) using an adjustment screw (yellow). **b** Cross section of a fiber prepared for transfer. Green: ferrule; blue: cladding; white: core; yellow: drop cast PC film. **c** multilayer sample transferred onto a fiber. White light coupled through the other end of the fiber is emitted from the fiber core near the center. The dark circle is the cladding. The rainbow-colored sheen across the sample is the result of the thin, smooth PC film underneath the sample. The slow variation of the rainbow interference pattern indicates the PC film is highly uniform. **d** Sharp PL emission lines from $MoSe_2$ on an optical fiber suggests high sample quality and low disorder.

between baths, the solvent must not be allowed to try on the wafer. A dropper is used to continuously wet the sample between baths using clean solvent from the next bath.

This technique has a number of clear advantages compared to the wet transfer process. Perhaps most important is the ability to form clean interfaces between layers by only one surface of the topmost layer coming into contact with polymer, and the other surfaces never coming into contact with any substance other than atmospheric gas. Dry transfers offer great convenience as well, being able to stack, in principle, an arbitrarily large number of layers together on a single stamp, thereby reducing processing time, labor, and risk for multilayer samples (fig. 2.3.3 e). The throughput is also increased by its high reliability. Whereas in wet transfers the sample is at a high risk of being damaged when the floating PMMA membrane is removed from the water bath, the stacked sample sits on a mechanically stable substrate (the stamp) throughout a multi-step dry transfer process. Finally, the dry transfer technique allows for arbitrarily complex samples to be deposited on unconventional substrates. One particularly relevant example of this is the deposition of van der Waals heterostructures on the tip of a single mode fiber[49]. This use case presents two challenges to the dry transfer process. The first challenge is the method of holding the fiber while

delivering adequate heating to the tip of the fiber, which can be addressed with a specialized fiber chuck which funnels heat towards the fiber tip (fig. 2.3.4 a). The fiber chuck must be mechanically stable, thermally conductive, and shield the fiber itself from contacting any hot surfaces as its protective polymer coating will be damaged by excessive heat. The second challenge is material adhesion. Optical fibers are polished to an optical quality surface, typically with roughness on the order of $\lambda/10$, where λ is the design wavelength of the fiber. This is substantially rougher than typical semiconductor or crystal substrates, which are polished to a sub-nm finish or cleaved along crystal planes. The relatively rough finish of optical fibers can distort and strain 2D materials attached to them and introduce substantial inhomogeneity and reduce van der Waals adhesion. To mitigate this problem, a thin film of PC can be drop cast on the tip of the fiber by simply wiping the tip with a clean room swab dipped in a 1% solution of PC (fig. 2.3.4 b). The resulting film is on the order of a few μm thick based on the appearance of thin film interference (fig. 2.3.4 c). When the fiber tip is heated and the sample placed against it during the final step of the transfer, the deposited PC film and the PC film of the stamp are both semi-fluid. When they meet and flatten together, the sample is effectively suspended in a viscous fluid environment and doesn't relax against the rough substrate. The benefit of this technique can be seen through the nearly homogeneously broadened absorption resonance of hBN-encapsulated WSe_2 samples prepared in this manner, indicating very low disorder (fig. 2.3.4 d). Fiber substrates can also be equipped with electrostatic gates, a process described in more detail in section 4.6.

As an entirely solvent-free alternative to the PC dry transfer, a film made of poly-propylene carbonate (PPC) can be use rather than PC[50]. The stamp assembly is exactly the same as in the PC dry transfer, except the polymer film is prepared using a solution of 10% PPC dissolved in anisole, which is then dried on a hot plate at 60° C for up to 24 hours. The transfer itself is rather similar as well, but the key difference which allows the transfer to conclude without a solvent bath to remove the sacrificial polymer layer after meltdown is that adhesion between vdW materials and PC is highly sensitive to temperature. In a narrow range of temperatures, roughly from 31° C to 35° C, select vdW materials, including hBN, adhere reliably to PC. However, at higher temperatures, especially around 60° C, the adhesion between hBN and PC becomes weak. This enables the assembly of multi-layered structures as long as each layer is picked up in

the lower temperature window, and finally for the assembled structure to be deposited on a target substrate by placing them in contact with one-another and retracting the stamp at a higher temperature. In doing so, the vdW stack will be left on the substrate as the adhesion between them is higher than the adhesion between the vdW stack and the PPC membrane. The difficult of this technique is that the very first layer of the stack generally must be hBN, and it must be large enough for all subsequent layers to fit under it, as they will not stick on their own to the PPC; in essence, the first hBN layer must be used to pick up all subsequent layers. Finding large, clean hBN can be challenging, and it is not always desirable to have hBN encapsulating the entire vdW structure, e.g. if lithographic contact is to be made with some of the layers post-transfer.

Finally, a crude but effective transfer which can be done without temperature control or solvent is the PDMS dry transfer[26,47]. 2D samples are first exfoliated onto blocks of PDMS, typically a few cm in lateral size and 1-2 mm in thickness. After identifying suitable exfoliated flakes, the PDMS is cut down to a lateral size of a few mm, centered on the identified flake. The PDMS is then attached to a glass slide and stamped against a target substrate (or on top of another flake or stack of 2D materials). The adhesion between vdW materials and PDMS is poor, and so the flakes exfoliated onto the PDMS are attracted to the substrate and remain attached to it when the PDMS is pulled away. This has a couple obvious drawbacks: first, stacks assembled using PDMS must be assembled layer-by-layer; second, interfacial contamination by the PDMS is inevitable; third, because vdW adhesion to PDMS is poor, the exfoliation onto the PDMS has a relatively low yield. Nevertheless, for extremely sensitive materials which degrade with exposure to heat, solvent, or atmospheric gasses, this can be a convenient way to quickly encapsulate a sample without much preparation or risk to sample integrity (aside from contamination by PDMS residue.)

2.4 Angular alignment of layers in a van der Waals stack

When rotational alignment between crystal axes of subsequent layers in a vdW transfer is important, a motorized rotation stage can be used to orient the crystal axes of a sample, which must be determined ahead of time. For non-centrosymmetric crystals (e.g. transition metal dichalcogenides), this may be accomplished using polarization-resolved second harmonic generation (SHG)[51–54]. In this technique, ultrafast (150 fs) optical pulses are focused onto the

sample to achieve enormous instantaneous electric fields (~10 MV/cm) which couples to its non-zero second-order polarizability to produce light at twice the frequency of the incident beam. The dependence of the second-order optical response on the polarization of the incident light necessarily reflects the symmetries of the crystal lattice. This polarization response is analyzed by rotating the polarization of the incident fundamental and measuring the intensity of SHG either co-polarized with the fundamental, thus revealing the orientation of the sample crystal axes. However, as this is an intensity-based measurement, there is a π rotational ambiguity in the generated polarization pattern; hence a crystal with threefold rotational symmetry will produce a sixfold polarization pattern, only allowing for the determination of crystal axes *modulo* π.

To resolve this ambiguity, an interferometric phase-resolved SHG technique[55] is employed, in which a reference nonlinear crystal (crystalline quartz) with a fixed orientation is placed in the excitation path. The sample to be analyzed, having already had its crystal axes determined as described above, is aligned with its crystal axes collinear to the reference crystal. As the fundamental pulse passes through the reference crystal on its way to the sample, a colinear pulse of second harmonic is generated. Due to dispersion in the reference crystal and other optics, a small time delay between the reference SHG pulse and the fundamental pulse is introduced. This delayed reference SHG pulse then interferes with the SHG pulse generated at the sample in the time domain, which can be observed spectroscopically (Fourier transform interferometry) as a series of interference fringes superimposed on the SHG spectrum. The interference pattern generated by two different samples are then compared: if the interference fringes antialign, then the crystal axes of the samples are antialigned, and *vice versa*.

In the case of a twisted homobilayer, an alternative method for achieving precise interlayer twist may be employed which eliminates the need to determine crystal axes. The *tear and stack* method is a recent development[56], in which a single monolayer flake of a material is cut into two pieces either through electrochemical etching using an atomic force microscope tip in contact mode or through laser ablation. The two halves of the flake are then stacked on top of each other with a twist angle introduced by rotating the second half before picking it up onto the stamp with the first half.

3 – Fundamental properties of the semiconducting transition metal dichalcogenides

This chapter concerns a family of 2D semiconductors, a specific subset of transition metal dichalcogenides (TMDCs) with the chemical formula MX_2, where M is molybdenum or tungsten and X is sulfur, or selenium. We will first discuss the scientific history of these unique materials before describing their electronic and optical properties. We will then introduce the unique locked spin-valley physics in these materials, and finally discuss the optical excitations they host.

3.1 The semiconducting transition metal dichalcogenides

Molybdenum disulfide has been known to humans for a very long time, although it was historically referred to simply as *molybdaena* and confused variously for lead, lead sulfide (galena), and graphite, despite these compounds all having rather different physical properties (the word *molybdenum* descends from the ancient Greek word Μόλυβδος, *molybdos*, meaning *lead*). It is the most abundant source of molybdenum on earth, and the only TMDC which occurs naturally in significant quantities. In the 18th century, a series of Swedish chemists and mineralogists (first Bengt Andersson Qvist[57], then Carl Wilhelm Scheele[58], and finally Peter Jacob Hjelm[59]) performed extensive and often dangerous experiments to study *molybdaena* and determined that the mineral in question was a sulfur salt of the metal which would eventually be referred to by modern chemistry as molybdenum. In the 19th century, MoS_2 began to see industrial use, both as a dry lubricant (like graphite, it inherits its lubricative properties from the layered nature of its structure, which permits particles of the material to slide along each other, and for caught particles to simply slide apart)[60], and as a dopant in metallurgy[61].

Modern research of MoS_2 and other semiconducting TMDCs began following the discovery of quantum mechanics and the development of a framework for studying crystalline solids. Alongside MoS_2, the analog compounds involving tungsten and selenium were synthesized and studied. This included numerous modern experiments like electron energy loss spectroscopy, electron spin resonance spectroscopy, photovoltaic measurements, and optical spectroscopy[62–

[64]. This period of focused research on bulk TMDCs lasted throughout the 1960s and early 1970s before interest waned as other materials rose to prominence.

In the 2D era, the study of TMDCs has experience something of a renaissance. Following the isolation of monolayer MoS_2 in 2010 and the discovery of bright photoluminescence in monolayer TMDCs[11], they have become one of the most studied families of 2D materials, lagging only behind graphene and black phosphorus. The reasons for the resurgent interest are numerous. Key properties which have contributed to this interest can be largely distilled into two categories. First, the semiconducting TMDCs all have direct band gaps (in the monolayer form), with gap energies ranging from roughly 2 eV (WS_2) down to 1.6 eV ($MoSe_2$)[65]. This range of energies, spanning from red to near infrared (NIR) is very accessible from an optical spectroscopy standpoint and is technologically relevant as it approaches the frequency band used for short distance fiber optic communication, is intercompatible with several III-V semiconductor system, color centers in diamonds, and a host of other leading solid state systems. The energy gaps of these materials are also fully staggered, such that a junction formed by any two TMDCs will have P-N behavior (type II band alignment). Second, a robust valley pseudospin degree of freedom develops in monolayers due to a combination of strong spin-orbit coupling and broken spatial inversion symmetry[66]. Excitations of the valley pseudospin can be long lived, up to microseconds, and exhibit coherent evolution[67–69]. These properties and more are explored in greater detail in section 3.2-3.5.

3.2 Band structure of TMDCs from bulk to monolayer

Central to the study of any material is the structure of the energy levels of the electrons—particularly valence and bonding electrons. The emergence of a rich, many-level electronic structure is necessary due to the Fermionic nature of electrons and the imposition of the Pauli exclusion principle which prevents the overlap of these energy levels. The analysis of a system's energy levels begins with the construction of a Hamiltonian, the form of which varies considerably depending on the nature of the material. This Hamiltonian must take into account the large number of individual atoms out of which even a microscopic piece of an extended solid is constituted. The specific ways in which those atoms are bound together must be treated

appropriately (i.e. the valence structure of the atom and the bonding types which it permits). Spin-orbit and hyperfine interactions must be considered. The resulting Hamiltonian is incomprehensibly large and often intractable to solve directly for an arbitrary extended material, but a large subset of extended solids—crystalline solids—can be treated in a more straightforward way. Because the structure of the Hamiltonian is necessarily periodic for a crystal, Schrödinger's equation admits *periodic* solutions. This is the Bloch theorem and is central in solid state physics. Explicitly, the Bloch theorem can be expressed as follows:

> If a particle is subject to a Hamiltonian which is periodic in space, the (spatial) eigenfunctions this Hamiltonian have the form $\psi_{\boldsymbol{q}}(\boldsymbol{r}) = e^{i\boldsymbol{q}\cdot\boldsymbol{r}}u_{\boldsymbol{q}}(\boldsymbol{r})$, where **q** parametrizes the momentum of the state and $u_{\boldsymbol{q}}(\boldsymbol{r})$ is a function which is periodic in the lattice vectors of the crystal.

This result is quite general; no assumptions must be made about the nature of the particle or the potential in which it resides (assuming it is a physical potential). Complications arise in systems which consist of interacting particles, but for noninteracting particles, analysis with the Bloch theorem is useful. The eigenvalues produced by the Hamiltonian corresponding to each $u_{\boldsymbol{q}}$, which might be more suggestively be written as $E(\boldsymbol{q})$ form a series of energy surfaces in momentum space, the surfaces having dimensionality equal to the dimensionality of the crystal. This is the band structure of the crystal, and depending on the particle or quasiparticle in question, it can represent the energy levels of electrons within the crystal, vibrational modes (phonons) associated with atomic motion of the crystal lattice, excitations of the spin population of the crystal (magnons, spinons, skyrmions, etc.), or a plethora of other phenomena. Crucially, the states represented by points in the energy bands have a representation in terms of the Bloch functions (which, as eigenfunctions, form a complete basis); thus the bands can be decomposed into constituent modes and reconstituted in more physical terms. For example, electronic bands can be expressed as linear combinations of electronic orbitals, and vibrational bands can be expressed as linear combinations of normal modes corresponding to simple motion of individual or collections of atoms in the unit cell. The states which occupy the electronic band structure take on many of the characteristics of the orbitals out of which they are constituted, e.g. if part of an electronic band is wholly composed of a $3d_{z^2}$ orbital, it has an orbital magnetic number of

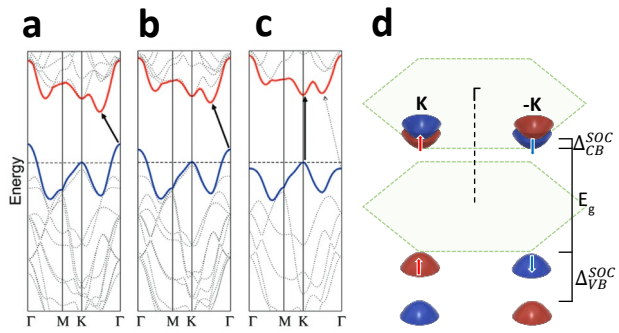

Figure 3.2.1 The band structure of semi-conducting TMDCs. **a-c** Evolution of the $MoSe_2$ band structure from bulk to bilayer and monolayer, respectively. Black arrows indicate the lowest energy transition. **d** K-point valleys in TMDC with spin-orbit coupling (SOC) in both the valence and conduction bands. Color-coding and arrows indicate the direction of electron spin in a given band.

$m_z = 0$, like the orbital itself. If it is composed of multiple orbitals, m_z may not be a good quantum number and a new basis for the orbital angular momentum may beneeded.

In this section, we will be focusing on the electronic band structure of TMDCs, and in particular on the energy bands which lie near the energetic boundary below which all states are occupied and above which all states are unoccupied, i.e. the Fermi level E_F. Deeply bound electrons in low-lying energy bands reside in the fully screened atomic cores which play a small role in the properties of materials compared to the outsized roles of electrons in bonding orbitals which are close to E_F. Similarly, electronic bands far above E_F, which under normal conditions are vacant, correspond to highly excited states of atomic orbitals which generally relax quickly. It is the low energy band structure, the bands nearest to E_F, which govern the most prevalent electronic properties of crystals. We will discuss the band structure of TMDs in the hexagonal representation of the Brillouin zone, one of several possible representations, and perhaps the most suggestive since it reflects the hexagonal shape of the crystal lattice. The low energy band structures of all four of the semiconducting TMDs are very similar (though the high energy band structure on either side of E_F necessarily varies because the different elemental constituents have different numbers of electrons); therefore we will first discuss the specific case of the band structure of MoS_2 as a representative of semiconducting TMDs, then elaborate on the differences between them.

The calculated band structure of bulk, bilayer, and monolayer MoS_2 are presented in figure 3.2.1 a-c[11]. The most prominent feature of this series is the upward shift of the conduction band (CB) Q-point valley (midway between the zone center and the zone corner) and the downward shift of the valence band (VB) Γ point (zone center) as thickness is reduced, which leads, in the monolayer limit, to the emergence of the valence band maximum and conduction

band minimum at the K point (zone corner) in both bands. The indirect-to-direct bandgap transition when cleaved down to a single layer occurs in all four members of the semiconducting TMDC family, and is driven by the loss of interlayer hybridization of the chalcogen orbitals which contribute to the VB Γ and the CB Q valleys[70]. By contrast, the K point valleys in both the CB and VB are comprised primarily of transition metal orbitals which are protected by the chalcogen layers from interlayer hybridization; thus the K point valleys remain relatively stationary as layer number varies.

The orbital composition of the K point has profound consequences for the band structure and electronic properties of TMDCs. Given the high atomic mass of the transition metals and their d valence orbitals, we would expect spin-orbit coupling to play a role in determining the electronic energy levels. Simple symmetry analysis gives us clues about how the spin-orbit coupling should manifest. The only mirror symmetry of the lattice is along the out-of-plane normal, indicating that σ_z is the only good spin basis. Furthermore, the broken inversion symmetry and finite crystallographic momentum of the K points requires that spin-orbit coupling take opposite sign in valleys with opposite crystallographic momentum, giving rise to the notion of the valley index $\tau = \pm$, referring to the two *inequivalent* sets of K-points, related to each other by time reversal symmetry and forming an alternating pattern at the corners of the hexagonal Brillouin zone[66] (fig 3.2.1 d). Furthermore, orbital analysis of the K-point valleys indicates that the VB is comprised of transition metal $d_{x^2-y^2}$ and d_{xy} orbitals which have magnetic quantum number $m = \tau \cdot 2$, while the CB is comprised primarily of the $m = 0$ transition metal d_{z^2} orbital. This results in large spin-orbit coupling in the VB on the order of hundreds of meV[71]. A small amount of spin-orbit splitting arises in the CB due to higher-order orbital contributions, on the order of tens of meV. As suggested by the presence of the valley index in the magnetic quantum number, the spin orbit splitting is opposite in opposite valleys, locking band edge carrier spin to the valley index. Spin-valley locking also serves to suppress intervalley scattering, as it would require either a spin flip or substantial change in energy *in addition* to a large change in momentum.

Adding to the valley-contrasting effect of the orbital magnetic moment is the effect of Berry curvature. In 2D crystals with broken inversion symmetry, the Berry curvature in a band *n*

$\boldsymbol{\Omega}_n(\boldsymbol{k})$ can take non-zero values in the z direction[72,73]. This is because $\boldsymbol{k}$ and $-\boldsymbol{k}$ crystallographic momenta are related by both time reversal and parity operations, but $\Omega_{n,z}(\boldsymbol{k})$ is odd under time reversal and even under parity; thus only crystals for which parity is not a good operation can support non-zero $\Omega_{n,z}(\boldsymbol{k})$ in the absence of other symmetry breaking. The Berry curvature in TMDCs can be calculated from first principles using the massive Dirac Hamiltonian, for which

$$\Omega_{c,z}(\boldsymbol{k}) = -2\tau \frac{a^2 t^2 \Delta}{(4a^2 t^2 k^2 + \Delta^2)^{3/2}} = -\Omega_{v,z}(\boldsymbol{k}),$$

where $c(v)$ indexes the conduction (valence) band, a is the lattice constant, t is the hopping integral, and Δ is the band gap. The Berry curvature is maximized at the K points and carries opposite sign in opposite valleys due to their being related by time reversal[74,75]. The Berry curvature necessarily vanishes at Γ via the symmetry arguments made above. Berry curvature couples to electron wavefunctions with finite spatial extent (and thus nonzero distribution in the Brillouin zone) causing an effective rotation of the wavepacket and leading to a Valley magnetic moment, which is opposite for opposite valleys[76,77]. This effective magnetic moment in momentum space couples to magnetic fields in the same way that real magnetic moments would and can otherwise be treated in exactly the same way as, e.g., an orbital magnetic moment or spin magnetic moment.

3.3 Valley excitons in monolayer TMDCs

When a photon of sufficient energy is incident on a semiconductor, it has a chance to be absorbed and promote an electron from the valence band to the conduction band, leaving behind in the valence band a vacant state known as a hole with an effective positive charge. The photoexcited electron and hole will experience an attractive electrostatic interaction, and if the electron doesn't relax too quickly, they will form a bound state known as an exciton[78]. Moreover, if the momentum difference between the electron and hole is sufficiently small, e.g. the band gap is momentum direct, they may recombine by the emission of a photon, or *photoluminescence* (PL). Absent nonlinear processes, the minimum energy of the absorbed photon must equal the single-particle bandgap less the Coulomb binding energy in order to create an exciton. The emitted photon will carry this energy precisely (up to convolution by broadening effects), with

any excess energy having been deposited in the crystal lattice by electron-lattice interactions[78,79]. The photon energy also determines the allowed momentum mismatch, as the recombination of the electron and hole must happen within the light cone of the photon, defined by the photon momentum. The band gap of TMDCs is momentum direct, and in principle could give rise to bright exciton PL. However, there are other factors which determine whether an electronic transition will be optically bright.

To first order, the coupling between an electromagnetic field and an electronic orbital is governed by the electric dipole operator. The transition matrix element between two states k and l is given by

$$a_{kl} = i\frac{m^*(E_k - E_l)}{\hbar}\langle k|\hat{\epsilon}\cdot\vec{r}|l\rangle,$$

where m^* is the effective mass and $\hat{\epsilon}$ is the (complex) polarization vector of the electric field. It can be seen from the spatial operator that opposite parity for the initial and final states is required for the matrix element to be nonzero. The K-K interband transition in TMDCs is therefore dipole allowed since the transition metal $d_{x^2-y^2}$ and d_{xy} orbitals that constitute the K-point VB are odd and the d_{z^2} orbital that constitutes the K-point CB is even. Optical transitions are also subject to conservation of angular momentum, both spin and orbital. In $MoSe_2$, WS_2, and MoS_2 the upper spin-split VB and lower spin-split CB within a given valley have the same spin; thus the transition is spin allowed. However, in WSe_2, the spin split CBs have opposite order, giving WSe_2 a spin-dark ground state exciton[80,81]. However, because the spin splitting is relatively small (and thus the Boltzmann factor is relatively large), this makes the transition from the upper VB to the upper CB bright at elevated temperatures[82].

The broadband PL spectrum of MoS_2 is shown in figure 3.3.1 a[11], and shows two dominant peaks corresponding to the two spin-allowed K-point transitions in MoS_2: from the upper VB to the lower CB, and from the lower VB to the upper CB (fig. 3.3.1 b). These two transitions correspond to two distinct excitonic species of different spin/valley pairing, commonly referred to as the A and B excitons, respectively. But the impact of spin/valley physics in TMDCs goes far beyond the production of the A and B excitons. The valley-associated magnetic moments, both from the orbital magnetic moment and Berry curvature, give rise to an optical selection rule for circularly polarized light, whereby the +K valley can be excited by right circularly polarized light,

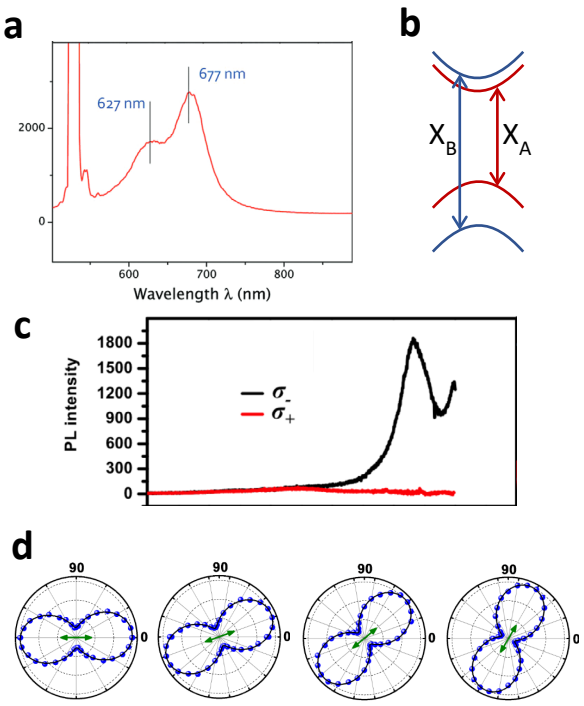

Figure 3.3.1 Valley physics in monolayer TMDCs. **a** PL spectrum of monolayer MoS_2 showing the A and B excitons. **b** Band schematic of a TMDC K point showing the electronic transitions corresponding to the A and B excitons. **c** Circularly polarized PL generated by circularly polarized optical pumping in MoS_2. **d** Polarization-resolved intensity plot of linearly polarized PL from WSe_2 excited by linearly polarized light. Green arrows indicate the excitation polarization axis. The PL polarization follows the excitation polarization as it is rotated.

and the -K valley can be excited by left circularly polarized light[66,67]. As discussed in section 3.2, the valley degree of freedom is protected by the large change in momentum and spin flip required for intervalley scattering. Thus, an exciton created by absorption of a circularly polarized photon will tend to stay within one valley, and upon recombination, emit a photon with circular polarization matching that of the absorbed photon. The photoluminescence of TMDCs is therefore co-circularly polarized with the excitation (fig. 3.3.1 c). In WSe_2, the valley coherence time is long compared to the radiative lifetime, allowing for the preparation of coherent superpositions of valley excitons by linearly polarized light and observation of linearly polarized photoluminescence with PL polarization axis set by the excitation axis (fig. 3.3.1 d)[68].

When TMDC monolayers are electrostatically doped, the formation of charged excitons (trions, if singly charged) is favored. Free charges bind to excitons through polar interactions, partially screening the binding energy; thus charged excitons appear at lower energies than neutral excitons (fig. 3.3.2 a)[83,84]. Both positive and negative trions can be seen. However, there are two different negative trions, X^- and $X^{-\prime}$, corresponding to triplet and singlet trions, respectively[85]. Besides the formation of these two distinct trion species, different combinations of spin and valley pairing produce a wide range of excitonic species in TMDCs, including the spin-dark ground state exciton in WSe_2, dark trions, singlet and triplet trions with intervalley carriers, and more (fig. 3.3.2 b)[86]. These states

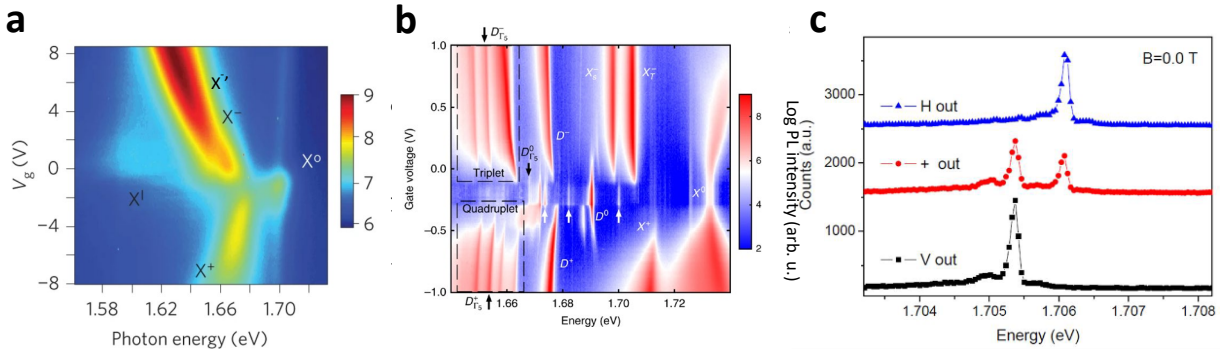

Figure 3.3.2 Excitonic species in TMDCs. **a** PL gate dependence of the PL spectrum in WSe_2 showing the three bright trion species along with the neutral exciton. X^l is the localized exciton (defect) band. **b** PL gate dependence of high-quality encapsulated WSe_2 shows large number of bright (X) and dark (D) excitons/trions with inter/intravalley character, along with several phonon sidebands at low energy (dashed boxes). **c** PL spectrum of a single defect emitter in WSe_2 shows cross-linearly polarized doublet behavior (H and V out) with no substantial circular polarization (+ out) in the absence of a magnetic field.

have low oscillator strengths and only become apparent in high-quality hBN encapsulated monolayers of WSe_2. TMDCs also host defect-localized excitons, in which an exciton binds to any number of different chemical, structural, or extrinsic defects. These defects typically manifest as low-energy, ultra-narrow emission peaks in the PL spectrum of TMDCs. Quantized light from defect-localized excitons has been observed. Many common types of defects break the 3-fold rotational symmetry of the lattice and thus destroy the optical selection rule for circularly polarized light. Such defects have longitudinal-transverse hyperfine splitting, producing a cross-linearly polarized, narrowly spaced emission doublet (fig. 3.3.2 c)[87–90].

4 - Diamagnetism of 2D excitons

In this chapter, we discuss studies of the electrostatic potential which binds electrons and holes to form excitons. In particular, we will focus on the use of the diamagnetic shift of excitons in 2D semiconductors to understand the effect of nonlocal screening and reveal the size and binding energy of excited states of excitons in 2D semiconductors. In turn this information can be used to verify or improve theoretical models of the attractive electrostatic potential. At very high magnetic fields, the cyclotron energy of the electron and hole bands become relevant and allow us to put tight bounds on the exciton's reduced mass. Experimental studies at high magnetic fields present unique challenges which will be addressed as well.

4.1 The Coulomb interaction in semiconductors

The most basic description of an exciton is an electron excited to an unoccupied band or orbital in a crystal, bound to the lattice by the Coulomb interaction with the positive hole left in its initial state in the valence band. The electrostatic potential which binds the electron and hole determines many of the fundamental properties of the exciton, most directly the binding energy, wavefunction size, and the spectrum of excited states (analogous to Rydberg levels in hydrogen) of the exciton. More subtle but nevertheless profound consequences of the electrostatic potential include the formation of charged excitons (positive and negative trions)[83,91], biexcitons[92,93] and larger excitonic "molecules"[94]. Indirectly, it influences the fine structure of excitons and many of the dominant scattering mechanisms which lead to decoherence and depolarization via the electron-hole exchange interaction[95–97]. It is therefore crucial to the theoretical understanding of excitons to know the form and parameters of their electrostatic potential.

As a simple model, we first consider the Coulomb potential which describes the interaction between two point charges of opposite sign separated by a distance r,

$$V(r) = -\frac{e^2}{4\pi\epsilon r}.$$

The fundamental challenge with this model is the interpretation of the dielectric constant ϵ when the separation r is similar to the spacing between atoms in the crystal. This challenge stems from the microscopic picture of dielectric polarization, in which individual molecular orbitals are polarized by an incident electric field according to their polarizability tensor γ_{ij}. In this case, each polarized orbital produces a local electric field which adds to the incident field. The dielectric constant is calculated by averaging the contributions of the polarized orbitals in the far field, and thus provides little to no information about the local electrostatic environment of a single charge embedded in a crystal.

There are two limits in which the effects of proximate polarized orbitals may be neglected. First, if the average electron-hole separation is large compared to the lattice constant, the dielectric screening of the material is well approximated by the macroscopic average described above[98,99]. This is the continuum model, in which many microscopic details are neglected from the exciton's 2-body Hamiltonian and are instead accounted for in the single-particle band structure that separately describe the electron and hole. That is to say, the 2-body wavefunction can be solved absent any consideration of individual orbitals and then mapped as an envelope function onto the single-particle Bloch states corresponding to the excited bands. Such excitons are called Wannier-Mott excitons[100]. The second such case occurs in the limit of the electron and hole having separation comparable to the size of atomic/molecular orbitals. Such excitons are called Frenkel excitons[101]. In this case, both the electron and hole reside within orbitals around the same lattice site and can be considered local excitations of particular orbitals. The spatial scale of the electric field produced by a Frenkel exciton is small compared to a lattice constant, and its dipolar electric field (outside the region between the electron and hole) falls off quickly. Thus, its effect on neighboring orbitals is relatively weak compared to the direct electron-hole interaction, and the nonlocal screening they provide may be neglected. However, in this limit, the polarizability of the core and semi-core electrons of the atoms involved in the Frenkel exciton cannot be neglected, and in general the modeling and calculation of Frenkel excitons is challenging[102].

Even when modeling Wannier-Mott excitons in the continuum limit, the dielectric environment of an exciton provides further complications. Firstly, as suggested by the tensor

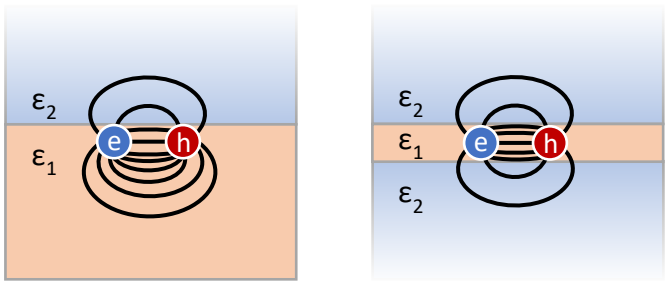

Figure 4.1.1 Dielectric screening of Wannier excitons at boundaries. **a** Exciton at the boundary of a semiconductor slab. The electric field lines are largely confined to the highly polarizable semiconductor. **b** Exciton confined in a thin semiconductor sheet.

form of the individual molecular polarizability γ_{ij}, the electric polarizability of a material χ_{ij} is itself a rank-2 tensor, such that polarization of the material is $P_i = \epsilon_0 \chi_{ij} E_j$. Anisotropy of χ_{ij} can be expected in anisotropic crystal structures. In inversion-symmetric crystals without broken time reversal symmetry, the off-diagonal terms $\chi_{i \neq j} = 0$, but uniaxial and biaxial crystal anisotropy allows the diagonal elements to take on distinct values, resulting in an ellipsoidal distortion of the electrostatic interaction. The second complication occurs at surfaces and edges of crystals, where, in addition to finite-size crystal effects, the dielectric boundary can strongly modify the electron-hole Coulomb interaction. If both the electron and hole reside at the surface of a semi-infinite dielectric slab against vacuum, the dielectric screening of their interaction is reduced by half (fig. 4.1.1 a). If they instead reside in a thin dielectric slab (thickness much smaller than electron-hole separation), the interaction is mostly unscreened (fig. 4.1.1 b). The loss of screening at boundaries results in a smaller, more tightly bound exciton, and effect which has been readily demonstrated in quasi-2D semiconductor quantum wells[103,104].

All of the complications listed above come into play when modeling excitons in atomically thin 2D materials: the size of the exciton is necessarily on the scale of the lattice constant along at least one direction, the material inherently has uniaxial, if not biaxial anisotropy, and the exciton necessarily resides at a dielectric interface. Consequently, the form and strength of the electron-hole Coulomb interaction is difficult to model *ab initio*. Absent a more sophisticated theoretical approach, the simplest model for the electrostatic potential [energy] of a hole in proximity to an electron centered in a thin dielectric sheet with uniaxial (out of plane) anisotropy is given by

$$V_K(r) = -\frac{e^2}{8\epsilon_0 r_0}\left[H_0\left(\frac{\kappa r}{r_0}\right) + Y_0\left(\frac{\kappa r}{r_0}\right)\right],$$

where $r_0 = 2\pi\chi_{2D}$ is the 2D screening length, $\chi_{2D} = d_s(\epsilon_{\parallel} - 1)$ is the 2D polarizability, d_s is the interlayer separation, $\epsilon_{\parallel}$ is the bulk dielectric constant in the plane of the sheet, κ is the average dielectric constant of the media surrounding the sheet, and H_0 and Y_0 are the Struve and Neumann functions of the first kind, respectively[105,106]. This potential is often referred to as the Keldysh potential, named for Leonid V. Keldysh. It is valid in the continuum model when the electron and hole are localized within a 2D plane, such that the distance between them is much larger than the size of their wavefunction perpendicular to the plane. In the limit of very large r, the potential converges to $-1/r$ dependence, and in the limit of very small r, the potential diverges logarithmically. This behavior can be understood intuitively in the following way:

- When the charges are far apart, the majority of the electric field lines which connect them pass through the space outside of the confining slab, and very little of the electric field is confined within the slab. Thus the geometry of the problem begins to approach that of two charges sitting at the interface between two semi-infinite dielectric slabs, the solution to which is scale-independent and has $-1/r$ dependence.
- When the charges are very close, the majority of the electric field lines which connect them are confined within the 2D slab, mirroring the behavior of electrostatics in a strictly 2D space, giving rise to the expected $\ln(r)$ dependence.

Naturally, almost all real systems fall in between these two limiting cases. In particular, the excitons in the semiconducting transition metal dichalcogenides (TMDCs) are predicted to have lateral sizes on the order of 1-2 nm[107], a size comparable to the layer thickness, and in a regime where it might not be appropriate to treat in the continuum limit nor as a fully localized excitation. In turn, this calls into question the applicability of the Keldysh potential to these systems and has made theoretical studies of the excitons they host challenging.

4.2 Probing the structure of excitons by static electromagnetic fields

The theoretical challenges described in section 4.1 motivate the need for experimental studies to test the validity of proposed models. However, this is made difficult by the limited

number of experimental tools available to study the structure and electrostatics of excitons. Due to their small spatial extent and transient existence, there is no way to directly image the size or map out the electric field of an exciton. There are, however, inferential tools that can be used to probe excitons and learn about these very fundamental properties. In particular, the coupling of an exciton to an external electrostatic or magnetic field can produce an energy shift which, in the case of the Stark shift and the diamagnetic shift, can reveal the size of the exciton's wavefunction.

When the binding energy of the exciton is large compared to the energy shift due to polarization by an external field, the field couplings may be treated perturbatively. The 1st and 2nd order perturbative Stark shift for the k^{th} orbital of the exciton in the center of mass representation (where k represents the full set of quantum numbers) is given by

$$E_{k,\mathrm{Stark}}(\boldsymbol{F}) = -eF_i\langle\psi_k|r_i|\psi_k\rangle - \frac{1}{2}e^2F_iF_j\sum_{k'\neq k}\frac{\langle\psi_k|r_i|\psi_{k'}\rangle\langle\psi_{k'}|r_j|\psi_k\rangle}{E_k - E_{k'}},$$

where $\boldsymbol{F}$ is the external electric field, e is the elementary charge, ψ_k is the wavefunction of the k^{th} orbital, E_k is the unperturbed energy of the orbital, and r_j is the position operator[108]. This is equivalent to calculating the difference in the Stark shift of the conduction and valence bands occupied by the electron and hole respectively, taking into account the sign difference between the Stark shift of the electron band and the hole band. In this case, k is the set of quantum numbers composed of the band indices and the crystal momentum, and ψ_k is the associated Bloch wavefunction.

Generally speaking, the linear Stark effect for excitons vanishes due to mirror and axial symmetries of the spatial wavefunction, but the quadratic shift is universally non-vanishing. For *s*-wave excitons, the linear Stark shift is proportional to the permanent dipole moment. The quadratic Stark shift is proportional to $\langle r_i^2\rangle$, where r_i is the spatial operator along the direction of the applied field, and can be thought of as resulting from the coupling of an *induced* electric dipole moment to the external field. Thus, the quadratic Stark effect can be used as a probe of the size of the exciton's wavefunction along a particular direction. However, there is a considerable challenge to implementing this effect experimentally when the electric field is applied along a bulk direction of the crystal, namely that a sufficiently strong electric field to

produce a measurable Stark shift will also drive charge separation, leading to significant screening of the electric field. If charges are confined along one or more directions, as is the case for low-dimensional materials, bulk screening is significantly reduced along the direction of confinement and the Stark shift can in principle be measured. However, for excitons in TMDCs, the wavefunction is confined to the metal d orbital which lie within a single atomic layer and has negligible size in the out-of-plane direction, making the Stark shift unmeasurably small with the electric fields that are currently achievable using 2D materials. Sufficiently large electric fields to produce measurable quadratic Stark shifts often exceed material breakdown field limits for solid state materials, but can be useful in the study of atomic systems[109].

It is somewhat coincidental that the linear Stark shift is able to reveal structural information via the exciton's electric dipole moment. This is because the emergence of an electric dipole moment is caused by *spatial* symmetry breaking and does not arise as a consequence of intrinsic electrostatic moments of particles. However, this is not the case for linear magnetic field coupling, thanks to the presence of magnetic moments of spins and quantized orbital angular momentum that *are* intrinsic to particles. The linear magnetic field coupling of a closed shell state is known as the Zeeman effect, and is independent of structural factors, instead depending only on spin and orbital quantum numbers and the applied magnetic field. The energy shift of a given state is given by

$$E_{Zeeman}(B) = \mu_B g_L m_j B,$$

where μ_B is the Bohr magneton, g_L is the Landé g-factor inclusive of spin and orbital contributions, m_j is the total magnetic quantum number in the basis corresponding to the direction of the magnetic field, and B is the applied magnetic field strength[108]. The simplest approach to calculating the g-factor for particles and quasi-particles (such as excitons) in solid state systems is to calculate the orbital- or band-wise Zeeman shifts and sum over all involved particles. The spin-valley physics in TMDCs leads to good spin/angular momentum quantum numbers in the z basis. As discussed in chapter 3, the spin-allowed optical transition produces an $S = 0$ exciton, thus the only contributions to the g-factor are from orbital and valley magnetic moments, producing a g-factor of around -4.

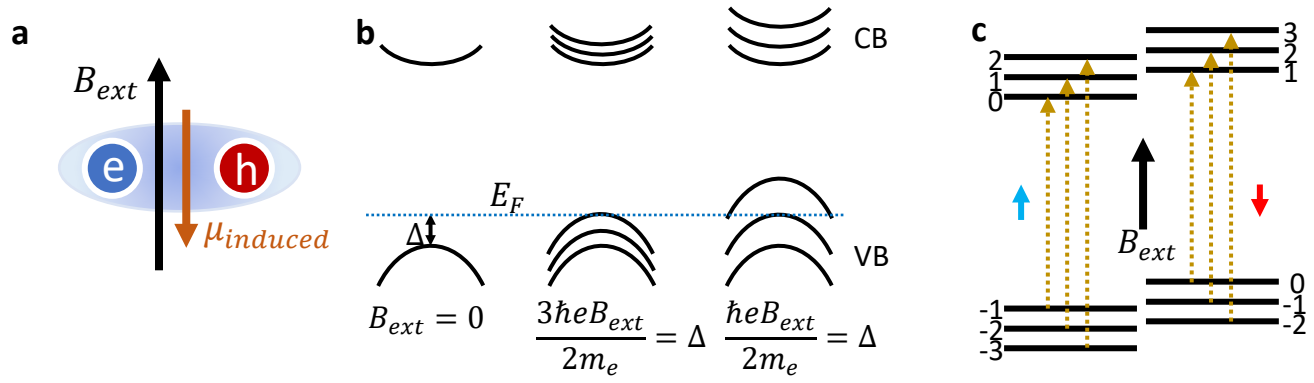

Figure 4.2.1 Diamagnetism of excitons. **a** Magnetic moment induced by an external magnetic field in an exciton. **b** Evolution of the 1st and 2nd valence band Landau levels in a semiconductor as they cross the Fermi level. **c** Allowed inter-Landau level transitions for spins aligned and antialigned to the magnetic field.

Analogous to the quadratic Stark effect, the quadratic coupling of a state to an external magnetic field can be thought of as the interaction between the field-induced magnetic moment and the field itself. Depending on context, this interaction can be paramagnetic or diamagnetic, the former corresponding to the parallel alignment of magnetic moments to the magnetic field and the latter corresponding to the antiparallel alignment of magnetic moments. There are numerous physical mechanisms which result in paramagnetism and diamagnetism which are situationally applicable. Generally speaking, a material or quantum system may have both paramagnetic and diamagnetic responses which add together to produce a net response depending on the size of both contributions. The only *universal* magnetism in closed shell systems is Langevin diamagnetism which results from the dynamical screening of magnetic flux by an electronic orbital, in a quantum analogy to Lenz's law (fig. 4.2.1 a). The resulting diamagnetic shift is given by

$$E_{Dia} = \frac{e^2}{8m_r}\langle r_\perp^2 \rangle B^2,$$

where $m_r = (m_e^{-1} + m_h^{-1})^{-1}$ is the reduced mass and $r_\perp$ is the position operator transverse to the magnetic field[110]. The diamagnetic shift is thus proportional to the cross-sectional area of the

state perpendicular to the magnetic field. For an s-wave state, the wavefunction envelope is rotationally symmetric and therefore

$$\langle r_{\perp}^{2} \rangle^{\frac{1}{2}} = \langle |r_{\perp}| \rangle.$$

It is important to note that this picture is only valid for closed shell systems and thus is inapplicable to the single-particle or single-band picture. Free charges in solid state systems instead experience Landau diamagnetism, in which the energy shift is proportional to the cyclotron frequency,

$$E_{Landau} \propto \hbar \left(N + \frac{1}{2} \right) \frac{e|B|}{m^{*}},$$

where m^{*} is the band-derived effective mass of the charge and N is the quantum number of the cyclotron orbit and takes integer values[110]. The quantization of this energy shift corresponds to harmonic orbitals with multiples of the cyclotron frequency, and occupancy of higher energy levels is made possible by Pauli exclusion. Crucially, this result is exact for a non-interacting Fermi gas and is fully compatible with single-particle band structure, where the quantization gives rise to Landau levels, replicas of the N=0 bands spaced by the cyclotron energy.

The consequences of Landau quantization in semiconductors and metals are well studied. In electronic transport measurements, it results in the Shubnikov-de Haas effect[111–114]: as the Fermi level is tuned through a series of Landau levels by electrostatic doping, or as Landau levels are tuned through the Fermi level by a changing magnetic field, the density of states at the Fermi level oscillates, producing oscillations in the longitudinal resistivity (fig. 4.2.1 b). Landau quantization also gives rise to the integer quantum Hall effect[2,115], which produces quantized plateaus in the transverse resistivity which eventually saturates at a perfectly quantized value of e^{2}/h. Notably, the Nobel foundation believes this effect to be important enough to merit the awarding of two separate Nobel Prizes in physics for discoveries related to the quantum Hall effect, first for the initial discovery and then again for its rediscovery in graphene.

Since both conduction and valence bands in a semiconductor are subject to Landau quantization, this raises the intriguing possibility of inter-Landau level optical transitions. Since

Landau levels correspond to angular momentum eigenstates, it must be that allowed inter-Landau level transitions conserve angular momentum. Since the hole left behind by an excited electron in a valence band Landau level will carry opposite angular momentum, it stands to reason that absorption of a photon must result in the excitation of the electron to a Landau level whose quantum number N is different from the absolute value of the original by exactly 1, i.e. from N=0 to N=1, N=-1 to N=2, etc. (fig. 4.2.1 c)[116].

4.3 Apparatus for high-field spectroscopy of 2D materials

The wavefunction envelope of a Wannier exciton in a 2D material can be calculated through the Schrödinger equation in the effective mass picture with the knowledge of a few key pieces of information, namely the effective masses of the electron and hole and the functional form and parameters of the electrostatic potential (or alternatively a numerical approximation). The latter can be determined from a calculated or measured band structure and the former can be *approximated* from first principles (e.g. the Keldysh potential discussed in section 4.1). This unfortunately leads to a situation wherein one must know ahead of time that the exciton wavefunction in sufficiently large for the macroscopic interpretation of dielectric polarization to be applicable in order to calculate the size of the wavefunction to begin with. One can always make an *ansatz* about the wavefunction size and proceed with the calculation, or infer binding energy from optical absorption measurements, in which the binding energy is approximately equal to the difference in energy between the band edge and exciton resonance. These various methods of estimation and approximation have led to the approximate determination of the size, mass, and binding energy of excitons in TMDCs with limited accuracy and precision, all relying on assumed models with multiple free parameters, each relying on an estimated value[107,117].

As discussed in section 4.2, the quadratic diamagnetic shift of provides a model-free approach to determining the size of an exciton with just a single free parameter: the reduced mass. The diamagnetic shift can be measured optically by tracking either the resonant absorption or photoluminescence emission energy of the exciton[118–120], an approach which has been widely used in various conventional 3D and quasi-2D semiconductor systems[120–122]. In III-V

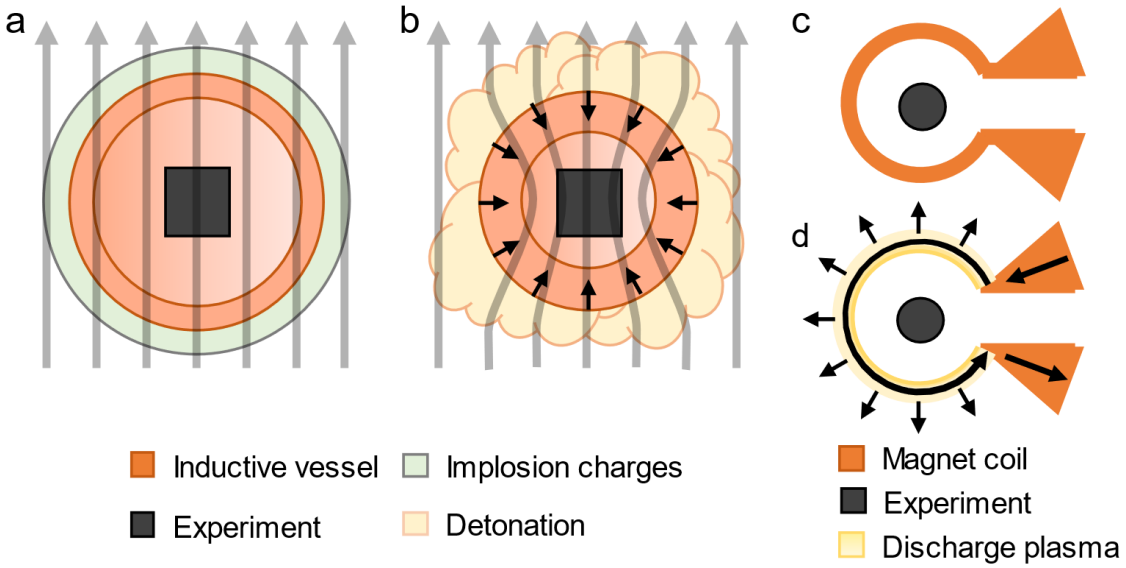

Figure 4.3.1 Destructive apparatus for achieving high magnetic fields. **a** Implosion magnet prior to detonation, immersed in an external magnetic field. **b** Implosion magnet after detonation. The imploding inductive vessel confines and concentrates the magnetic flux. **c** Single turn magnet prior to discharge. **d** Single turn magnet during discharge after coil is flashed to plasma.

semiconductor quantum wells, the exciton radius is on the order of 10 nm (depending on the well thickness)[123] and the reduced mass (heavy-hole exciton) is about 0.05 m_e[124]. For the diamagnetic shift to be determined accurately, the magnitude of the shift should be comparable to the linewidth of the exciton resonance. In the case of III-V quantum wells, this requires a magnetic field of around 10 T, which is easily accessible for tabletop experiments using superconducting solenoid magnets. However, for monolayers of TMDCs, the estimated radius is on the order of 1.5 nm, the estimated mass is approximately 0.2 m_e, and best achievable linewidths in absorption experiments is typically about 2 meV, thus requiring a magnetic field strength on the order of 100 T to achieve the same fractional diamagnetic shift, which is far from achievable in the laboratory. There are, however, a few different approaches to produce such large magnetic fields in specially equipped dedicated research facilities.

The earliest approach, also the approach capable of producing the largest magnetic fields, is through flux confinement in implosion magnets[125]. The operating principle of implosion magnets is uniquely destructive, as the name suggests: The sample and measurement equipment are placed at the center of a typically spherical or cylindrical metal confinement shell, which is surrounded by shaped explosive charges. The assembly is placed in a moderately strong magnetic

field generated by a resistive solenoid magnet, usually on the order of a few Tesla (fig. 4.3.1 a). The experiment begins when the shaped explosive charges are detonated, causing the metal shell to implode around the sample. The integrated magnetic flux contained by the shell is momentarily conserved due to a reactive electric current produced by the Lorentz force on electrons in the shell (i.e. Lenz's law). The faster the motion of the shell walls and the less resistive the shell, the greater the degree of flux confinement will be. As the flux is largely conserved but the perpendicular cross sectional area of the confined volume decreases, the field strength is increased proportionally. If mechanical failure of the shell can be avoided (so as to prevent the "opening" of the circuit of the reaction current), the strength of the confined field will diverge like $1/r^2$, producing incredibly large magnetic fields, up to *thousands* of Tesla (fig. 4.3.1 b). The downsides of such experiments are obvious: they inevitably lead to the complete destruction of the sample and any measurement equipment which must be within the confined volume. The success rate for these experiments is low, as asymmetric explosions and premature mechanical failure of the confinement shell will result in failure to achieve the desired magnetic field or premature destruction of the sample. Furthermore, the duration of the experiments is typically only a few microseconds, requiring perfect timing and fast data acquisition, which were extremely difficult to achieve at the time of the development of this technique.

A somewhat less catastrophically destructive apparatus for generating extreme magnetic fields is the destructive split ring/single turn magnet[126,127]. The magnetic field is produced by passing a large electric current, supplied by discharging a large parallel array of capacitors, through a single split circular ring of copper (fig. 4.3.1 c). The initial Joule heating is sufficient to vaporize and turn the split ring into a plasma, increasing the conductivity of the current channel and further increasing the strength of the magnetic field it produces. Meanwhile, the outwardly directed Lorentz force acts on the current channel, causing the plasma loop to expand and eventually blow itself apart (fig. 4.3.1 d). The pulsed magnetic field that can be produced in such magnets is on the order of hundreds of Tesla and persists for tens of microseconds. In the process, the conductive split ring which generates the magnetic field is destroyed, but the sample at its center, which is physically shielded from the exploding plasma, typically survives the experiment, allowing it to be repeated once the split ring is replaced. Like with implosion

magnets, the short timescale of the experiment demands precise synchronization of the experiment and the discharge and fast data acquisition, but because the experiment is fairly repeatable and survivable for the sample, it is a much more attractive approach for measuring materials in extreme magnetic fields.

However, neither of the approaches discussed above are especially well suited to optical study of TMDCs. Acquiring high-resolution optical spectrum data is typically done with a spectrometer equipped with a charge coupled device (CCD) array, which records a 1D or 2D image of the spectrally dispersed light in the spectrometer. The time required to read the image from the CCD and prepare it for subsequent exposure is on the order of 1 ms, and minimum exposure time is often limited to around 1ms as well, resulting in a maximum sampling rate of around 500 Hz. A longer duration magnetic field pulse is thus required for such optical experiments. Since the limitation on pulse duration for both of the above methods for generating high magnetic fields is the destruction of the sample or the source of the magnetic field, it stands to reason that a *non-destructive* approach is needed to achieve the pulse durations required for optical spectroscopy. An obvious way to achieve a non-destructive pulsed magnet is to supply a solenoid with a pulsed electric current, but there are significant engineering challenges for such a magnet capable of providing magnetic fields in the 100 T regime.

The first engineering challenge is the design of the solenoid itself (fig. 4.3.2 a). The magnetic field produced by a vacuum-core solenoid is $B = \mu_0 IN/l$, where I is the current passed through the solenoid, N is the number of loops in the solenoid, and l is the length of the solenoid. It is then tempting to design a solenoid with a very high winding density N/l in order to achieve a high field with a modest current. However, two problems arise: First, the resistance of the coil is roughly cubic in the turn density, assuming the turn density is adjusted by reducing the diameter of the wire while keeping the volume of the solenoid constant, thus requiring significantly higher voltage to achieve the same current. If the magnet current is sourced by a discharging capacitor array, capacitors must then be added in series to increase the achievable discharge voltage. This also means that, all other quantities being equal, the ratio between the dissipated power and the achievable magnetic field is proportional to $(N/l)^{-2}$, resulting in excessive Joule heating if the winding density is too high. Secondly, the inductance is quadratic

in the winding density, which slows down the response time of the system. Since the solenoid and capacitor array together form an RLC circuit, and the capacitors used are typically polar, the system must be overdamped in order to avoid current oscillation resulting in reverse-biasing the capacitors. Consequently, the pulse duration for a high-inductance solenoid will be very long, and the dissipated energy will be linear in the pulse duration. This combination of factors means that solenoids with high winding density produce excessive Joule heating which raises the temperature of the coil substantially. Since the resistivity of metals increases with increasing temperature, this produces positive feedback which can cause a runaway increase in temperature, resulting in mechanical or electrical failure of the coil. Consequently, the design of high-field pulsed magnets tend towards lower inductance, higher current coils.

This leads to the next engineering challenge: The Lorentz force on the coil in high field magnets is necessarily large and grows like I^2, which means that at some point, reducing the winding density to produce a more efficient, higher current magnet will increase the mechanical stress on the magnet to the point of mechanical failure. The proper design of the coil must take this into account and balance it against the need to minimize Joule heating, and there exists an optimal winding density at which the mechanical design can cope with the stress and the Joule heating is sufficiently low to not overheat the magnet.

The final engineering challenge is the provision of a cryogenic environment. Very often in condensed matter physics, and as is the case for TMDCs, it is beneficial for experiments to be carried out at cryogenic temperatures. Thermal broadening of an electronic resonance at room temperature is on the order of 25 meV, and since the expected diamagnetic shift of the ground state exciton in TMDCs is only a few meV even at 100 T, it is necessary to cool the sample to liquid helium temperatures to achieve the required spectral resolution to measure the diamagnetic shift accurately. The incorporation of the magnet within a cryostat assembly is also beneficial to the performance of the magnet. If the magnet is cooled by a liquid nitrogen reservoir as part of the cryostat's radiation shield assembly, its resistance will be reduced by up to an order of magnitude compared to room temperature if the coil is made from high-purity copper[128]. This means that, given a fixed design peak current, the coil density and therefore achievable magnetic field can be increased by approximately a factor of 3 while dissipating the same power. The

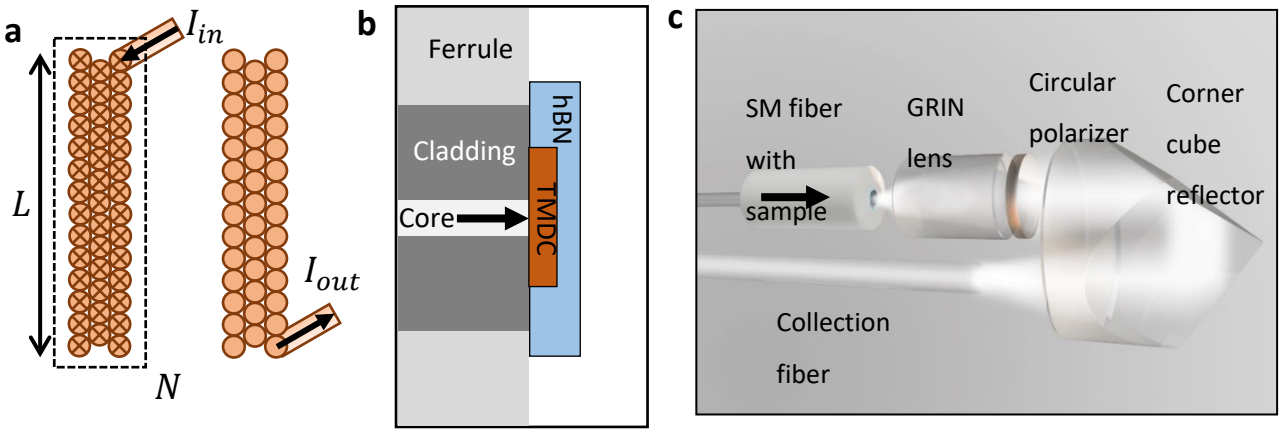

Figure 4.3.2 Non-destructive pulsed magnets. **a** Schematic of solenoid magnet coil. **b** Cross-sectional schematic of TMDC sample on a single mode optical fiber. Arrow indicates direction of light propagation. **c** Component layout of optical probe for measuring circularly-polarized transmission spectrum of fiber sample. Arrow indicates direction of light propagation.

discharge of the magnet will necessarily heat the magnet, which will then need to be recooled by the nitrogen reservoir.

Magnets of this type can be found in a number of research facilities around the globe, most notably in Los Alamos National Laboratory's National High Magnetic Field Laboratory – Pulsed Field Facility (LANL NHMFL-PFF) where the first magnets of this type were developed. There are a number of these magnets available at LANL NHMFL-PFF, each equipped with a liquid-nitrogen-jacketed helium bath cryostat to enable measurement of samples around 4.0 K (and optionally a ^{3}He insert to achieve 400 mK) with the following field configurations: 100T for 15 ms , 65 T for 16 ms, or 60 T for 100 ms. The listed pulse durations are calculated as the full-width half-max of the field pulse waveform. For the magnet offering 60 T for 100 ms, a flat-top profile is achieved for the full 100 ms following a gradual buildup in field strength.

The work described in the following sections was carried out using the 65 T magnet at LANL NHMFL-PFF equipped with a 4.0 K helium bath cryostat. The magnet is energized through the discharge of a 19 MJ capacitor bank. The lower limit for the bath temperature is determined by the boiling point of liquid helium at the reduced atmospheric pressure at LANL due to its elevation. The diameter of the cold bore of the cryostat is only 15 mm (reducing the magnet diameter reduces Joule heating), making optical access by free-space optical coupling

challenging. But by far, the larger challenge to free-space optical coupling is the intense vibration created by the discharge of the magnet which results from the self-force of the coil and the inductive force of the magnet on the conductive material around it (including the cryostat components). The design of measurement probes must be robust to vibration and optical access must be achieved by optical fibers.

As mentioned previously in this section, the diamagnetic shift of an exciton can be measured by tracking either the absorption resonance or the photoluminescence energy of the exciton as a function of applied magnetic field. The low quantum efficiency of monolayer TMDCs, especially for WSe_2 and WS_2 which have spin-dark ground states due to their inverted spin-split valence band ordering, results in a relatively weak photoluminescence signal requiring exposure times on the order of a few seconds for CCD-based spectrometers. It is therefore infeasible to use photoluminescence spectroscopy to track the exciton's energy during a magnetic field pulse with a duration of a few tens of ms. On the other hand, absorption spectroscopy, whether realized through transmission or reflection geometry, yields a signal strength independent of the illumination intensity and a signal to noise ratio determined by the noise level of the measurement instrument. In other words, in photoluminescence, there is an upper limit to the number of photons which can be collected by the spectrometer in a given time, which is limited by the sample itself, setting a relatively low limit on the signal to noise ratio for short exposure times. On the other hand, the signal to noise ratio for absorption measurements is limited only by the intensity of the light source and the collection efficiency, independent of the exposure time. It is therefore easier by far to probe the diamagnetic shift of the exciton using absorption spectroscopy.

A key challenge specific to carrying out this type of measurements with 2D materials is the small size of mechanically exfoliated flakes, typically on the order of 100 μm^2, which requires the use of microscopy for optical measurements. In turn, this means that the sample must be spatially aligned to a focused light beam, usually *in situ* to compensate for drift that might occur due to thermal expansion as the sample is cooled down from room temperature to cryogenic temperatures. The small size of the experimental bore in the high field magnet makes this approach infeasible. Earlier work of this nature was carried out using thin epitaxial films of

TMDCs[118], a few mm in lateral size, which eliminated the need for careful alignment, but the optical quality of such films is low due to inhomogeneous broadening arising from strain, chemical inhomogeneity, structural and chemical defects, and the presence of overlapping multilayers and amorphous seed sites[129–131]. The highest optical quality samples of monolayer TMDCs are mechanically exfoliated and encapsulated by hexagonal boron nitride (hBN) which serves as an atomically flat dielectric substrate. Such samples can exhibit linewidths more than an order of magnitude smaller than epitaxial films[132,133].

To capitalize on the benefits of using exfoliated flakes and overcome the challenges of acquiring and maintaining focus on a microscopic sample, we designed a new sample probe in which the sample itself was affixed to the core of a single-mode optical fiber (fig. 4.3.2 b). The method for sample preparation is described in section 2.3. The probe itself consisted of the single mode fiber with attached sample, through which white light is transmitted, a graded index lens to collimate the transmitted light, a circular polarizer with fixed helicity, a retroreflecting corner cube to redirect the transmitted light, and a large-diameter (0.5 mm) multi-mode optical fiber to couple the redirected transmitted light back out of the sample probe. These elements were held in place by a plastic bracket assembly and affixed to the end of a long fiberglass rod. A magnetic field sensor and temperature diode were affixed to the end of the probe to read off the sample conditions during the experiment. The probe stick was loaded into a vacuum tube, evacuated, and filled with rarefied helium to serve as exchange gas and provide cooling to the sample (fig. 4.3.2 c). The vacuum tube was lowered into the helium bath cryostat in the magnet bore. The optical fibers were then connected to long relay fibers running into the nearby optics lab. A laser-driven plasma light source was used to generate a white light continuum which, after having UV components removed by a spectral filter, was coupled into the single mode fiber via the attached single-mode relay fiber. The light returning via the multimode fiber and its attached relay fiber was coupled into a Czerny-Turner spectrometer with a liquid-nitrogen cooled CCD array.

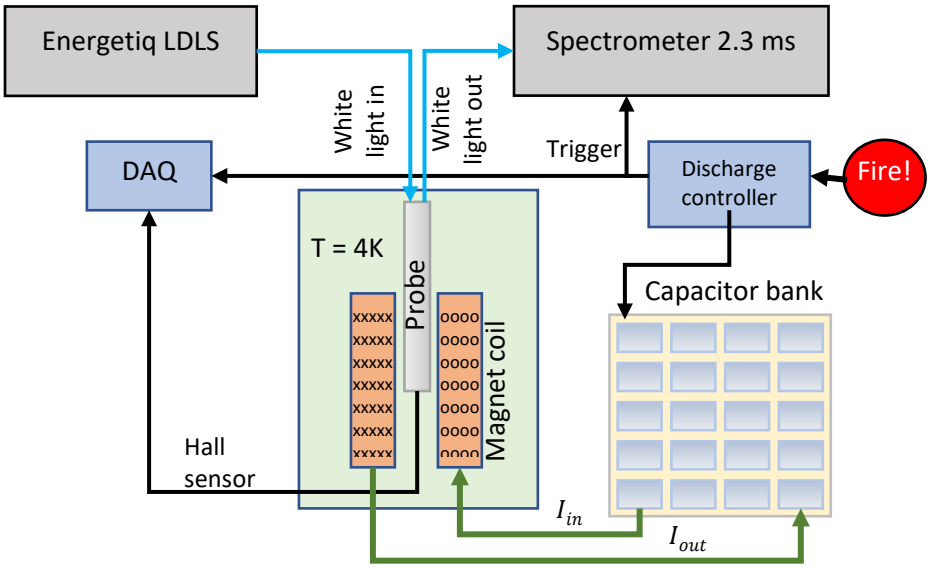

Figure 4.3.3 Experimental block diagram for measuring the white light transmission spectrum spectrum of a 2D semiconductor in a cryo-magnetic probe.

The experiment begins with the charging of the capacitor bank. Once the capacitor bank is charged, the user presses a button which sends a trigger signal to the magnet controller to initiate the "shot," the synchronized discharge of capacitor bank through the magnet and collection of data. The same trigger signal is routed in parallel to a pair of delay timers, which after a programmable delay, trigger data collection by the spectrometer CCD and by a data acquisition board connected to the magnetic field sensor attached to the sample stick. The delays of the various trigger signals are synchronized so that the instantaneous magnetic field reading can be precisely correlated to the frames recorded by the spectrometer, which collects data continuously during the shot (fig. 4.3.3). A short CCD exposure time is used (about half of the readoff time/sampling period) in order to measure a semi-instantaneous spectrum rather than a spectrum averaged over the entire sampling period, during which the magnetic field and the spectrum may change significantly. This measurement scheme allows for acquisition of a series of spectra as the magnetic field increases towards its maximum and then recedes, producing a field dependent data set. However, because the field changes rapidly in time around the field maximum (up to 15 T/ms), data points in proximity to the highest fields are sparse. However, the ability to adjust the trigger delay and the excellent repeatability of the field pulse enable multisampling: the field pulse can be repeated with different trigger delays in order to acquire

data at field values in between previously recorded data points. Unfortunately, due to long time (up to an hour) needed for the magnet to cool down between shots, it is impractical to multisample with more than one or two interstitial delays.

4.4 Experimental measurement of the diamagnetic shift of 2D excitons

The individual spectra collected throughout the shot represent the net spectral distribution of the transmitted light at a given magnetic field value, which is the multiplicative product of the spectrum of the light source, the combined transmittance spectra of all of the optical components, the efficiency of the spectrometer and CCD, and the transmission spectrum of the sample itself. These convolving factors are typically removed in an experiment by dividing the data by the sample-free background spectrum, collected with identical experimental parameters, just absent the sample itself. This is unfortunately not possible in our experiment as the sample can't be removed from the single mode fiber without destroying it, and because of variations in the transmission spectra between single mode fibers, it isn't possible to simply swap out the sample fiber for a blank fiber to acquire a background spectrum. As an alternative, the background spectrum can be reconstructed inferentially based on three requirements: First, that the background spectrum is mostly independent of magnetic field (it can experience spectrally uniform intensity fluctuations); second, that the spectral feature(s) from the sample are localized to a wavelength region $\lambda_1 < \lambda < \lambda_2$ at zero magnetic field; third, that at a sufficiently high magnetic field, the spectral feature(s) from the sample fully shift outside of the region between λ_1 and λ_2. If these conditions are satisfied, at magnetic fields in which the third criterion is satisfied, the wavelength region between λ_1 and λ_2 can be sampled *free from the influence of the sample* and used to replace that spectral region at zero magnetic field, effectively patching over the exciton resonance at zero field to produce a background spectrum. Given the expected diamagnetic shift of 1-2 meV at maximum field and a best-case-scenario absorption resonance width of 4 meV, it would seem that the third condition would not be met; the absorption peak would still overlap its zero-field position at the highest magnetic field. Fortunately, the valley Zeeman effect produces a shift (for a single valley) of around 7.5 meV at 65 T, shifting the absorption peak well away from its zero-field position. The transmission data presented from

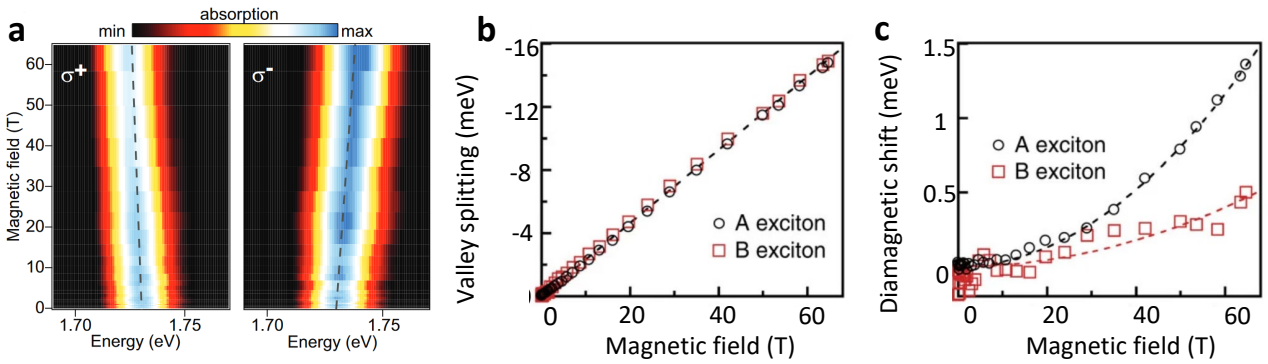

Figure 4.4.1 High field optical spectroscopy of a 2D semiconductor. **a** Color map of *A* exciton resonance from either valley shifting in a magnetic field. **b** Difference in energy between valleys vs. magnetic field for the *A* and *B* excitons, shifting as a result of the valley Zeeman effect. **c** Average energy of the *A* and *B* excitons vs. magnetic field.

here on are normalized T/T_0 spectra, with T_0 constructed as described above when possible, or by interpolating across the exciton resonance using a cubic spline fit when the resonance width is too large for reconstruction.

To decouple the Zeeman effect and the diamagnetic shift, it is helpful to have data constituting a time-reversal pair. Zeeman splitting, in the absence of other time-reversal symmetry breaking, can be defined as either $\Delta_{Zeeman}(B) = E_{\uparrow}(B) - E_{\uparrow}(-B)$ or $\Delta_{Zeeman}(B) = E_{\uparrow}(B) - E_{\downarrow}(B)$, where the arrows denote the orientation of magnetic moments for the time-reversal pair. In the context of TMDCs and the valley Zeeman effect, it is more suggestive to write it as $\Delta_{Zeeman}(B) = E_{+}(B) - E_{+}(-B)$ or $\Delta_{Zeeman}(B) = E_{+}(B) - E_{-}(B)$, where E_{+} (E_{-}) indicate the energy associated with the transition in the +K (-K) valley. For this experiment, it is much more convenient to measure the energy of a single valley at positive and negative magnetic fields than it is to measure opposite valleys at the same magnetic field, simply because the polarization optic is fixed to the cryogenic probe and would require a lengthy thermal cycle to change. Therefore, each data set presented consists as two separate shots with positive and negative field (note: the direction of the field is reversed by switching the direction of current flow rather than charging the capacitor array with opposite polarity, since the capacitors used are polar). The data set collected during a shot is most clearly represented as a 2D colormap, where the color of each pixel represents the signal strength and the horizontal and vertical axes represent the recorded energy and magnetic field values respectively (fig. 4.4.1 a).

Data analysis is carried out by first interleaving multisampled shots and then concatenating positive and negative field shots together. The data set is then normalized to the reconstructed T_0 spectrum. For presentation purposes, color maps are interpolated along the B axis using nearest-neighbor interpolation due to the inconsistent field spacing of the raw data. For quantitative analysis, no B interpolation is used. The data are then fit using either a Gaussian function or a numeric Voigt function, implemented with normal regression techniques. A table of the field-dependent exciton resonance energy $E(B)$ is then generated. Because of the excellent repeatability of the magnetic field waveform and the use of precision timing equipment, the discrepancies in the recorded field points between the positive and negative field shots are small (< 0.5 T for shots near the maximum field rate of change, average of < 0.1 T across all recorded data), generally being less than half the size of the field change during the spectral integration period. It is then possible to separate out the functionally odd and functionally even components of the field dependence by calculating $\Delta(B) = E(B) - E(-B)$ and $\bar{E}(B) = [E(B) + E(-B)]/2$, which should correspond to the Zeeman splitting (fig. 4.4.1 b) and the diamagnetic shift (fig. 4.4.1 c), respectively. The Zeeman splitting is well fit by a linear model with the energy intercept fixed to $\Delta(0\ \mathrm{T}) = 0\ \mathrm{meV}$. The even component of the energy shift $\bar{E}(B)$ is well approximated by a quadratic fit, whose parabolic coefficient can be directly related to the perpendicular size of the exciton, assuming the mass is known:

$$\bar{E}(B) = \alpha B^2 = \frac{e^2}{8m_r}\langle r_\perp^2 \rangle B^2.$$

4.5 Nonlocal screening of 2D excitons

The screened Keldysh potential, introduced in section 4.1, reflects the electrostatic potential of a charge embedded in a 2D dielectric slab with screening length $r_0 = 2\pi\chi_{2D}$, surrounded by uniform dielectrics on either side with average relative dielectric constant κ. Therefor the binding energy and the radius of a 2D exciton will depend on these two material parameters. Although not explicitly stated above, dielectric constants are dependent on frequency/photon energy, and the relevant energy scale for the calculation of excitons is that of

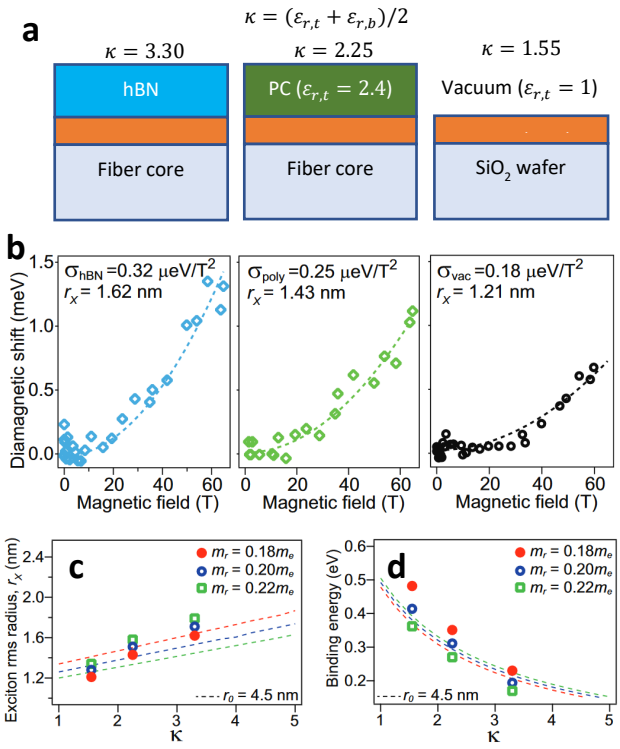

Figure 4.5.1 Effect of dielectric screening on 2D excitons. **a** Schematic of samples in different dielectric environments. **b** Diamagnetic shifts of the samples depicted in panel **(a)**. **c** Exciton radius and **d** binding energy for each sample calculated from their diamagnetic shift at select reduced masses.

the binding energy of the exciton. First principles calculations indicate that the excitons in TMDCs should have a binding energy of a few hundred meV (depending on degree of screening)[117], and so dielectric constants in this region of the IR are used.

To investigate the influence of a 2D exciton's dielectric environment on its size and binding energy, several samples with different dielectric environments were measured. The first sample was a monolayer of WSe_2 with a layer of hBN on one side and the fused silica optical fiber on the other, having an average dielectric constant $\kappa = 3.30$[134,135]. The second sample was a monolayer of WSe_2 with a film of polycarbonate on one side and the fused silica optical fiber on the other, with $\kappa = 2.25$[136]. The third sample was a thin film of epitaxially grown (through chemical vapor deposition) WSe_2 on a thermal silica substrate with vacuum on the other side, with $\kappa = 1.55$[134]. Notably, the third sample was measured in a slightly different way as it was used as-grown on an opaque substrate (fig. 4.5.1 a). A separate sample probe which uses reflection geometry was used, following the work of McCreary *et al*[118]. Analysis of the transmission or reflection spectra from the three samples yields consistent g-factors of around -4.05 ± 0.1, in agreement with values previously reported in the literature, and diamagnetic shift coefficients $\sigma_{hBN} = 0.32 \pm .02\ \mathrm{meV/T^2}$, $\sigma_{poly} = 0.25 \pm .02\ \mathrm{meV/T^2}$, and $\sigma_{vac} = 0.18 \pm .02\ \mathrm{meV/T^2}$, respectively (fig. 4.5.1 b). To convert the diamagnetic shift coefficients into calculated exciton radii, the reduced mass of the state must be known. The hole effective mass (derived from the valence band) has been determined experimentally through angle-resolved photoemission spectroscopy (ARPES)[137]

and both the electron and hole masses have been determined theoretically from tight binding[138]. Density functional theory has been employed to calculate the reduced mass more directly[107]. Based on these previous works, a value of $m_r = 0.18\, m_e$ is assumed in this section unless otherwise specified. Using this value for the reduced mass yields exciton radii of $r_{hBN} = 1.62$ nm, $r_{poly} = 1.43$ nm, and $r_{vac} = 1.21$ nm, respectively.

More sophisticated analysis can be performed by numerical evaluation of the Schrödinger equation using the screened Keldysh potential. The free parameters in the Hamiltonian are the reduced mass m_r, the 2D polarizability χ_{2D}, and the average surrounding dielectric constant κ. Using a theoretically predicted value for χ_{2D}[117] and leaving κ and m_r as free parameters, the exciton size (fig. 4.5.1 c) and binding energy $-\langle V \rangle$ (fig. 4.5.1 d) can be calculated (dashed lines) and compared to values calculated from the experimentally determined diamagnetic shift (symbols). To determine the binding energy from the diamagnetic shift, the radius for a given mass is calculated, and the solution to the Schrödinger equation which yields the calculated radius is used to then calculate $-\langle V \rangle$. Using the nominal reduced mass of 0.18 m_e, the resulting binding energies vary from about 240 meV up to 490 meV, depending on dielectric environment. This range of energies justifies the prior ansatz about the use of IR dielectric constants. Interestingly, the optical transition energy is essentially independent of the binding energy, a fact which has been attributed in other studies to bandgap renormalization due to dielectric screening.

Crucially, the radii determined from the measured diamagnetic shift depend only on the assumed mass and are model independent, while the calculated solutions depend on key assumptions about the form of the electrostatic potential and the applicability of a macroscopic model of dielectric susceptibility (and thus the use of macroscopic polarizability values). It is clear from this comparison that the calculated solutions somewhat underestimate the degree to which dielectric screening effects impact the exciton wavefunction and binding energy, as shown in figures 4.5.1 c-d, pointing towards deficiencies in the theoretical model widely used to calculate the properties of excitons in 2D materials, regardless of the value of assumed mass.

4.6 Testing the Keldysh potential: the non-hydrogenic Rydberg series of 2D excitons

As introduced in section 4.1, the functional form of the electrostatic potential which binds an electron and hole to form an exciton in a 2D semiconductor is substantially different from the hydrogenic potential which is responsible for the structure of atoms or excitons in 3D semiconductors. One consequence of this non-hydrogenic potential is seen in section 4.5, where the fundamental properties of the exciton, such as wavefunction size and binding energy, are shown to depend strongly on the surrounding dielectric environment. The other fundamental property of closed shell systems which might be expected to change with the modification of the functional form of the binding potential is the spectrum of excited states, analogous to the Rydberg series in atomic hydrogen. The simplest example of this is the comparison of the 3D hydrogenic model to the 2D hydrogenic potential. In the case of the former, the S-wave energy levels have eigenvalues

$$E_n = -\frac{\mathrm{Ry}}{n^2},$$

where Ry is the Rydberg energy, approximately 13.6 eV, and n is the principal quantum number. This solution is highly degenerate and incomplete, but the consideration of relativistic corrections and spin interactions leads to the notions of fine and hyperfine structure, which lift the degeneracy and give rise to the well-known ordering of s, p, d, and f energy levels, corresponding to different values of the azimuthal quantum number l. These levels are further split according to their magnetic quantum numbers m. Nevertheless, a key result of the hydrogen atom model is the ordering of energy levels primarily by the principle quantum number—that is to say, when comparing two eigenkets $|nlm\rangle$ and $|n'l'm'\rangle$, with $n \neq n'$, the ket with larger principal quantum number will have the larger energy eigenvalue of the two. By comparison, the logarithmic potential produces anomalous ordering of the energy levels E_{nl} according to their principal quantum number[139,140]. For example, in arbitrary units of energy, $E_{4,0} = 2.83 < E_{3,2} = 2.88$, and $E_{5,0} = 3.02 < E_{4,2} = 3.06$.

Given the similarities between the logarithmic potential and the Keldysh potential, we might expect similar behavior for 2D excitons. Anomalous ordering of energy levels has indeed been predicted in TMDCs, but direct optical evidence is difficult to obtain because transitions to

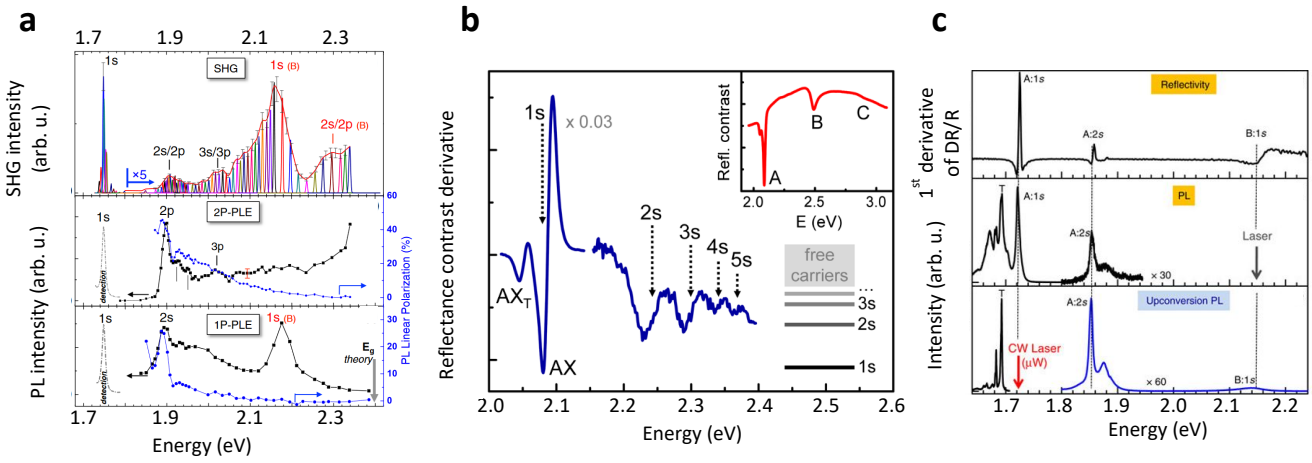

Figure 4.6.1 Spectroscopic evidence for excited states of excitons in TMDCs. **a** Excited s and p states appear in the second-harmonic generation spectrum (top panel), 2-photon photoluminescence excitation spectrum (middle panel), and photoluminescence excitation spectrum (bottom panel) of WSe_2. **b** Excited s states of the ground state exciton in WS_2 evident in reflectance contrast spectroscopy. **C** Excited s states of the ground state exciton in WSe_2 evident in reflectance contrast (top panel), photoluminescence (middle panel), and upconversion photoluminescence (bottom panel).

states with $l \neq 0$ are parity forbidden or require angular momentum greater than what can be imparted by a single photon, thus requiring brightening from symmetry breaking, coupling to vibrational modes, or multiphoton processes with weak cross sections. It would nevertheless be beneficial to the *theoretical* understanding of the structure and spectrum of 2D excitons to study the optically bright $l = 0$ excited states. There have been numerous reports of a series of high-energy optical resonances in proximity to the ground state exciton $X^0_{A,1s}$ in TMDCs, observed through a variety of linear and nonlinear optical spectroscopies (fig. 4.6.1 a-c)[52,141,142]. These resonances have been frequently assigned to excited states $X^0_{A,ns}$, where ns refers to the $l = 0$ energy level with principal quantum number n. This assignment has been largely based on comparing the energy spacings of the optical resonances with values predicted theoretically for the $X^0_{A,ns}$ states. However, some of these resonances have also been assigned to exciton-phonon complexes of $X^0_{A,1s}$ and phonons from the TMD layer and hBN encapsulating layers[143]. This assignment was based on photoluminescence excitation spectroscopy measurements and cast some doubt on the origin of these high-energy resonances in the absence of concrete evidence either way.

In the interest of clarifying previous results on excited states of excitons in TMDCs, the tools developed in section 4.5 offer a promising route forward. One hallmark of Rydberg states is increasing wavefunction size with increasing principal quantum number. Given the ability to measure exciton size in a model-free fashion, the diamagnetic shift of these resonances have the potential to reveal the nature of the high-energy resonances observed in TMDCs with tangible certainty, and in the process, enhance our theoretical understanding of the Coulomb interaction in 2D semiconductors. But there are significant challenges to measuring the high-energy resonances in the experimental context of a high-field study, chief among them the significantly reduced oscillator strength of the high energy states and tight requirements on sample quality needed to observe them. They are most prominent in samples consisting of a TMDC monolayer sandwiched between two relatively thick (> 5 nm) layers of hBN, the general consensus being that using hBN as an atomically flat substrate reduces the disorder potential which is typical of rougher substrates[142,144]. It is also necessary for the sample to be nearly charge neutral, otherwise trion formation is favored over the formation of neutral excitons and other neutral states. Charge doping can be introduced by chemical impurity, charge traps in the substrate, or electromechanically during fabrication. The presence of free or trapped charges can also change electrostatic screening (and therefore the exciton's radius and binding energy) by modulating the local polarizability[145].

To meet these requirements, electrostatically gated samples of monolayer WSe_2, sandwiched between two thick layers of hBN, were prepared on the tip of an optical fiber. The method for preparing these samples was similar to the previously described method (section 2.3) but with a few additional steps. The fibers are first prepared with a pair of metal gate electrodes by masking the fibers by hand using polyimide tape (fig. 4.6.2 a). The key feature of the gate pair is a narrow gap, approximately 50-100 μm wide, centered on the fiber core. It is in this gap that the sample will eventually be placed. The masked fiber is then placed in an electron-beam metal evaporator angled at 45°, so that one of the electrodes on both the fiber end face and cylindrical face are pointed towards the evaporation source (fig. 4.6.2 b). The fiber is then coated with 5 nm of chromium to serve as an adhesion layer, followed by 50nm of gold [note that since the fiber is angled 45° with respect to the path between the evaporation source and the fiber, the calibrated

thickness during the evaporation was scaled by a factor of $\sqrt{2}$.] The fiber was then rotated 180 degrees about its axis and the process was repeated in order to coat electrode which originally faced away from the evaporation source. Following evaporation, the polyimide tape was removed and the fibers cleaned with solvent, taking care not to allow the polymer fiber jacket to come in contact with the solvent so as to avoid degradation by the solvent. The van der Waals dry transfer technique described in (section 2.3) was used to assemble capacitively gated structures as depicted in figure 4.6.2 c, and deposited on the tip of the prepared optical fiber (fig. 4.6.2 d). The samples were then loaded in a modified version of the experimental probe described in section 4.5, equipped with a pair of conductors for gating the sample. The conductors were adhered to the gold electrodes on the fiber tip using silver paste.

Prior to beginning magnetic field dependent data, the transmission spectrum of each sample was measured as a function of applied gate voltage (fig. 4.6.2 f). The gate voltage was applied to the electrode attached to the graphite sheet parallel to the TMDC layer, while the electrode attached to the TMDC was grounded through a current preamplifier to detect any signs of dielectric breakdown or gate leakage. The gate-dependent spectra divide predominantly into 3 regimes, corresponding to the Fermi level residing within the valence band, within the gap, and within the conduction band. The spectra in the range of gate voltages over which the Fermi level is within the gap is dominated by absorption by the neutral $X^0_{A,1s}$, while the spectra in the range of gate voltages in which the Fermi level is in the valence or conduction bands are dominated by absorption by the positive and negative trions X^+ and X^-, respectively. The gate voltage corresponding to charge neutrality was assumed to be half way between the upper and lower thresholds of the voltage range over which the neutral exciton persists. The gates were then held at this voltage throughout the experiment. Magnetic field dependent data were collected and analyzed according to the methods described in section 4.5.

An example of a multisampled shot is shown in figure 4.6.3 a, in which a number of absorption resonances are observed to shift with the applied magnetic field. Based on the analysis that follows, we tentatively assign them to the 1s, 2s, 3s, and 4s energy levels of the neutral A exciton, in order of lowest energy to highest. The observed resonances were fit with

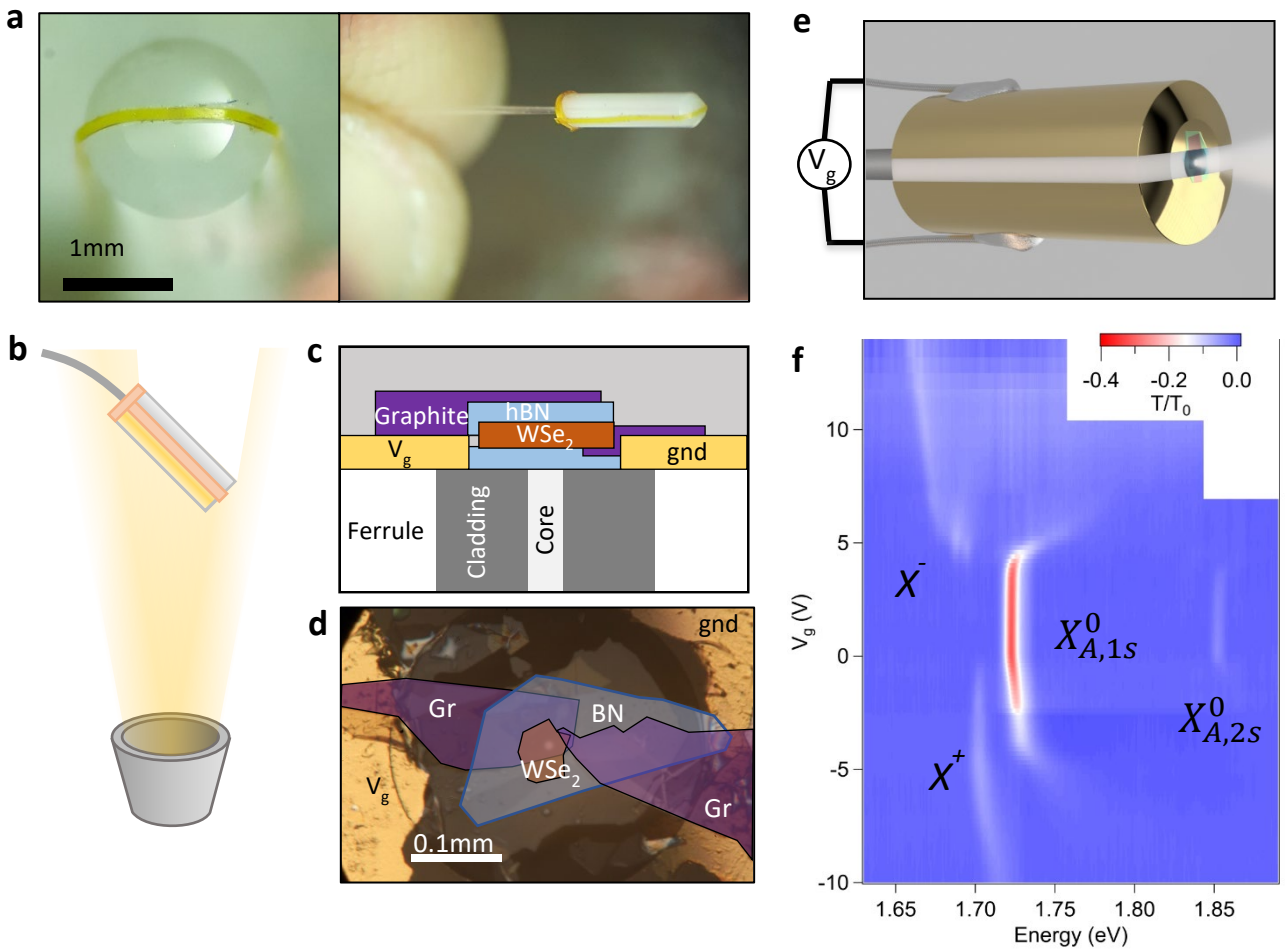

Figure 4.6.2 Fabrication of an electrostatically gated semiconductor sample on an optical fiber. **a** The single-mode optical fiber is first masked using narrow strips of polyimide tape. **b** The masked fiber is placed in an electron beam evaporator at a 45 degree angle so that the gold coats one side of the fiber along with the end face, before repeating the process after flipping the fiber. **c** Cross section of gated semiconductor heterostructure on an optical fiber. **d** Optical micrograph of sample after transfer. Although the gold pads are irregular and jagged, the sample area is uniformly clean. **e** Depiction of white light being transmitted through gated fiber sample. **f** Gate-dependent differential transmission spectrum of WSe_2.

Gaussian profiles and their field-dependent energies were recorded. The odd components of their energy shifts, corresponding to the Zeeman shift, are plotted in the figure 4.6.3 b and fit with a linear function to determine the g-factor. The g-factors of all four states are in close agreement with the previously determined g-factor of around -4, indicating that all four states have the same spin/valley configuration and have no additional magnetic moments from electron-hole spin-orbit coupling. Photon absorption by a p-wave exciton resonance is possible only if the photon carries orbital angular momentum, but since the light coupled through the

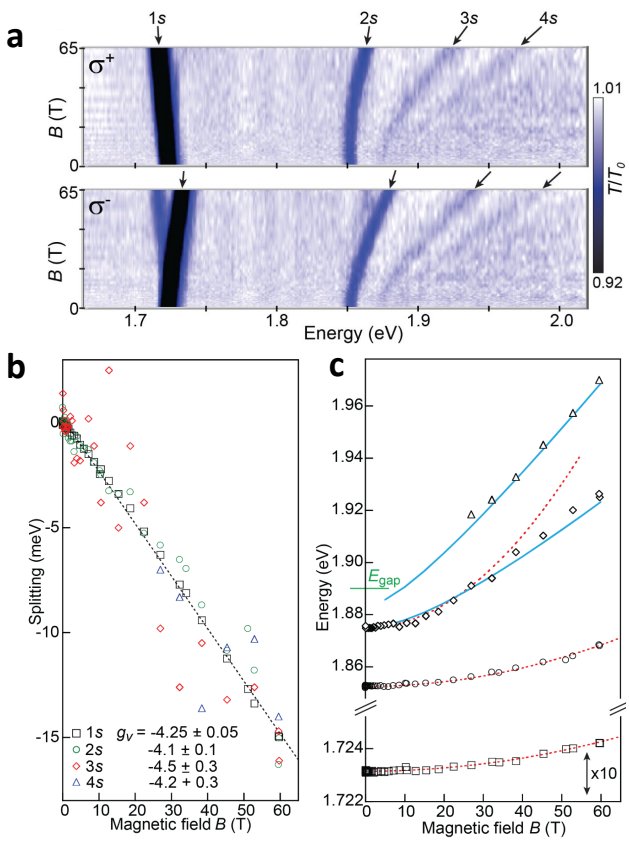

Figure 4.6.3 High field behavior of excited states. **a** Transmission spectrum colormap showing the evolution of the WSe_2 A_{1s}-A_{4s} exciton resonances from either valley up to 65 T. **b** The homogeneous zeeman splitting of the A_{ns} excitons. **c** Valley-averaged energy shifts of the A_{ns} excitons. Blue lines show numerically calculated diamagnetic shifts, red dashed lines show low-field quadratic fits. The band gap is shown in green.

fiber is necessarily in the fundamental $TEM_{0,0}$ mode, this possibility is precluded. It is also notable that such transitions are also dipole forbidden as they have net odd symmetry, thought they could be weakly brightened by electron-phonon coupling[146]. At an experiment temperature of 4 K, such absorption would be incredibly weak even for photons carrying the correct orbital angular momentum. This suggests that, if the observed resonances are indeed Rydberg-like excitations of the ground state exciton, they must be the optically allowed s-wave states.

Our tentative assignment is confirmed by the low-field diamagnetic shifts, calculated by fitting the even component of the resonance energy shifts with quadratic functions *up to a certain field*. At high magnetic fields, both the 3s and the 4s state show significant deviation from the quadratic fit. The 4s state, excluded from this analysis entirely, is not resolvable at low field, but the 3s state is resolvable and its diamagnetic shift is well described up to around 30 T by the quadratic fit. The radii of the 1s, 2s, and 3s excitons, according to their quadratic diamagnetic shifts, are $1.7 \pm 0.1\ nm$, $6.6 \pm 0.2\ nm$, and $14.3 \pm 1.5\ nm$ respectively, assuming an exciton reduced mass of $m_r = 0.20\ m_e$. To compare these results with theoretical expectations, ground state and excited state wavefunctions (fig. 4.6.4 a) were calculated using the Keldysh potential and the 2D hydrogenic potential, the results of which are tabulated in figure 4.6.4 b. Required material parameters for the calculations are

the 2D screening length $r_0 = 4.5\,nm$ of the WSe_2 monolayer[117] and the average dielectric constant of the encapsulating hBN layers[135], $\kappa = 4.5$. The values of these constants used in the numerical calculations described here are taken from literature and are consistent with the values used in section 4.5. The calculated energies of the states, as shown in figure 4.6.4 c, vary as a function of κ, and match well with the observed energies only at $\kappa = 4.5$, confirming the accuracy of the assumed material properties and the validity of the Keldysh potential. This is supported further by comparing the measured exciton size to the sizes predicted by the Keldysh and 2D hydrogenic potentials. The 2D hydrogenic potential substantially overestimates exciton size, a clear result of overestimating the screening as compared to the Keldysh model in the case of large electron-hole separation and a relatively weak surrounding dielectric environment.

The transition of the diamagnetic shift of the 3s and 4s states from quadratic in B to linear in B at high fields, along with the trend of increasing oscillator strength of the excited states with increasing magnetic field, are well explained as consequences of Landau diamagnetism. As discussed in section 4.2, there are two diamagnetic effects which are universal to gapped electronic systems: Quadratic closed-shell diamagnetism, which is quadratic in B, and Landau diamagnetism, which is linear in B. The derivation of the former is a straightforward result of 2nd order perturbation theory for an electron-hole system with a generic attractive central potential, while Landau diamagnetism is exact in the case of a free Fermi gas. But the inclusion of both of these effects along with the electrostatic potential means that they must both be treated perturbatively. Since it only applies to bound states, it must be the case that the quadratic diamagnetic effect leaves the single-particle gap unchanged and thus must act only on the quasiparticle gap, in effect borrowing some of the binding energy for the oscillator energy. Thus, as the magnetic field strength increases, the electron and hole become less tightly bound until, at some point, they are effectively unbound. This occurs when the diamagnetic shift is equal to the zero-field binding energy, or equivalently when the magnetic length $l_B = \sqrt{\hbar/eB}$ is equal to the exciton radius. Once the electron and hole are unbound, closed-shell diamagnetism is no longer valid. In reality, the Coulomb interaction acts over arbitrarily large distances, so the disappearance of Landau diamagnetism and the crossover from the bound state to the unbound state must happen asymptotically. As this occurs, the Landau quantization of the single-particle

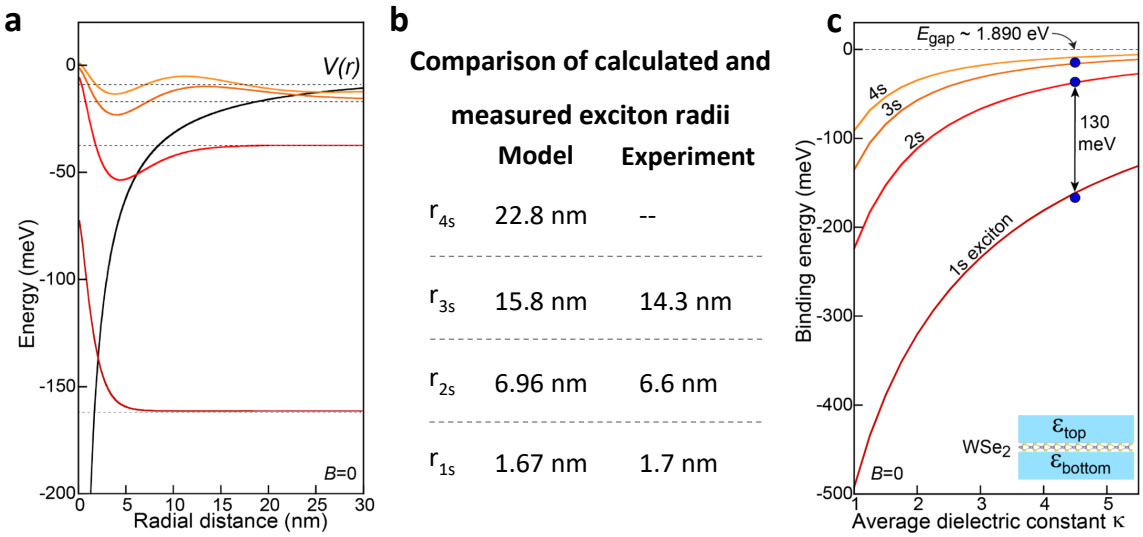

Figure 4.6.4 Comparison of measured and calculated exciton properties. **a** The calculated wavefunctions of the A_{ns} states superimposed over the confining Keldysh potential at B = 0. **b** Table comparing the exciton radii of their calculated wavefunctions to the experimentally determined values. **c** The influence of dielectric screening on exciton binding energy is compared to the actual binding energies determined from measured exciton energies. Only at the correct average dielectric constant is the correct 1s-2s splitting possible.

gap begins to dominate the spectrum of the exciton. We can also think of the onset of Landau diamagnetism in the high-field limit as resulting from the intrusion of cyclotron orbits into the orbitals of the bound state. Since l_B gives the radius of the 1st cyclotron orbit, as B increases, the cyclotron orbits shrink. Once the cyclotron orbit is of the same size as the exciton radius, the cyclotron orbits become a useful description of the bound state orbitals, i.e. $\langle\varphi_n|\psi_n\rangle$ becomes large, where $|\phi_n\rangle$ is the nth cyclotron wavefunction and $|\psi_n\rangle$ is the bound state orbital with principal quantum number n. It then stands to reason that this should occur when the cyclotron energy of the nth cyclotron orbital is equal to the binding energy of the ns exciton[119].

Of course, the exact solution to the Hamiltonian with Coulomb and magnetic field interactions would produce something that might as well be called the *excitonic diamagnetic shift*, which produces limiting behavior at low and high field which mirrors the two more famous effects, but crucially carries a single good orbital quantization number across all magnetic fields, including the intermediate field regime where neither limit applies. In other words, this quantum number should be conserved across the transition from Langevin-like behavior to Landau-like behavior. In turn, as we seek to describe our observations of quantized energy levels transitioning

between these two regimes, we can describe any given energy level *n* as having the properties of the *ns* closed orbital at low field and the properties of the Nth Landau level (where $N = n - 1$) at high magnetic field. This understanding is necessary in order to determine the critical field at which the crossover between low and high magnetic field regimes occurs, as we must be able to compare the energy of the Nth cyclotron level to the binding energy of the ns exciton. Based on the calculations summarized in figure 4.6.4 c and experimentally determined electron and hole reduced masses, we can deduce the binding energy of the 1s-4s states and calculate their critical fields to be 580 T, 41 T, 11 T, and 3.5 T, respectively. Since this critical field reflects the *crossover* point rather than the transition into one regime or the other, it is most aptly described as representing the intermediate field regime in which neither limiting behavior is applicable. Rather, Langevin diamagnetism applies when the magnetic field is much smaller than the crossover field, and Landau diamagnetism applies when the magnetic field is much larger than the crossover field. This suggests that, even for the 3s and 4s states, whose diamagnetic shifts appear to be nearly linear, the highest achievable field is still in the intermediate field regime. If one were able to measure the diamagnetic shift in the high field regime, the exciton's reduced mass could be calculated very precisely based on the cyclotron energy (which is inversely proportional to the reduced mass). But since for the observed states the high field regime is not reached, this simple calculation is not possible.

However, it is possible to use the information from the 3s and 4s states to put *bounds* on the reduced mass. Given the net diamagnetic shift of the exciton

$$\Delta_N(B) = \frac{\hbar\left(N + \frac{1}{2}\right)eB}{m_r},$$

the derivative of which is

$$\frac{d\Delta_N}{dB} = \frac{\hbar\left(N + \frac{1}{2}\right)e}{m_r},$$

and knowing that the slope of the measured diamagnetic shift should increase monotonically and asymptotically towards this value, we can deduce a *lower bound* on the ultimate slope. Therefore, based on the slope of the diamagnetic shift at the highest magnetic fields for the 4s

state, we can calculate an *upper bound* on the reduced mass of $m_r < 0.21\ m_e$. At the same time, the ratio of the splitting between the Nth and (N-1)th energy levels δ_N to the cyclotron energy should monotonically and asymptotically approach unity from above. We can thus use their splitting at the highest magnetic field to place a *lower bound* on the reduced mass of $m_r < 0.19\ m_e$. Because the upper bound is determined solely by the diamagnetic shift of the 4s state which is close to the high-field regime, while the lower bound relies partly on the diamagnetic shift of the 3s state, we can expect the upper bound to be a tighter and more accurate constraint than the lower bound. This result represents the first time that the reduced mass of the exciton in a 2D semiconductor has been directly constrained experimentally.

Another elegant result from this data arises from the consistency of the measured g-factor for the 1s-4s states (fig. 4.6.3 b), along with the discovery of very large, spatially diffuse wavefunctions for the excited states. In particular, it gives us insight into the distribution of orbital and valley magnetic moments (see section 3.3) throughout the Brillouin zone. Since the overall g-factor involves the contributions of all Bloch waves contained within the wave packet and both orbital and Berry curvature derived magnetic moments can be expected to change across the Brillouin zone, it might also be expected that the g-factor could deviate from the K point value due to the wave packet's finite size. This is especially true of the 1s exciton which has a radius of around 1.7 nm, roughly 2.5 times the size of the lattice constant, and therefore the 1s exciton's wavefunction fills a substantial portion of the Brillouin zone and potentially samples a varied distribution of magnetic moments. On the other hand, the 4s exciton, whose radius is approximately 23 nm from calculations, samples only a minute section of the Brillouin zone in the vicinity of K. Given the constant g-factor across excitons spanning over an order of magnitude in size, we conclude that the distribution of magnetic moments in the Brillouin zone is fairly homogeneous around K, at least when an azimuthal averaged (i.e. averaging along the band edge at a constant momentum difference *q* away from the band edge minimum).

5 - Engineering interlayer interactions in semiconducting heterobilayers

In this chapter, we discuss the properties of heterobilayers semiconducting transition metal dichalcogenides (TMDCs), composed of two monolayers of different TMDCs placed into contact with each other. Their staggered band alignment allows for the formation of interlayer excitons. We discuss seminal studies of these interlayer excitons, and present a new method for controlling their behavior and enhancing their beneficial properties by separating the TMDC layers with a thin tunneling barrier.

5.1 Heterobilayers of transition metal dichalcogenides: a coupled quantum well analogue

In chapters 3 and 4, we introduced the semiconducting transition metal dichalcogenides (TMDCs), whose unique locked spin-valley physics and direct band gap make them an attractive platform for studying spintronics and excitonic physics in the ultimate limit of 1D quantum confinement in monolayer form. It was often helpful in these chapters to draw comparisons to foundational works in quasi-2D semiconductor systems such as GaAs (and other III-V) quantum wells (QWs), after which many studies of TMDCs have been modeled, such as the measurement of the diamagnetic shift of excitons presented in chapter 4. Given that III-V QWs have a 3-decade head start, it's not too surprising that, given their relative novelty, new fundamental discoveries in TMDCs continue to be made at a rapid pace. Only in the last year was the full excitonic spectrum of WSe_2 fully described, with its 15+ photoluminescence (PL) emission lines now fully identified[86].

One of the most exciting offshoots from the study of quasi-2D QWs is the coupling of two or more QWs layered together to form *double* or *coupled quantum wells* (CQWs)[147–150]. The typical III-V CQW structure centers on an epitaxially grown five layer stack, with each layer composed of $Al_{1-x}Ga_xAs$ with varying composition parameter x (fig. 5.1.1 a). The band gap of $Al_{1-x}Ga_xAs$ decreases monotonically with increasing composition parameter x, and the band alignment between two QWs with different x is type-I, i.e. the conduction and valence bands of

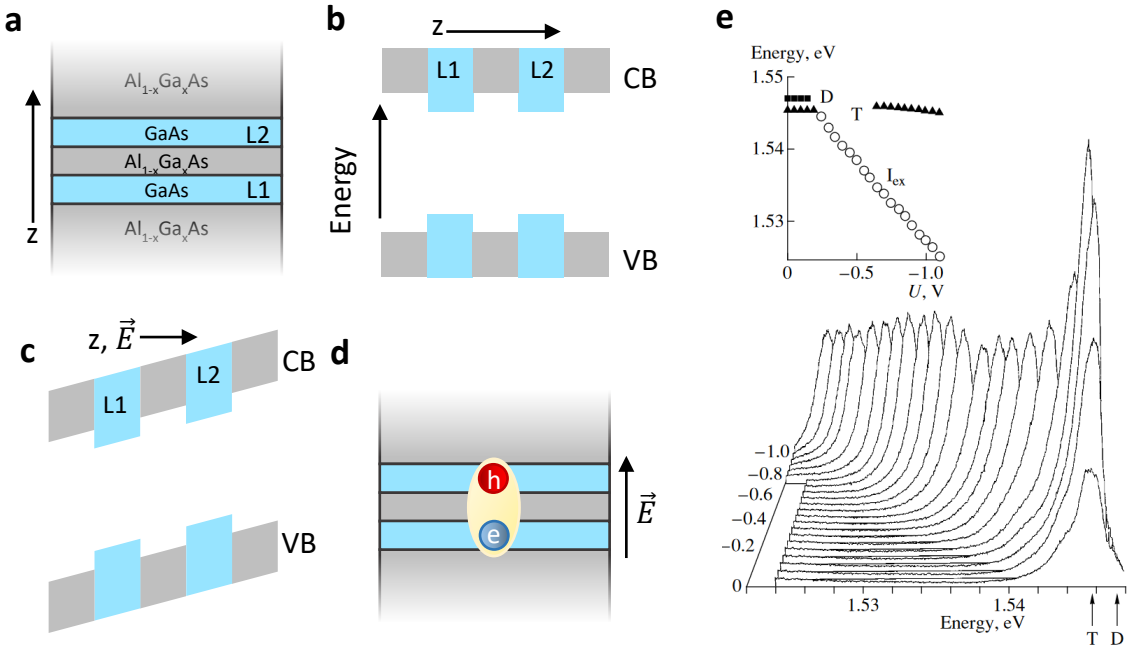

Figure 5.1.1 Indirect excitons in coupled quantum wells**. a** Diagram of an AlGaAs/GaAs coupled quantum well with the two quantum wells labeled L1 and L2. **b,c** Band schematic of the coupled quantum well without and with an electric field applied in the perpendicular direction. **d** Cartoon of an indirect exciton in the biased coupled quantum well. **e** Dependence of the coupled quantum well photoluminescence on interwell bias U. T and D denote the two intrawell exciton species, and I_{ex} is the interwell species.

the QW with the smaller band gap fall entirely within the gap of the QW with the larger band gap. This means that, in effect, the QW with lower x (and larger band gap) acts as an insulator for carriers in the QW with higher x. The second and fourth layers in the CQW are the active layers and are thin, high-x QWs, if not pure GaAs. The layer between them (layer 3) has a lower x than the active layers, and thus acts as an insulating/tunneling barrier. The first and fifth layers are low-x $Al_{1-x}Ga_xAs$ (if not pure AlAs) and act as dielectric substrates for epitaxial growth and potentially lithographic patterning of a conductive gate layer. The low-energy band structure of a symmetric CQW is depicted schematically in figure 5.1.1 b. Since the two QW layers are degenerate in this design, carrier tunneling between them is essentially determined by quantum fluctuations, and the tunneling probability can be tuned by the thickness or band gap of the barrier layer (the difference in gap between the QWs and barrier layer sets the tunneling potential barrier height). If an electrostatic bias between the two QWs is introduced, either using electrodes directly in contact with the two QWs or by the application of a perpendicular electric

field, the overall layered band structure becomes tilted (fig. 5.1.1 c), and the CQWs acquire staggered (type-II) band alignment[148,150]. Ground state electrons will then preferentially tunnel to the layer with the lower valence band, and holes to the layer with the higher conduction band. Under optical excitation, biased CQWs host *spatially indirect* excitons, in which the electron resides in layer with lower conduction band and the hole resides in the layer with the higher valence band, giving them an out-of-plane electric dipole moment (not to be confused with the optical dipole moment) (fig. 5.1.1 d). The optical transition for the indirect excitons remains *momentum* direct[151] though—a terminological distinction that may befuddle those outside the CQW community. As the interlayer bias increases, the conduction band hosting the electron decreases in energy and the valence band hosting the hole increases in energy, resulting in a net decrease in the energy of the indirect exciton transition (fig. 5.1.1 e). Of course, in the case of zero interlayer bias, the indirect exciton transition becomes degenerate with the direct transition[151,152]. With a large enough interlayer bias, the conduction or valence bands of the QWs become degenerate with the bands of the barrier layer, which will then stop acting as an insulator and will then proceed to form type-II alignment with both of the QW layers. This is especially a concern if the composition parameter x is similar for the QWs and the barrier layer, and thus the difference in their bandgaps is small to begin with.

The indirect excitons in CQWs have been of great interest to the scientific community for a number of reasons. First, they have a relatively long lifetime thanks to the large electron-hole separation, which suppresses recombination[153]. Second, the reduced e-h Coulomb interaction increases their Bohr radius, exaggerating the effects of the vertical quantum confinement[154]. Third, since their energy is broadly tunable by an external electric field, it is straightforward to create customized lateral potential traps and landscapes for them through lithographic patterning of gate electrodes[151]. Lastly, their permanent electrostatic dipole moment leads to strong many-body interactions. This combination of factors opens the door to studying many-body physics and potentially forming correlated states. There have been numerous reports of electrostatically-trapped indirect excitons forming exciton condensates at high density and low temperature, and the formation of spatio-temporal coherence in indirect exciton gasses[155]. There is also potential to form electrostatically defined indirect exciton superlattices, analogous to

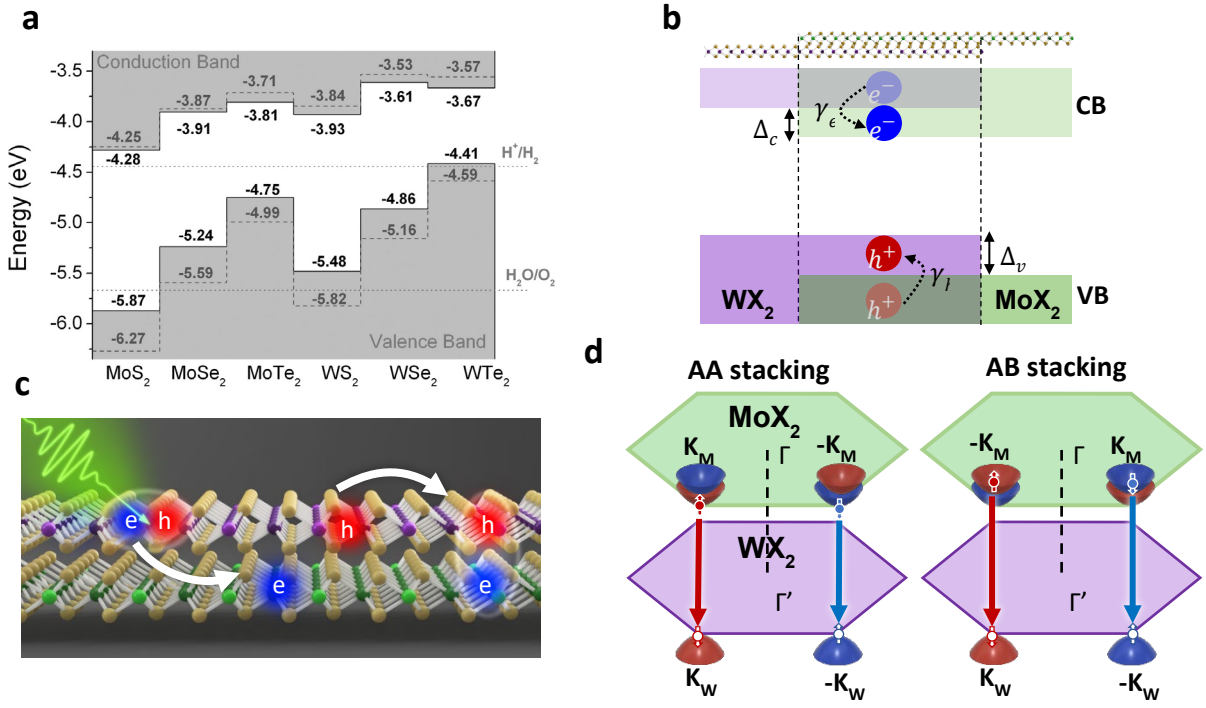

Figure 5.1.2 Interlayer excitons in heterobilayers of transition metal dichalcogenides. **a** Band offsets of the six gapped transition metal dichalcogenides. All sulfide and selenide members of the family exhibit type-II band alignment with each other. **b** The band offsets in the conduction (valence) band Δ_c (Δ_v) drive electron (hole) transfer to the energetically favorable layer with transition rate γ_e (γ_h). **c** Cartoon depiction of interlayer exciton formation. First, a photon generates a photoexcited electron/hole pair. Then, on a timescale similar to the time required for the intralayer exciton to form, the electron or hole relaxes to the opposite layer. Finally, the electron and hole become bound to form an interlayer exciton. **d** Depiction of the K-point band structure of a heterobilayer in the case of AA or AB stacking, showing the different possible ground state spin/valley configurations in the two cases.

optical lattices, for studying Hubbard model physics and other many-body interactions on a synthetic lattice[156–158].

In close analogy to the III-V semiconductor CQWs, it is also possible to form coupled bilayers of 2D TMDCs, by stacking two layers of a given TMDC together with a barrier layer, then applying an interlayer bias[159]. However, a unique property of the TMDC family allows us to simplify the construction of coupled bilayers, namely that any two *different* members of the semiconducting TMDCs, when stacked together, naturally form type-II band alignment[65] without any external interlayer bias (fig. 5.1.2 a), while the van der Waals gap between them serves as a tunneling barrier. Since all four semiconducting TMDCs have different energy gaps, the interlayer

potential difference between the upper valence and lower conduction bands will be different. Depending on the pairing of TMDCs, the effective interlayer potential for either the valence or conduction band can be anywhere from about 200 to 1000 meV. Upon optical excitation, the excited electron and hole then have a chance to hop to the layer with the lowest potential for the given carrier. The large interlayer potential driving the charge transfer ensures that the process is ultrafast and occurs on the time scale of 10s to 100s of fs (fig. 5.1.2 b)[160]. Given the radiative lifetimes of the excitons in TMDCs, typically several ps[161], this means that virtually all intralayer excitons (X_A) that form are swiftly dismantled before they have a chance to recombine, quenching their PL. Like the indirect excitons in CQWs, the Coulomb interaction for electrons and holes in opposite layers remains strong enough for form excitons from an electron in one layer and a hole in the other (fig. 5.1.2 c)[20]. These are typically referred to as *interlayer excitons*, or IX (perhaps to the consternation of the reader, the same abbreviation is used for indirect excitons, but in this dissertation, IX will refer exclusively to interlayer excitons in van der Waals layered structures).

The electronic transition for indirect excitons in III-V semiconductor CQWs, like the transitions within a single QW, are momentum direct[152]. Absent band hybridization effects which can potentially change the location of the conduction or valence band extrema, this is necessarily the case because the band extrema are both located at the Γ point at the zone center[162]. Even if the band extrema were at non-zero crystallographic momentum, the layered assembly of CQWs is accomplished through epitaxial growth, and consequently, adjacent layers are crystallographically aligned with one-another. On the other hand, the band extrema in TMDCs are located at the K point, the corner of the hexagonal Brillouin zone, and because the two layers constituting a heterobilayer are only held together by van der Waals forces, it is possible for them to be rotationally misaligned. If they are misaligned, then the K point in one layer may not overlap the K point in the opposite layer, resulting in an interlayer electronic transition that is momentum indirect. However, using the van der Waals transfer technique outlined in section 2.3 and the polarization-resolved second harmonic generation (SHG) method for determining crystal axes of non-centrosymmetric crystals (such as TMDC monolayers) outlined in section 2.4, it is possible to build TMDC heterobilayers in which are rotationally aligned. In this case, the K point

in one layer can be intentionally aligned with the K point or even the $-K$ point in the opposite layer (fig. 5.1.2 d), with the implementation of phase-resolved SHG. When the layers are crystallographically aligned, the interlayer transition is nearly momentum direct, although a slight radial misalignment is inevitable, due to the different lattice constants of the various TMDCs.

Given the small size of excitons in TMDCs (explored in chapter 4), their wavefunction fills a large enough portion of the Brillouin zone for recombination to be relatively efficient despite the radial misalignment, or even with slight angular misalignment[163], although notably, interlayer exciton PL will generally be absent in grossly misaligned heterobilayers. As a result, PL from the IX can be observed, with the emission energy being much lower than the intralayer PL, due to the large band offsets (fig. 5.1.3 a)[20]. Although it is substantially quenched compared to freestanding monolayers, PL from intralayer excitons can be seen in heterobilayers. Due to hybridization and band bending, the emission energies of the intralayer excitons are slightly different from the freestanding monolayers[164,165]. Emission from the charged trion species is prevalent as a result of charge accumulation in either layer due to the built-in interlayer potential. The IX PL is substantially inhomogeneously broadened compared to the intralayer exciton PL. Because of its large out-of-plane permanent electrostatic dipole moment, the IX produces an extended electric field and is very sensitive to contamination between layers and inhomogeneity in its dielectric environment (fig. 5.1.3 b)[20,21,166]. Furthermore, the electrostatic dipole moment of the IX causes strong dipolar repulsion between IX, resulting in a density-dependent energy shift of the IX (fig. 5.1.3 c)[166]. An inhomogeneous distribution of IX density would therefore contribute to the inhomogeneous broadening of the PL emission spectrum.

Because the carrier wavefunctions at the valence and conduction band edges are highly localized to the transition metal orbitals at the very center of each TMDC layer, the electron and hole wavefunctions of an IX have essentially no overlap. As with CQWs, this suppresses recombination and endows IX with an extremely long lifetime, on the order of 10s to 100s of ns[71,167,168], up to 5 orders of magnitude longer than the lifetimes of the intralayer species (fig. 5.1.3 d). The reduced Coulomb interaction also suppresses electron-hole exchange interactions, the primary mechanism for Valley depolarization, thus extending the valley lifetime of IX out to 100s of ns or even μs[166,169]. If a heterobilayer is excited with a focused spot of pulsed light,

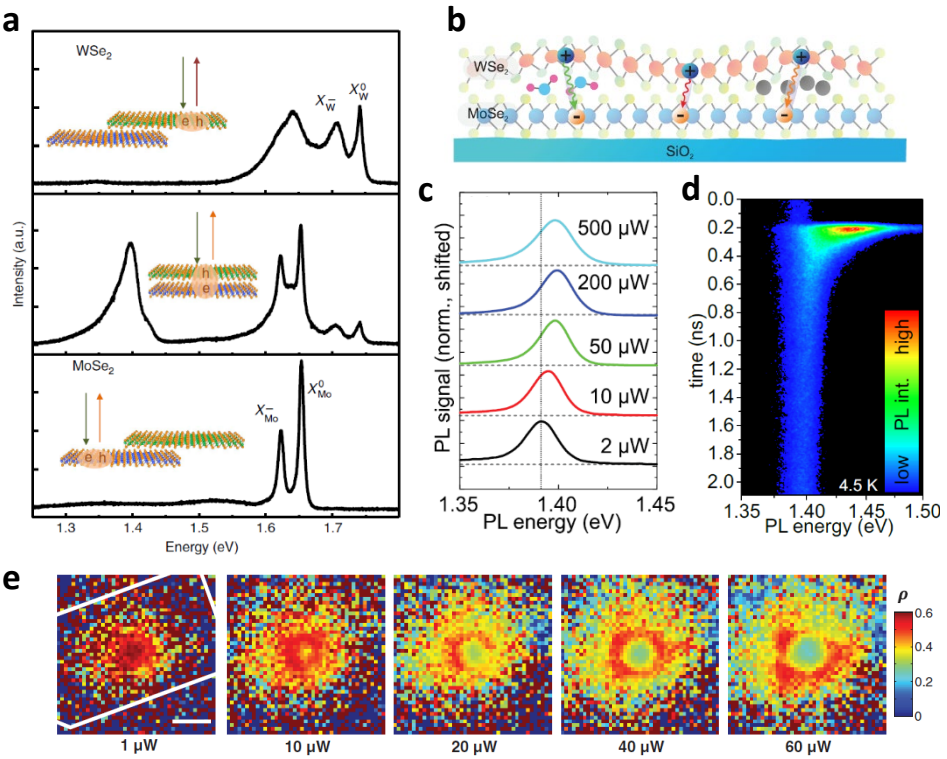

Figure 5.1.3 Interlayer exciton photoluminescence. **a** PL spectra of monolayers of WSe_2 and $MoSe_2$ and a heterobilayer formed from monolayers of each. Emission from the intralayer species in either monolayer can be seen in the heterobilayer, along with a new dominant peak which corresponds to the interlayer exciton. **b** Cartoon showing the effects of interfacial contamination and disorder on the interlayer exciton energy distribution. **c** Excitation density dependent blueshift of interlayer excitons resulting from dipolar many-body interactions. **d** Time-resolved spectral dynamics of interlayer excitons. At 0.2 ns, the heterobilayer is excited by pulsed light, creating a dense, strongly interacting exciton gas. As the excitons diffuse and recombine to lower the density, their spectrum redshifts as a result of reduced many-body interactions. **e** Spatially-resolved interlayer exciton valley polarization provides evidence for valley-dependent exchange interactions. At high excitation density, the majority valley experiences stronger repulsive interactions than the minority valley, and preferential diffusion creates a ring of high valley polarization.

forming a localized, momentarily high density cloud of IX, the long decay dynamics and strong repulsive many-body interactions cause the IX cloud to expand superdiffusively. The time-varying population density therefore results in a time-dependent energy spectrum, with the initial high density producing a blueshifted spectrum which decays and redshifts over time (fig. 5.1.3 e), and decay dynamics that deviate significantly from simple exponential decay. Moreover, the IX are subject to valley-dependent repulsive exchange interactions, meaning that in a valley-

polarized cloud of IX, the majority valley type will expand more rapidly than the minority valley type, leading to interesting valley texture (fig. 5.1.3 e)[166].

5.2 Controlling interlayer exciton dynamics with a tunneling barrier

In CQWs, a tunneling barrier between the QWs is necessary to form discretized energy levels and increase the size of their band offset in order to form indirect excitons. While this is not necessary in TMDC heterobilayers to form IXs thanks to their naturally-occuring type-II band alignment, a tunneling barrier can be used to tune the properties of the IX. A similar mode of control is used in CQWs, by tuning the thickness and composition of the barrier layer[170,171]. A natural candidate for a tunneling barrier in a van der Waals heterostructure is hexagonal boron nitride (hBN), a wide-gap insulator which is optically transparent. To study the impact of a tunneling barrier on the IX in TMDC HBLs, we have built a series of devices consisting of monolayers of WSe_2 and $MoSe_2$ separated by a thin hBN spacer layer with variable thickness, allowing for systematic study of the effect of different spacer thicknesses on IX while controlling for variations between samples (fig. 5.2.1 a), including twist angle and crystal composition. The WSe_2-hBN-$MoSe_2$ structure is encapsulated on either side by thick layers of hBN (10-30 nm) to provide a homogeneous, pristine crystalline substrate. We refer to the resulting structure as a forked heterobilayer, or FHBL. A micrograph of an assembled FHBL is shown in figure 5.2.1 b, and this specific sample is referred to as FHBL-6, and has regions with no separation, monolayer hBN separation, and 2 nm thick hBN separation (6 to 7 layers), and an interlayer twist angle of around 4 degrees. Unless otherwise noted, data presented below were collected at a sample temperature of 5 K using a pulsed laser (pulse duration 6 ps) to excite the sample. Spectra were acquired using a spectrometer equipped with a CCD array.

We begin by studying the intralayer exciton PL of FHBL-6. In these studies, the non-resonant excitation wavelength used was 633 nm. Figure 5.2.1 c shows the typical PL spectra of the freestanding monolayers and the PL spectra of the three HBL regions, in the energy region corresponding to the WSe_2 and $MoSe_2$ intralayer exciton species. As expected, intralayer exciton PL from both layers is visible in the directly contacted HBL, although significantly quenched and

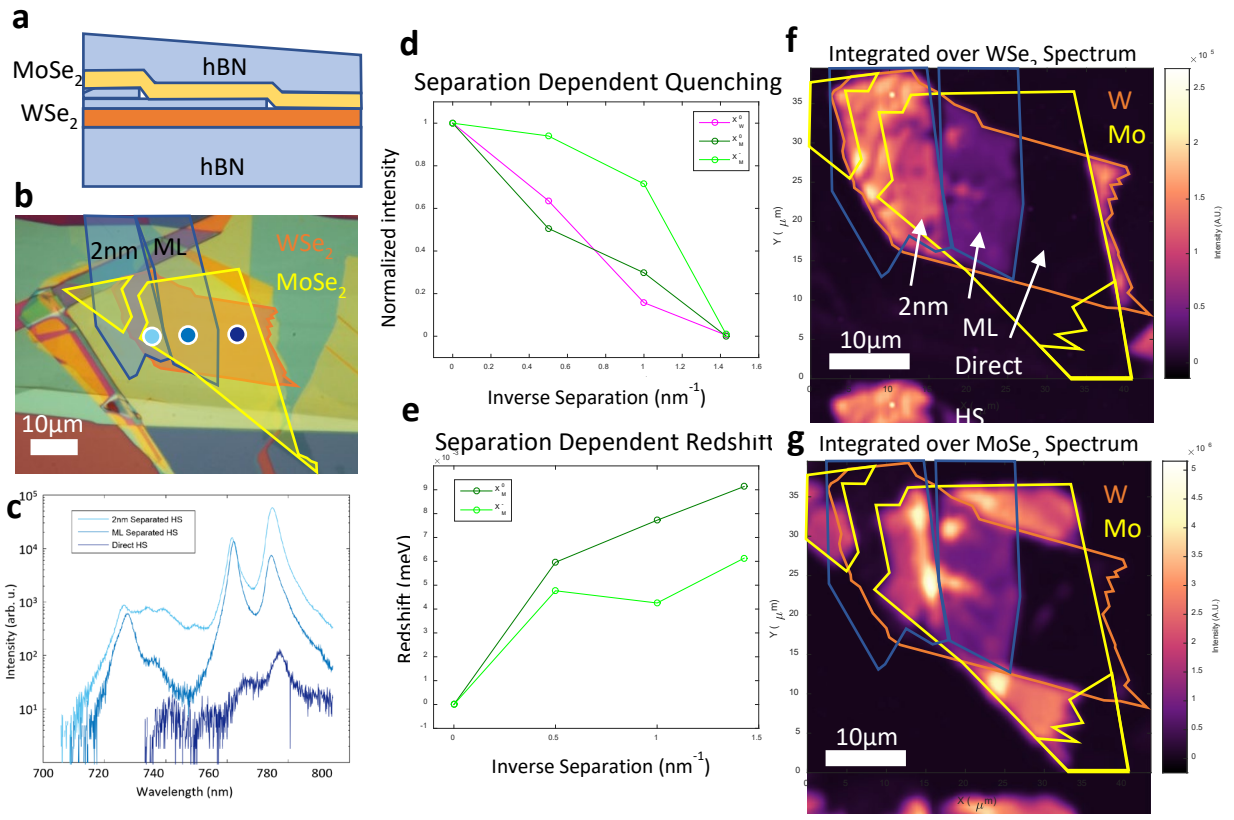

Figure 5.2.1 Boron nitride spaced heterobilayers. **a** Cross-section of a forked heterobilayer (FHBL) with an hBN spacer of varying thickness. **b** Optical micrograph of a FHBL with monolayer (ML) and 2 nm thick hBN spacers. Overlaid shape represent the outlines of important layers. **c** PL spectra from select spots in each region of the FHBL. Color-coded dots in fig. c represent the locations at which the spectra were taken. **d-e** Intensity change and redshift of various intralayer exciton species (X_j^s is the intralayer exciton in layer j with charge s) as a function of inverse layer separation. Freestanding layers are taken to have inverse separation of 0 nm^{-1} as they are uncoupled. Both are measured relative to the freestanding layers. **f-g** Spatially resolved PL maps integrated over the spectral regions corresponding to the intralayer excitons in either layer, showing the effects of quenching and homogeneity of the sample.

hybridized compared to the freestanding monolayers. In the regions with hBN separator, the degree of quenching and hybridization are reduced due to suppressed interlayer interactions and charge transfer through the tunneling barrier (fig. 5.2.1 d-e). When the PL intensity in spectral bands corresponding to the WSe_2 and $MoSe_2$ is mapped out spatially, the effect of the spacing layer can be seen even more clearly (fig. 5.2.1 f-g), with the regions of different separation clearly distinguished from one another. While the intensity distribution is fairly homogeneous across a

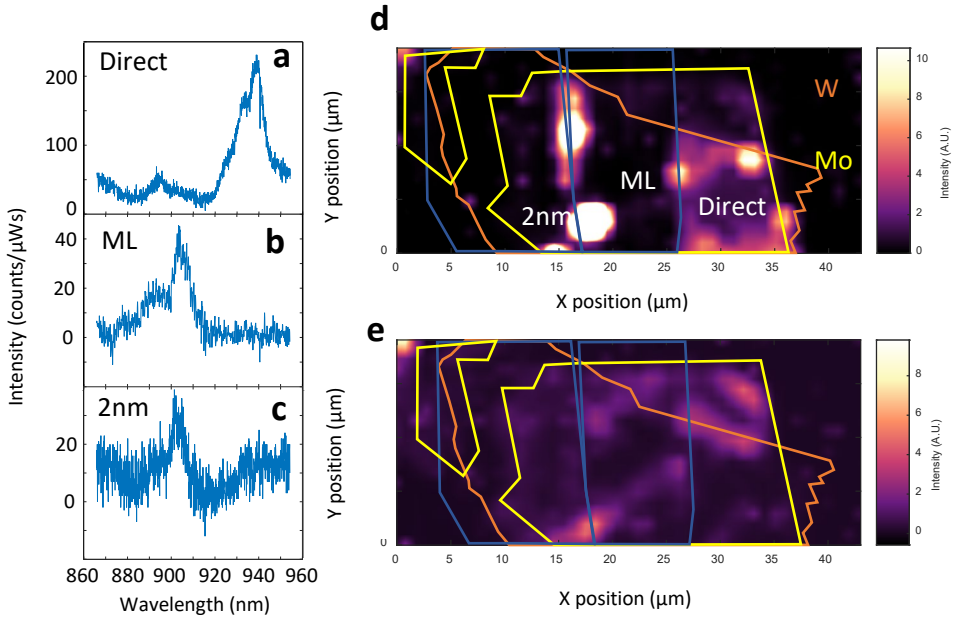

Figure 5.2.2 Interlayer excitons in a spaced heterobilayer. **a-c** Characteristic photoluminescence spectra from the three different separation regions of FHBL 6 normalized to excitation power and integration time. **d-e** Spectrally integrated PL maps of FHBL 6 across the spectral regions of 910-950 nm and 880-900 nm, respectively, showing the localization of the lowest energy peak to the directly contacted portion of the FHBL.

given region, there are hot-spots corresponding to bubbles of contaminants between layers in the stack (not necessarily between the TMDC layers, possibly at other interfaces).

The PL from the IX of FHBL-6 is somewhat less homogeneous than the intralayer exciton PL, highlighting the sensitivity of the IX to disorder. Select spectra from each region are shown in figure 5.2.2 a-c. The PL in the separated regions is notably weaker and less regularly structured than the PL in the directly contacted HBL, and generally occurs at higher energies. In fact, when a select spectral band (910-954 nm) is integrated and spatially mapped, we can see that PL of this energy range is largely localized to the unseparated region (fig. 5.2.2 d). Examining the spectral region of 880-900 nm, the distribution across the HBL is anything but consistent, showing up at specific hot spots and even on the $MoSe_2$ monolayer (in the case of the monolayer, the contribution to this energy band is from the exponential defect tail of the $MoSe_2$ and is distinct from the spectra of the HBL) (fig. 5.2.2 e).

A separate sample, FHBL-4 (fig. 5.2.3 a), had better crystallographic alignment between layers (< 2 degrees) and produced substantially brighter interlayer photoluminescence, enabling more careful study of the interlayer excitons in the separated regions. This sample had regions of hBN barrier thickness of zero, one, and two layers. As with FHBL-6, the intensity of the intralayer PL correlated positively with spacer thickness (see appendix C: supplementary data for chapter 5). Substantial differences between the IX PL in the different regions of separation were also observed, and the PL was relatively homogeneous across each region (fig. 5.2.3 b). A line cut showing the evolution of the IX PL spectrum through the different regions is shown in figure 5.2.3 c. Each region is clearly identifiable by a unique energy spectrum, with the lowest and broadest energy spectrum appearing in the unseparated region and the highest and narrowest spectrum appearing in the bilayer separated region. The increasing energy with separation is expected from the accompanying reduction in binding energy, however the narrowing of the spectrum remains unexplained.

Another expected result from separating the electron and hole and inserting a tunneling barrier between them is increased exciton lifetime. To study the interlayer exciton dynamics, we excite the sample with a pulsed laser at 2 MHz with a pulse duration of 6 ps, resonant with the WSe_2 trion at 735 nm. The photoluminescence is sent through a monochromator and into an avalanche photodiode (APD) connected to a time-correlated single photon counting module, which builds up a histogram of PL photon arrival time to the APD following triggering by the pulsed laser's timing output. This setup allows us to build up the energy-dependent PL dynamics and distinguish the different PL features from each other. The normalized PL decay traces for the directly contacted heterostructure and the monolayer-separated HBL are presented in figure 5.2.3 d. While the PL from the separated HBL initially (for the first 50 ns) decays rapidly compared to the directly contacted HBL, the decay slows down substantially and the intensity beyond 100 ns appears to be virtually constant in time over the 500 ns decay trace shown here, indicating a slow decay component with a lifetime much longer than 500 ns. To extend the histogram collection window and reduce signal wraparound, the repetition rate was reduced further to 200 kHz. This enabled the collection of data out to 5 μs of delay. Once again, the extremely long lifetime component of the interlayer exciton in the separated region is clear, and with the

extended data collection time, reaches an eventual single exponential decay with a lifetime of 8.5 μs, as many as 7 orders of magnitude longer than the intralayer PL lifetime (fig. 5.2.3 e). When we excite the sample with circularly polarized light and measure the decay dynamics of the co- and cross-circularly polarized components, we can calculate the time-dependent valley polarization ρ (fig. 5.2.3 f). Calculating the lifetime based on the individual lifetimes of the circularly polarized components, we find the co-polarized emission has a PL lifetime of 8.4 μs and the cross-polarized emission has a PL lifetime of 9.2 μs, yielding a PL polarization lifetime of up to 40 μs.

Since the discovery of bright PL in monolayer TMDCs and the locked spin-valley physics, scientists have proposed numerous applications for quantum devices based on exciton valleytronics. However, the fast dynamics of excitons in monolayer TMDCs, and even the interlayer excitons in heterobilayers, make the useful manipulation of TMDC valley excitons for technological applications rather difficult. Here, we have demonstrated a straightforward way to extend the exciton and valley lifetimes in TMDC heterobilayers by up to 7 orders of magnitude by inserting a tunneling barrier between layers, bringing this material system closer to technological utility. The extension of the lifetimes and quantum control afforded by this method also has value in basic science—the long PL lifetime and single-exponential decay suggest a stationary, cool population of excitons, a necessary requirement for realizing coherent and many-body phases which are fragile at high electronic temperatures. The increased dipole moment due to electron-hole separation enhances the dipolar repulsion of the IX and increases the coupling strength of the IX to an external electric field, making possible deep electrostatic potential traps which can confine dense populations of long-lived, strongly interacting IX.

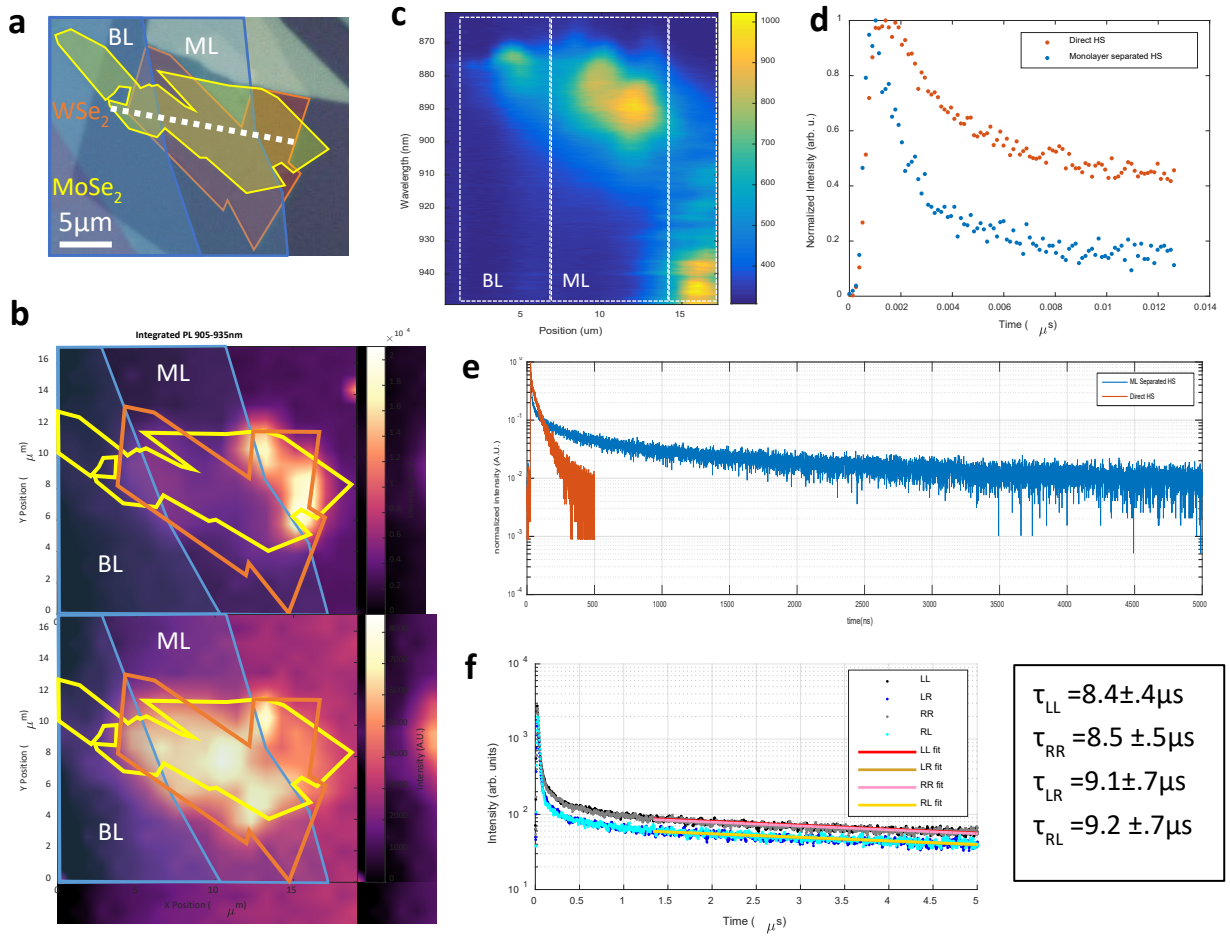

Figure 5.2.3 Excitons dynamics in a spaced heterobilayer. **a** Schematic of FHBL 4, with monolayer (ML) and bilayer (BL) hBN separators. **b** Spatially resolved photoluminescence integrated over the 905-935 nm (top) and 880-900 nm (bottom) spectral regions, respectively. **c** Spatial photoluminescence linecut of sample. The excitation/collection spot is moved across the white dashed line in fig. a from left to right. Each separation region of the FHBL produces a distinct photoluminescence spectral distribution. **d-e** PL dynamics of the directly contacted and monolayer separated regions. **f** Polarization-resolved PL dynamics of the monolayer separated region with tails fit to single exponentials. Decay constants are tabulated on the right. The majority valley has a slightly shorter lifetime than the minority valley, yielding a calculated valley lifetime of 43 μs.

6 - Magnetism in atomically thin flakes of mixed-halide chromium trihalides

In this chapter, we introduce a prominent family of 2D magnetic materials, the chromium trihalides, and discuss their layered magnetic behavior down to the atomically thin limit. Two members of the family, CrI_3 and $CrBr_3$, both have out-of-plane anisotropy which stabilizes out-of-plane magnetism within a given layer, but unlike $CrBr_3$, antiferromagnetic interlayer coupling results in layered antiferromagnetic ordering in CrI_3. Since the interlayer magnetic interaction is controlled by superexchange between layers through the halide sites, we demonstrate the ability to tune the interlayer magnetic order from antiferromagnetic to ferromagnetic by forming solid solutions of CrI_3 and $CrBr_3$ of the form CrI_xBr_{3-x}. Curiously, these mixed-halide 2D magnets exhibit coexisting ferromagnetic and antiferromagnetic domains at critical compositions, which we speculate might arise from stacking faults.

6.1 Layered 2D magnetism in chromium trihalides

Layered magnetism arises in 2D and quasi-2D layered structures of magnetic materials in which the intra- and interlayer magnetic coupling result from different mechanisms or are independently tunable[172–174]. A classic example of this is in synthetic layered antiferromagnetic (SAF) thin films, where Ruderman-Kittel-Kasuya-Yosida[175–177] (RKKY) interactions between two ferromagnetic layers are mediated by a nonmagnetic spacer layer[178,179]. The spin component of an electron wavefunction as it passes through the nonmagnetic layer has a dynamic phase which depends on the thickness of the spacer and the magnetization of the two magnetic layers on either side. Careful epitaxial growth therefore allows for the net magnetic interaction between the layers to be ferromagnetic (FM) or antiferromagnetic (AFM), or even for the interlayer interaction to be turned off completely by designing the spacer thickness to produce a specific dynamic phase for spins transmitted between layers.

Perhaps the most ubiquitous example of interfacial engineering of layered magnetic structures is exchange biasing in hard disk drive read heads[180,181]. These devices are based on

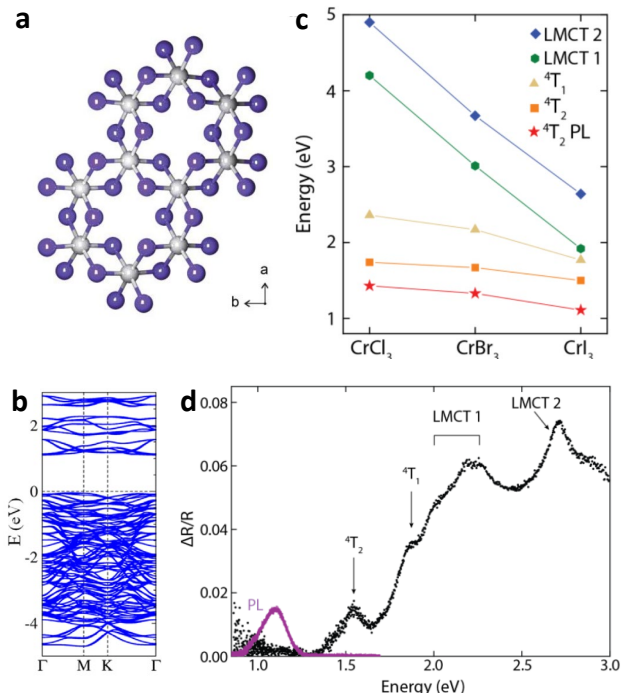

Figure 6.1.1 Properties of exfoliated CrI_3 . **a** The crystal structure of a single layer of a chromium trihalide viewed from the out-of-plane direction. **b** Band structure of CrI_3. **c** Energy dependence of the various crystal field levels of chromium trihalides for the various halogens. **d** Differential reflectance and PL spectra of CrI_3 at 4 K.

magnetoresistance (MR) effects (giant[178,179] or tunneling MR), in which the resistance between two FM layers is dependent on the relative orientation of their magnetization. The magnetization of one of the FM layers is pinned by placing it in contact with a type-A antiferromagnetic (A-AFM) material which is ferromagnetically ordered within the plane and antiferromagnetic ordered between planes. The magnetic field required to magnetize the A-AFM layer is large, making it insensitive to its magnetic environment and leaving the crystal plane which is in contact with the exchange-biased FM layer permanently magnetized. Electron exchange interactions between the A-AFM layer and the FM layer it is contacting produce an effective magnetic field in the FM layer[95,182,183] which shifts the center of its coercive loop, making it effectively insensitive to the magnetic environment produced by the magnetic domains of the hard drive platter in which information is stored. The second FM layer which is not exchange biased, however, can have its magnetic orientation flipped by proximity coupling to the magnetic field of the hard drive platter domains. Thus exposure of the MR junction to the magnetic data on the hard disk platter will only affect the magnetization in one of the two FM layers, providing control over the *relative* orientation of the magnetization of the FM layers, enabling data readout via the magnetic junction's magnetoresistance.

In both of the cases of SAFs and MR devices, their proper function of the device relies on precise epitaxial growth which, while readily achieved with modern equipment, remains expensive and slow[184]. Furthermore, the lattice-matching requirements for high-quality interfaces in layered epitaxial growth restricts material compatibility. Recent discoveries of 2D

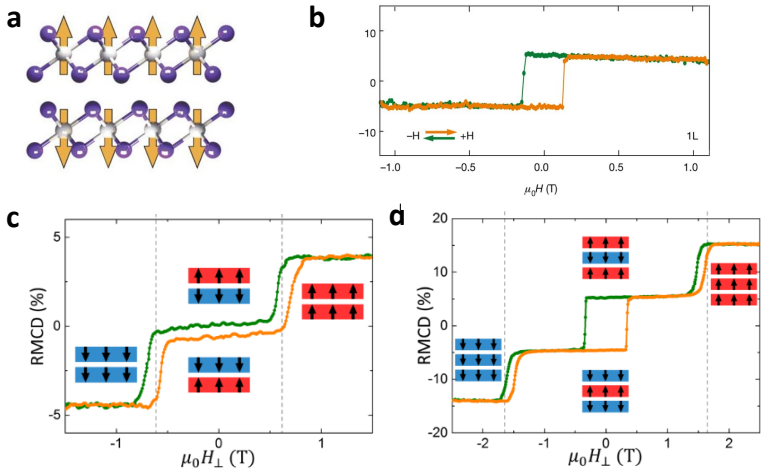

Figure 6.1.2 Layered magnetism in CrI_3. **a** Side view of CrI_3 bilayer with arrows indicating the alignment of the magnetic moments of each chromium site. **b** Magnetic field dependent Kerr rotation measurement of monolayer CrI_3. Colored arrows indicate field sweep direction. **c, d** Magnetic field dependent RMCD measurement of bilayer and trilayer CrI_3. Insets indicate the alignment of the layers' magnetic moments.

magnetic materials provide a possible solution to these challenges. One of the first discovered families of 2D magnetic materials, the chromium trihalides CrX_3, where X is Cl, Br, or I, are particularly attractive for these types of engineered magnetic structures because they encompass many different types of magnetic order within the family and remain magnetic even in the atomically thin limit. Originally discovered in bulk in the 1960s[7,185], these simple binary compounds are readily synthesized and exfoliated[13,172,186]. They consist of two layers of halide atoms sandwiching a layer of chromium atoms, which are arranged on a hexagonal lattice (fig. 6.1.1 a). The halide atoms form distorted octahedral cages around the chromium atoms, forming highly polar bonds. The resulting band structures are wide-gap semiconductors or insulators[187] (fig. 6.1.1 b), though each species hosts a number of bright localized excitons associated with d-d and charge transfer transitions appropriate to the distorted octahedral crystal field around the chromium (fig. 6.1.1 c-d)[188].

The magnetic order they host originates from spin-polarized half-filled chromium d orbitals, and is stabilized by strong magnetocrystalline anisotropy due to spin orbit coupling[189], a thermodynamic requirement for 2D magnetism[190]. Interactions between the spin polarized chromium sites are mediated by superexchange through the halide sites. The magnitude and sign

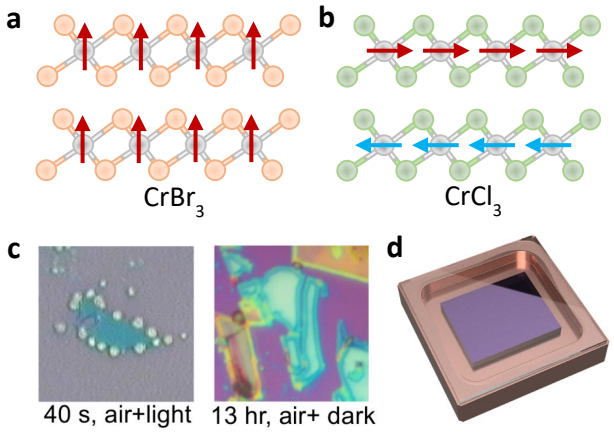

Figure 6.1.3 A family of air-sensitive layered magnets. **a, b** Side view of $CrBr_3$ and $CrCl_3$ bilayers with arrows indicating the alignment of the magnetic moments of each chromium site. **c** (left) Exfoliated flake of CrI_3 exposed to room air and light for 40 seconds. Lightly colored dots are hydrated/degraded areas. (right) Exfoliated flake of CrI_3 exposed to air in the absence of light for 13 hours. Discolored halos around flakes have degraded. **d** Copper sample capsule (spacer) containing a silicon wafer, sealed from the ambient environment by a glass window adhered with vacuum grease.

of that exchange interaction is highly sensitive to the bonding angles of the halides, as described by the Goodenough-Kanamori-Anderson rules[191–194]. Interactions between layers are mediated by *super-superexchange* interactions between Cr sites in adjacent layers via the pair of halide layers between them, which is also highly sensitive to geometry, e.g. stacking order[195].

CrI_3 was the first member of the family to be isolated and studied in the atomically thin limit, and these initial studies culminated in two major discoveries. First, it was found that magnetism in CrI_3 persists down to monolayer thickness[13], the first demonstration of magnetism in the truly 2D limit. Second, it was discovered that, while bulk crystals of CrI_3 are ferromagnetically ordered with out-of-plane magnetization, thin exfoliated samples have layered antiferromagnetic order. In other words, spins within a given layer are ferro-magnetically aligned in the out of plane direction while adjacent layers have their magnetization aligned in the antiparallel direction (fig. 6.1.2 a). As a result, with no applied magnetic field, samples with an even number of layers have zero net magnetization, while samples with an odd number of layers have a net magnetization equal to that of exactly one layer. When an out-of-plane magnetic field is applied to monolayer samples, the magnetic response is a single rectangular hysteretic loop, characteristic of highly anisotropic ferromagnetism (fig. 6.1.2 b). In multilayer samples, the antiferromagnetic coupling between layers can be overcome by an out-of-plane magnetic field, resulting in layer-wise spin-flipping transitions at critical fields. The resulting magnetization curve

is reminiscent of the stairstep magnetism of SAFs[196], with the number of steps equal to the number of layers (fig. 6.1.2 c-d).

Since these initial discoveries, the other members of the chromium trihalide family have been studied extensively. Like CrI_3, $CrBr_3$[186] also has out-of-plane magnetic ordering within each layer, but adjacent layers are ferromagnetically coupled, resulting in a net-ferromagnetic material (fig. 6.1.3 a). On the other hand, the magnetism in $CrCl_3$ manifests with in-plane spin ordering within each layer with no directional anisotropy within the plane and AFM coupling between adjacent layers (fig. 6.1.3 b)[197]. There is a trend within the chromium trihalides of increasing magnetic ordering temperature with increasing atomic mass of the halide species, with CrI_3 having the highest Neél temperature of the family, 45 K in monolayer[186], $CrBr_3$ having a Curie temperature of 37 K in monolayer[198], and $CrCl_3$ having the lowest Neél temperature, 14 K in monolayer[197]. This result is consistent with the picture of increasing orbital size with increasing atomic mass of the halides producing larger overlap integrals which enhance the Cr-Cr superexchange interactions. It is also the case that as these materials are thinned down from bulk, their transition temperatures tend to decrease by up to 50%[172,186] as a result of increased quantum fluctuations in the smaller magnetic ensemble.

2D magnetic materials are frequently studied using the polar magneto-optical Kerr effect (MOKE) or reflectance magneto-circular dichroism (RMCD)[199]. These effects provide a convenient optical probe of out-of-plane magnetization compatible with confocal microscopy. In the case of MOKE, the out-of-plane magnetization M_z couples to the real part of the off-diagonal components of the first order polarizability tensor $\chi_{xy} = -\chi_{yx} \propto M_z$. When light polarized in the x-y plane reflects off the sample, the polarization angle rotates in the plane by a characteristic angle $\theta_k \propto M_z$. RMCD is a result of M_z coupling to the *imaginary* part of χ_{xy}, and manifests as a difference in the reflectivity for right- and left-handed circularly polarized light. Unlike Kerr rotation, which is directly proportional to the magnetization, the dependence of the RMCD signal on magnetization is nontrivial. This is manifestly clear from the fact that θ_k is unbounded (the rotation can wrap around any multiple of 2π), while the circular dichroism, when defined as $\mathrm{RMCD}=(R_+ - R_-)/(R_+ + R_-)$ can not exceed ± 1. Since macroscopic magnetization density is

not physically bounded, it is clear that the RMCD signal must not have a linear dependence on M_z.

On the other hand, since these two effects are governed by the real and imaginary components of the same polarizability matrix element, they are related to one another through the Kramers-Kronig relations, and given knowledge of the broadband spectral response of one of these two effects, the response of the other can be calculated. The MOKE and RMCD spectra of a given material are sensitive to its electronic (and in some case vibrational) resonances[200]. This can significantly impact the measurement of either effect if probed using a fixed single wavelength of light tuned in proximity to a resonance since, in general, a resonance energy may shift due to changing magnetization or magnetic field (i.e. from the Zeeman effect or diamagnetic effects). Moreover, the optical dipole of an electronic transition can couple directly to magnetization, resulting in brightening or darkening of the transition[188]. Despite these complications, it is often beneficial to use nearly-resonance optical probes to measure MOKE and RMCD, as long as the detuning is sufficient that the effects discussed above can be assured to play a small role in the magnetization dependence of the measurement. Away from resonances, MOKE and RMCD are generally very weak (RMCD nearly vanishes below the electronic band gap, for example), and the signal enhancement *near* a resonance can significantly improve signal quality. The techniques used to measure these effects are detailed in appendix B.

An unfortunate liability with these materials is their chemical instability in the presence of water and oxygen which quickly degrade the material, a reaction which is hastened by exposure to light or elevated temperatures (fig. 6.1.3 c)[201]. They must therefore be exfoliated and handled entirely inside an inert gas environment like a nitrogen or argon glovebox. They can be doubly encapsulated between layers of air-stable 2D materials like hexagonal boron nitride or graphene to shield them from contact with air, but the fabrication of such layered samples by van der Waals transfer must also be carried out within a glovebox. But because the reaction of CrX_3 with moisture and oxygen is enhanced by high temperature, even in a glovebox with <0.5 ppm O_2 and H_2O, high temperature transfers can sometimes lead to the degradation of thinner samples. It is often much more convenient to avoid transfers altogether if a simple exfoliated sample is all that is needed for an experiment. To do so, the sample must be prepared inside a

sealed sample vessel, typically a block of high purity copper with a milled pocket, sealed with a thin glass window and vacuum grease (fig. 6.1.3 d).

Nevertheless, for the fabrication of functional 2D devices involving chromium trihalides, assembly by van der Waals transfer usually can't be avoided. Even to make electrical contacts with exfoliated layers, they must be protected from oxygen and moisture for standard lithography techniques used to create electrodes. Transfers done with these materials are done at lower temperatures than usual to mitigate risk of degradation, around 40-60° C as compared to the more common 90-130° C temperature range. But the ability to assemble multilayer stacks incorporating chromium trihalides, especially CrI_3, have produced numerous remarkable results that demonstrate the potential for utilizing layered magnetism in van der Waals devices[35,202]. The first realization of a magnetic van der Waals device based on CrI_3 was in heterostructures of multilayer CrI_3 and monolayer WSe_2. Zhong *et al.*[203] discovered that the valley pseudospin in WSe_2 can be strongly manipulated by the magnetic order in CrI_3. This is the result of valley-selective charge transfer from the WSe_2 to the CrI_3—only charges whose spins are aligned with the magnetization of the CrI_3 layer that the WSe_2 is contacting are able to hop into the CrI_3, thus selectively depopulating one valley of the WSe_2. This results in fixed circularly polarized PL emission from the WSe_2 originating from the valley which is *not* depopulated by charge transfer. Furthermore, valley-selective exchange interactions produce an energy splitting between the valleys which is equivalent to the Zeeman splitting produced by a magnetic field of around 14 T. A corollary to this effect has also been demonstrated, in which optical pumping of the WSe_2 layer can be used to control the magnetic order of the interfaced CrI_3.[204] As the excitation density is increased, the critical field required to induce the spin-flip transition of a CrI_3 decreases. This effect is distinctly not thermal in origin, as the excitation energy dependence reveals that excitation resonant with the WSe_2 A exciton enhances the effect. It has been shown separately that electrostatic control of CrI_3 bilayers can tune the spin-flip critical field, and in particular that hole doping can decrease the critical field[202]. Given that the hole-type charge transfer from WSe_2 to CrI_3 must be faster than the sub-ps lifetime of the excitons in WSe_2, and given that the charge imbalance this creates relaxes nonradiatively, the continuous excitation of the WSe_2 leads to a

pileup of charge and effective hole doping of the CrI_3, consistent with the result in the case of direct electrostatic gating.

6.2 Halide mixing for controlling magnetic coupling in chromium trihalides

The electrostatic and optical control of magnetism in CrI_3 discussed in section 6.1 make possible the precise extrinsic control of the IEC in CrI_3, but the magnitude of these effects remain small compared to the degree of controllability in SAFs, in which the IEC can be continuously tuned from AFM to FM[173]. This control is realized by tuning the thickness of the nonmagnetic barriers in SAFs during growth, and necessarily lacks *in situ* tunability for SAF devices. However, were such an intrinsic control available for chromium trihalides, it could potentially be combined with optical or electrostatic control to substantially broaden the overall customizability of these materials for practical device design. Given the isostructuralism of all members in this chemical family[205], it raises the possibility that their halide constituents can be partially interchanged or mixed to form new solid solution materials with the chemical formula CrL_xM_{3-x}, where L and M are different halogens. Whether or not the resulting mixed halide materials would host stable magnetism is not clear from first principles. The growth and study of such materials was initially carried about by Tafti *et al.*[206], in which $CrBr_xCl_{3-x}$ was grown and was demonstrated to have macroscopic magnetic properties which fell part way between the two parent compounds. Given that they are both layered antiferromagnets but have opposite anisotropy (with $CrBr_3$ having out-of-plane magnetization and $CrCl_3$ having in-plane magnetization within a given layer), the resulting solid solutions appeared to have a canted magnetic easy axis. Furthermore, their magnetic transition temperatures fell in between the transition temperatures of the parent compounds, trending monotonically as the composition parameter *x* was varied. However, the work did not rule out the possibility of chemical domain formation, and since the measurements made were directly probing the macroscopic magnetization vector, the averaging of a mixture of domains with out-of-plane and in-plane anisotropy would result in an apparently canted anisotropy, and interactions between domains could stabilize magnetism at an intermediate temperature[207] (in the mean-field sense). These preliminary studies were therefore unable to

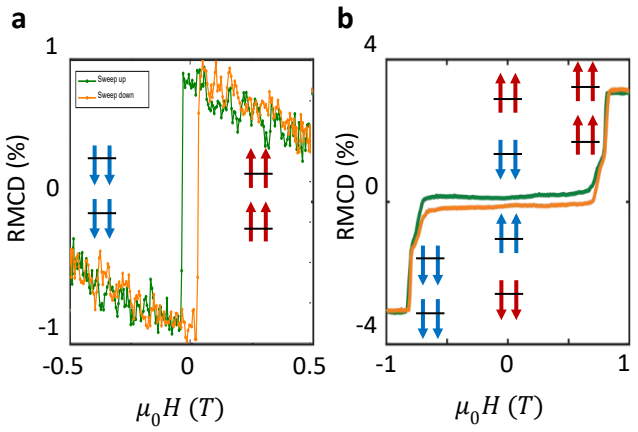

Figure 6.2.1 Comparison of RMCD field sweeps on **a** bilayer $CrBr_3$ and **b** bilayer CrI_3. Insets indicate the layered magnetic order in each configuration.

unequivocally establish that the technique of halide mixing in synthesis could be used to design materials with customized IEC and magnetic anisotropy. However, these limitations could be overcome by studying solid solution chromium trihalides using *microscopic* measurement techniques instead. To that end, we have studied exfoliated samples of a series of solid solutions of the form CrI_xBr_{3-x} using a number of microscale optical techniques.

To establish the baseline properties of this chemical family, the magnetization curves of bilayers of the two limiting members with x=0 ($CrBr_3$) and x=3 (CrI_3), measured by RMCD (see appendix B) using a 633 nm laser at a sample temperature of 1.6 K, are shown in figure 6.2.1 a and b, respectively. All following measurements were performed under these conditions unless otherwise stated. The bilayer of $CrBr_3$ has a single rectangular hysteresis loop centered at $\mu_0 H = 0\ T$ and a coercive field of $\mu_0 H_c = 0.028\ T$, with a slightly sloped background due to the slight magneto-circular dichroism of the objective lens. On the other hand, the bilayer CrI_3 has the expected staircase magnetization profile characteristic of layered antiferromagnetism with a spin flip transition at $\mu_0 H_c = 0.75\ T$ and appears to lack the sloped background visible in the $CrBr_3$ data. This is because the magnitude of the RMCD for $CrBr_3$ at 633 nm is less than 25% of the magnitude of the CrI_3 RMCD at the same wavelength, as this wavelength is near the $LMCT_1$ charge transfer transition in CrI_3 which provides pseudo-resonant enhancement of the circular dichroism. The nominally antiferromagnetic zero-field configuration of the CrI_3 appears to produce a non-zero RMCD signal, effectively opening the loop and giving the appearance of an open hysteresis loop. We speculate that this is the result of symmetry breaking from sample environment, as the sample has vacuum on one side and an SiO_2 substrate on the other[35,202]. It is known that the zero-field layer magnetization configuration of bilayer CrI_3 depends on the magnetic field sweep direction, with one sweep direction producing the ↑↓ configuration and the

other direction producing the time reversed ↓↑ configuration[35,208], where the first arrow indicates the magnetization direction of the top layer and the second arrow indicates the magnetization direction of the bottom layer. If the contribution of the two layers to the RMCD signal is unequal, the two possible ground states would produce opposite nonzero net RMCD signals, even if the magnetization is effectively zero. The spin flip transition of the bilayer CrI_3 also appears to onset gradually; this is due to the formation of domains which partially fill and eventually traverse the beam spot during the magnetic field sweep, as described by Huang *et al.*[13].

The introduction of the complementary halide into the lattices of $CrBr_3$ and CrI_3 at low levels (x = 0.44 and x = 2.6, respectively) produces clear changes in the magnetic behavior in both compounds. Figure 6.2.2 a shows the magnetic behavior of bilayer $CrI_{0.44}Br_{2.56}$. Like its parent compound, it has a single rectangular hysteresis loop, although the coercive field is increased to $\mu_0 H_c = 0.032\ T$, a change of approximately 15%. Given that both parent compounds have similar exchange interaction strengths, but CrI_3 has far greater magnetic anisotropy compared to $CrBr_3$[209], this is a clear indication that the halide mixing acts to change the effective global magnetic anisotropy, regardless of whether chemical domains are formed. If chemical domains are indeed present, they must be small enough that the long range magnetic interactions act to stabilize the global magnetic order with properties that are on average somewhere between those of either parent compound. Likewise, the magnetic behavior of $CrI_{2.6}Br_{0.4}$ is similar to that of CrI_3, showing the characteristic stairstep magnetism, albeit with a substantially reduced spin flip transition field of $\mu_0 H_c = 0.45\ T$, a reduction of approximately 40% (fig. 6.2.2 b). This demonstrates immediately that the strength of the IEC in layered antiferromagnets can be substantially tuned using the technique of halide mixing. And once again, if chemical domains are present in the sample, they don't appear to manifest as separate magnetic domains, as the resulting signal would appear as a superposition of ferromagnetic and antiferromagnetic magnetization curves.

The outcome is somewhat different in the case of heavily mixed solid solutions in the vicinity of x = 0.95 to x = 1.1. Figure 6.2.2 c shows the magnetization curve of a bilayer with x = 0.95 showing a well-defined rectangular hysteresis loop and a large coercive field of $\mu_0 H_c = 0.18\ T$, consistent with the trend established by the bilayer with x = 0.44. However, other sample

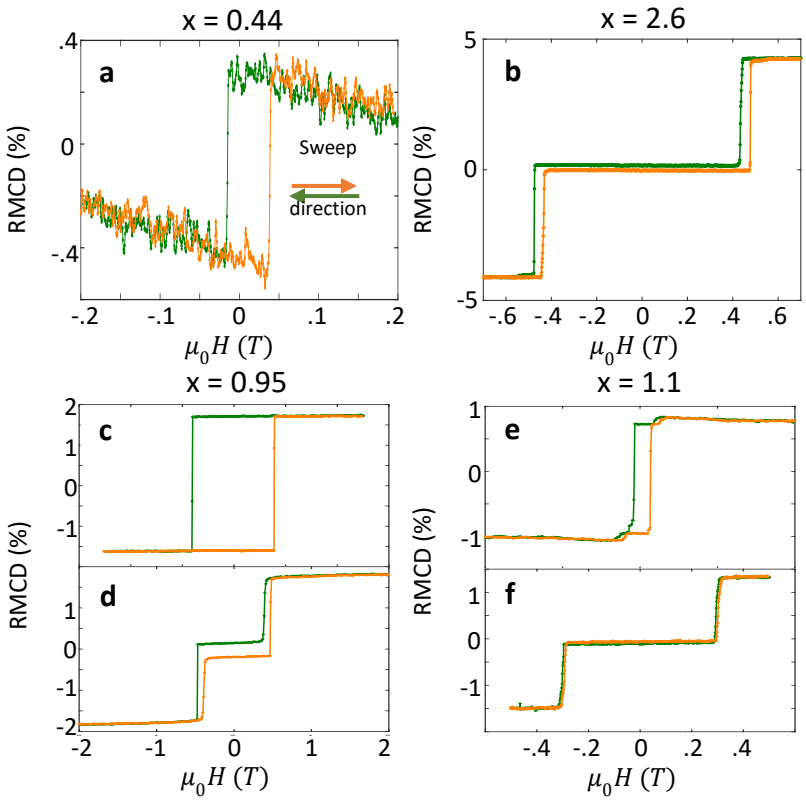

Figure 6.2.2 Control of bilayer magnetic order by halide composition. **a, b** RMCD field sweeps taken on bilayer CrI_xBr_{3-x} for x = 0.44 and x = 2.6. The former, having predominantly bromide, behaves ferromagnetically. The latter, having predominantly iodide, behaves antiferromagnetically. **c-f** RMCD field sweeps taken on bilayers with x = 0.95 and x = 1.1. For different exfoliated flakes of either composition, both ferromagnetic and antiferromagnetic order can be seen.

flakes from the same exfoliation with nominally identical chemical composition show antiferromagnetic stair-step magnetization (fig. 6.2.2 d). This mixture of observed behaviors across a single exfoliation is reproducible in samples with x = 1.1 (figs. 6.2.2 e-f). The inconsistency of results from different flakes from a single exfoliation raises questions about the chemical homogeneity of the bulk crystals from which the samples were exfoliated. Since the bulk crystals were synthesized by chemical vapor transport which produces directional growth, it is possible that reaction or crystal growth dynamics could favor the formation of different mixtures at different points in the growth of a single crystal. When the crystal is cleaved apart during the exfoliation process (described in section 2.1), this would produce a varied distribution of compositions and thus a distribution of compositions among the exfoliated flakes.

However, we have isolated single microscopic flakes with nominal compositions of x = 0.95 and x = 1.1 which host both ferromagnetic and antiferromagnetic domains, thus excluding the possibility of macroscopic chemical inhomogeneity. Figure 6.2.3 a shows a spatially-resolved RMCD map of a bilayer with composition x = 1.1 at zero applied magnetic field, following initialization at a positive magnetic field. In this color map, red corresponds to positive magnetization, white corresponds to zero magnetization, and blue corresponds to negative magnetization. This flake has a pair of small antiferromagnetic domains (white) with a lateral width of 1-2 micrometers near its center, which are surrounded entirely by ferromagnetic domains (red). A brightfield micrograph of the flake (fig. 6.2.3 b) shows that it has homogeneous optical contrast, indicating that there are no gross defects or varying sample thicknesses in the domain regions. Moreover, the domain patterns are found to be stable through thermocycling above and below the transition temperature, indicating that their coexistence is not merely thermodynamic in nature but is governed by some underlying structure.

To study these domains more carefully, a series of magnetic field sweeps were carried out with the RMCD probe beam situated at different points along the flake, starting from the AFM domain and moving into the FM region (figs. 6.2.3 c-f). Given that the size of the beam spot (approx. 2 μm) is similar to the size of the domains, it was impossible to sample the AFM domain without also slightly sampling the surrounding FM region. Nevertheless, the spot centered on the AFM domain is dominated by stairstep magnetization, and as the beam spot moves further and further into the FM region, the magnetization transitions to a square hysteresis loop. In all of the magnetization curves measured in this series, a combination of AFM and FM behavior is observed, but notably, the spin-flip transition field associated with the AFM order is consistently around $\mu_0 H_c = 0.25\ T$, and the ferromagnetic coercive field is consistently around $\mu_0 H_c = 0.19\ T$. This suggests that the unusual multi-step magnetization seen in all cases is simply a superposition of both behaviors. Regardless of the origin of these domains, their coexistence and the deviation of their critical magnetic fields from those of the parent compounds indicates that on the microscale, halide mixing is a viable technique to tune the inter- and intralayer exchange couplings in chromium halides over a broad range, up to and including through a sign change in the interlayer coupling.

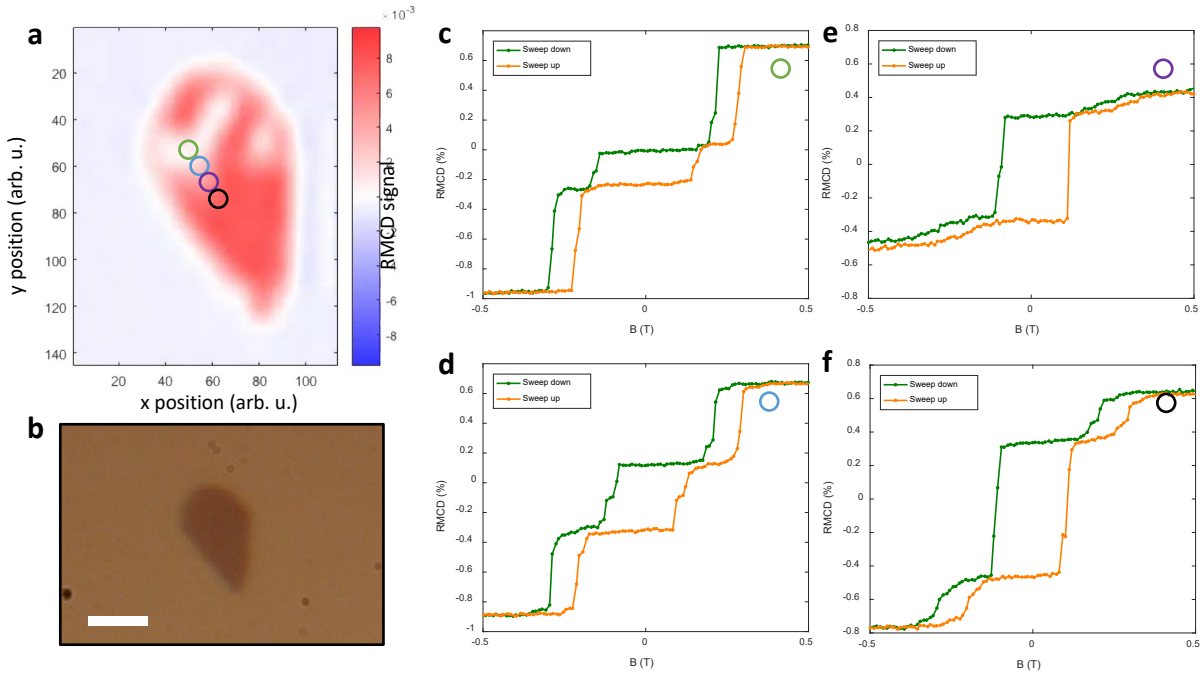

Figure 6.2.3 Coexistence of ferromagnetic and antiferromagnetic domains at critical compositions. **a** RMCD map of a flake of exfoliated $CrBr_{1.9}I_{1.1}$ taken at zero magnetic field, showing ferromagnetic regions (red) and antiferromagnetic regions (white). **b** Optical micrograph of the above sample for reference. Scale bar is 5 µm. **c-f** RMCD field sweeps taken on different spots across the flake. Colored open circles indicate the location of data acquisition on the RMCD map. The diameter of the circles approximates the beam spot size.

But while this discovery suggests that macroscopic chemical inhomogeneity is not responsible for the inconsistency of magnetic order in this critical range of compositions, it forces us to also consider that there may be microscopic chemical inhomogeneity, on the order of the magnetic domain size or even much smaller. While measurement techniques like MOKE and RMCD are capable of resolving magnetic domains, they aren't useful for studying chemical composition or crystal structure, and instead we turn to other optical probes which are more directly sensitive to local structure. The first of these is Raman spectroscopy, in which the optical phonon spectrum of the material is measured through optical spectroscopy of Raman-scattered light. This technique is ubiquitous is chemical analysis and material science, and is useful for both chemical and structural analysis as the optical phonon spectrum and light-matter coupling depend on bond coordinates, bond rigidity, and local symmetry[210]. Figure 6.2.4 a-c shows the Raman spectra of CrI_3, $CrI_{0.9}Br_{2.1}$ and $CrBr_3$ taken using a Rayleigh wavelength of 633 nm. For a

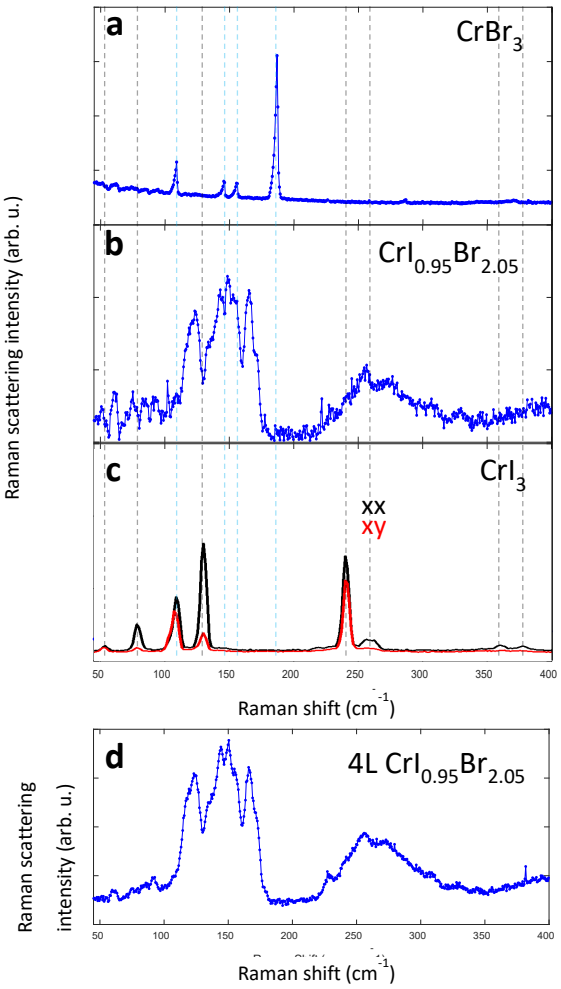

Figure 6.2.4 Hybridization of the Raman spectrum of $CrI_{0.95}Br_{2.05}$. **a-c** Raman spectra taken on bulk samples of $CrBr_3$, $CrI_{0.95}Br_{2.05}$, and CrI_3. Dashed gray lines indicate the main Raman peaks found in CrI_3, while dashed blue lines indicate those of $CrBr_3$. The red and black lines in the CrI_3 spectrum correspond to co-linearly and cross-linearly polarized Raman spectra. **d** Raman spectrum of four-layer $CrI_{0.95}Br_{2.05}$, nearly identical to the bulk spectrum.

more detailed description of the measurement technique, see appendix B. While the Raman spectra of the pure parent compounds consist of narrow, well defined peaks, the Raman spectrum of the mixed halide compound presents with a broad mass of numerous ill-defined peaks. Perhaps most importantly, the prominent vibrational modes of the parent compounds aren't strongly present in the Raman spectrum of the mixed halide compounds. Both CrI_3 and $CrBr_3$ have four dominant Raman peaks at low energy, with the peaks in CrI_3 falling between 50 and 150 cm^{-1}, and the peaks in $CrBr_3$ falling between 100 and 200 cm^{-1}. CrI_3 has an additional pair of peaks around 250 cm^{-1} associated with the antiferromagnetic interlayer coupling. In $CrI_{0.9}Br_{2.1}$, the lower energy Raman manifold falls roughly in the energy range of the peaks in $CrBr_3$, although the exact positions of the peaks don't line up well between the two, and there exists a higher energy manifold approximately in the same energy range as the peaks associated with AFM order in CrI_3, but broadly smeared out an even so not lining up exactly in energy. The spectrum of the mixed halide compound appears to be completely distinct and fully hybridized, suggesting that the material is chemically well-mixed, and that there aren't segregated domains of predominantly one halide or the other. The spectrum in atomically thin samples is almost identical to that of bulk. The Raman spectrum shown in fig. 6.2.4 d comes from

an exfoliated four layer sample from a different crystal batch altogether, confirming that the particular Raman spectrum of this composition is not stochastic or random at all, but composed of specific, characteristic modes, which we speculate correspond to the normal modes of the multitude of different atomic arrangements within a unit cell which are possible in these mixed halide compounds.

Given the strong evidence for chemical homogeneity, there remains only the possibility of the domain pattern being the result of a type of structural inhomogeneity that Raman spectroscopy is insensitive to. Recent theory work has elucidated the role of stacking order in determining the IEC in CrI_3[195]. There are two nearly degenerate stacking orders for CrI_3, corresponding to rhombohedral and monoclinic phases. In as-grown bulk, which is ferromagnetic, the former is favored at low temperatures below around 230 K, while the latter is favored at high temperatures. Calculations have shown that the rhombohedral phase produces ferromagnetic IEC, while the monoclinic phase produces antiferromagnetic IEC. It then stands to reason that during the mechanical exfoliation process, which necessarily deforms the crystals, they could possibly undergo a structural transition at room temperature to the monoclinic phase and remain with that stacking order through thermocycling. This effect was recently demonstrated by high pressure studies[211], which showed that by applying a pressure of over 2 GPa, exfoliated samples can be converted back to the rhombohedral phase and become ferromagnetic again. Applying this result to the mixed halide samples, we speculate that, due to deformations in the lattice of each layer, strain domains form which trap different regions of an exfoliated crystal in a particular structural phase. The strain domains themselves are inherent to the mixed halide chemistry; since the Cr-Br and Cr-I bond lengths are different[205,209], it is inevitable that the lattice will be corrugated and irregular if the halide species are well mixed. While this discussion is speculative, there are a number of possible experimental techniques that could resolve the question definitively, such as tip-enhanced Raman spectroscopy, which could reveal strain domains with a lateral resolution of a few nm, or perhaps most simply, the application of high pressure to rearrange the lattice as was demonstrated by Song *et al.*

7 - Optical properties of the magnetic semiconductor Chromium Sulfur Bromide

In this chapter, we introduce a newly discovered 2D magnetic material, chromium sulfur bromide, or CrSBr. We investigate the basic optical properties of exfoliated flakes of CrSBr through absorption and photoluminescence (PL) spectroscopy. We find that the layered antiferromagnetic (AFM) order of thin flakes of CrSBr heavily influences their optical spectra.

7.1 Optical excitations in chromium sulfur bromide

Magnetic semiconductors are of technological and theoretical interest due to coupling between electronic structure and magnetism[212–214] which enables spintronic and magnetoelectic effects like spin injection[215], magnetoresistive devices[216], and direct-read magnetic memory[217]. If a magnetic semiconductor also has a direct band gap or optically allowed crystal field transitions, it may photoluminesce, adding light emitting and processing technologies to the list of potential uses[218,219]. Selection rules for optical transitions are influenced by global symmetry, combining symmetries from the crystal lattice, electronic orbitals, and spin/magnetic order present in the material. It then stands to reason that control of magnetic order, e.g. through temperature or external magnetic field, may generally impact the optical properties of a magnetic semiconductor and offer new routes to material control. However, the number of magnetic semiconductors that have been discovered remains small, some elementary examples being the europium chalcogenides[220–222] and magnetite (iron(II,III) oxide, Fe_3O_4)[223]. While photoluminescence has been reported in the former, neither are good semiconductors and neither have garnered great attention for technological applications.

An alternative approach to harness the combined power of semiconductors and magnetic materials is to endow an existing semiconductor with magnetic properties through chemical doping to create what is referred to as a dilute magnetic semiconductor, or DMS[212,224]. The approach typically used to create a DMS is to incorporate transition metal ions with strong spin-orbit coupling and unpaired electrons at a low concentration into the growth of a conventional

semiconductor. Success has been found with a wide range of semiconductors, including group III-V, IV-VI, and II-VI semiconductors. Among the semiconductors which have been incorporated into DMSs, a number have direct band gaps, including gallium arsenide[218] and zinc oxide[225]. Given the large spacing between the magnetic ions, the magnetism in DMSs is mediated by free carriers[226]. The Curie temperature of these materials tends to be well below 100 K, but they tend to be highly controllable, as depleting or supplementing the carriers that mediate the magnetism through electrostatic gating can tune the magnetic behavior substantially[227,228]. At higher doping levels, magnetic interaction between the dopant spins can be governed by superexchange, establishing much stronger magnetic order than in low concentration DMSs with low dopant concentrations and boasting Curie temperatures well above 100 K[229].

Retreading the theme of long-forgotten van der Waals materials discovered many decades ago and revisited in the present 2D materials boom, there exists a largely unexplored family of magnetic semiconductors (at the time of writing), the chromium chalcogen halides, which potentially have attractive properties for device applications and a number of unexplored theoretical facets[230,231]. This family contains numerous members, many of which are semiconducting, and many of which host magnetism with a magnetic ordering temperature over 100 K or even up to room temperature[232,233]. Their crystal structure is highly anisotropic (fig. 7.1.1 a) with a rectangular unit cell which includes 2 atoms each of chromium, chalcogen, and halide. The ligands coordinate in a distorted octahedral cage around the chromium sites, with the chromium linked by chalcogens along the **a** and **b** crystal directions and additionally by the halogens along the **a** direction. Like with the chromium trihalides discussed in chapter 6, the magnetic polarization within a layer of a chromium chalcogen halide lies primarily at the chromium sites and is mediated by superexchange through the attached ligands. In this case, the magnetic behavior is best captured by the anisotropic Heisenberg model, and depending on choice of ligands can produce easy axes in the a, b, or c crystal directions. In addition to this rich magnetic behavior, they are predicted to have high carrier mobility with strong anisotropy due to mass anisotropy at the band edge, making them potentially useful for electronic applications.

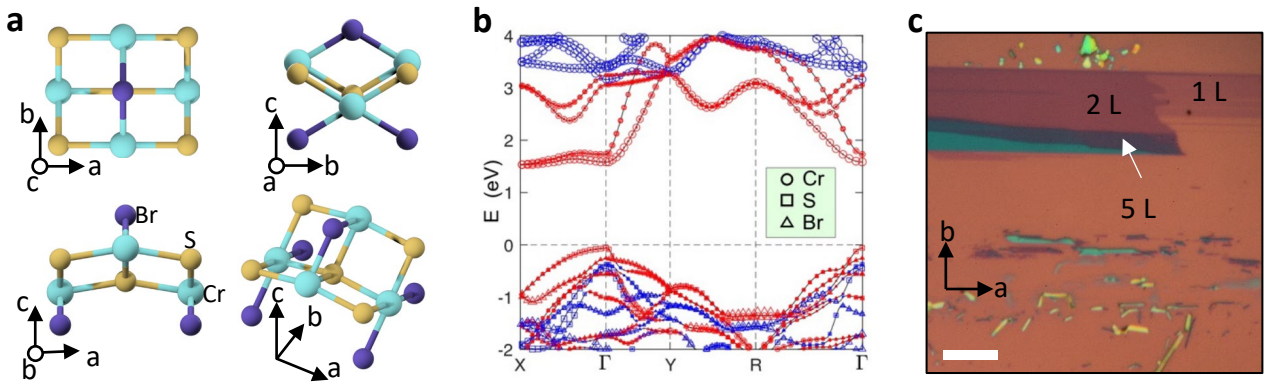

Figure 7.1.1 Properties of CrSBr. **a** The unit cell of CrSBr. **b** Orbital-resolved calculated band structure of bulk CrSBr. Majority spin bands are in red, minority spin bands are in blue. **c** Brightfield micrograph of assorted thicknesses of exfoliated CrSBr (1 layer, 2 layer, and 5 layer are labeled.) Scale bar is 5 μm.

In this chapter, we will focus on one particular member of this family, CrSBr. Density functional theory calculations[233] (fig. 7.1.1 b) predict a valence band maximum (VBM) at the Γ point of the Brillouin zone and nearly degenerate Γ and X points as conduction band minima (CBM), with a gap energy of 0.5 to 1.7 eV[232,233] (DFT notoriously underestimates band gaps). Of note is the considerable mass anisotropy in both the conduction and valence bands at Γ, with light electrons and holes along the $\Gamma - X$ direction and heavy electrons and holes along the $\Gamma - Y$ direction. The orbital composition of the bands is primarily from the sulfur in the valence band and chromium in the conduction band. Given the anisotropy of the electronic structure, we might expect the optical properties to be highly anisotropic as well.

While this material is nominally air stable, others have reported that thin samples can degrade on unpassivated SiO_2 substrates[234]. To this end, samples reported below were exfoliated onto Si/SiO_2 substrates passivated by 1-dodecanol inside an inert gas glovebox at less than 0.5 parts per million O_2 and H_2O. Sample thickness was identified by optical contrast as described in section 2.2. Figure 7.1.1 c shows an image of an exfoliated sample of CrSBr with numerous layer thicknesses identified by optical contrast. Crystal axes of exfoliated samples were determined based on the orientation of the needle-like bulk crystals during exfoliation, whose long axis has been identified by prior x-ray diffraction experiments to be the **a** direction[235]. The exfoliated samples were then loaded into a copper spacer and sealed with a glass cover slide using vacuum

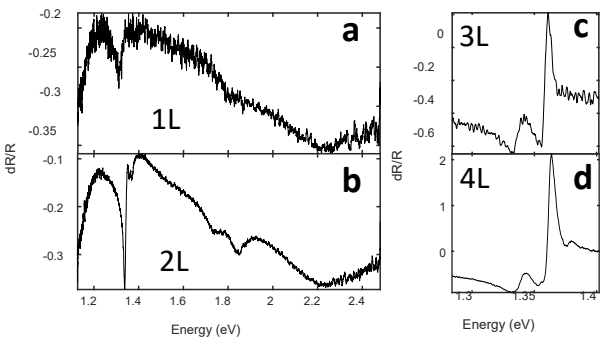

Figure 7.1.2 Low-temperature reflectance spectrum of CrSBr. **a, b** The broadband differential reflectance spectra of monolayer and bilayer CrSBr. Fast oscillations are due to thin film interference in the cryostat's vacuum window. **c, d** Differential reflectance spectra of three and four layer CrSBr focused on the energy region around the ground state exciton.

grease, as described in section 6.1 before being transported to a cryostat for measurement. Unless otherwise specified, all measurements took place at a temperature of 5 K.

The optical white-light reflectance spectrum of a monolayer sample of CrSBr is shown in figure 7.1.2 a. The data were taken using an unpolarized thermal light source, and the raw reflected intensity spectra were converted to normalized differential reflectance spectra by first subtracting and then dividing by the reflected intensity spectrum of the surrounding substrate. There is one clear absorption resonance in the measured energy range, located at 1.313 eV. When the same measurement is made on the bilayer, the strength of this resonance is increased substantially and the energy shifts to a somewhat higher energy, around 1.338 eV. Furthermore, we can clearly see a pair of higher energy resonances around 1.73 and 1.85 eV (fig. 7.1.2 b). Given the proximity of several other, more deeply bound band extrema to the VBM and CBM[232], it is possible that the observed higher energy resonance are their corresponding optical transitions. However, we will focus on the energy region surrounding the lowest lying resonance, which presumably corresponds to the ground state excitation.

Curiously, as the sample thickness increases beyond bilayer, the complexity of the reflectance spectrum around 1.3-1.4 eV increases, with two resonances visible in the trilayer sample at 1.338 and 1.359 eV (fig. 7.1.2 c), and three resonances in the four-layer sample at 1.337, 1.356, and 1.376 eV (fig. 7.1.2 d). In samples thicker than four layers, the number of resonances appears to be fixed at 3 (see appendix c, supplementary data for chapter 7). Notably, the complexity of the high energy reflectance spectrum does not seem to increase beyond the two peaks around 1.7-1.9 eV which become visible in bilayer samples.

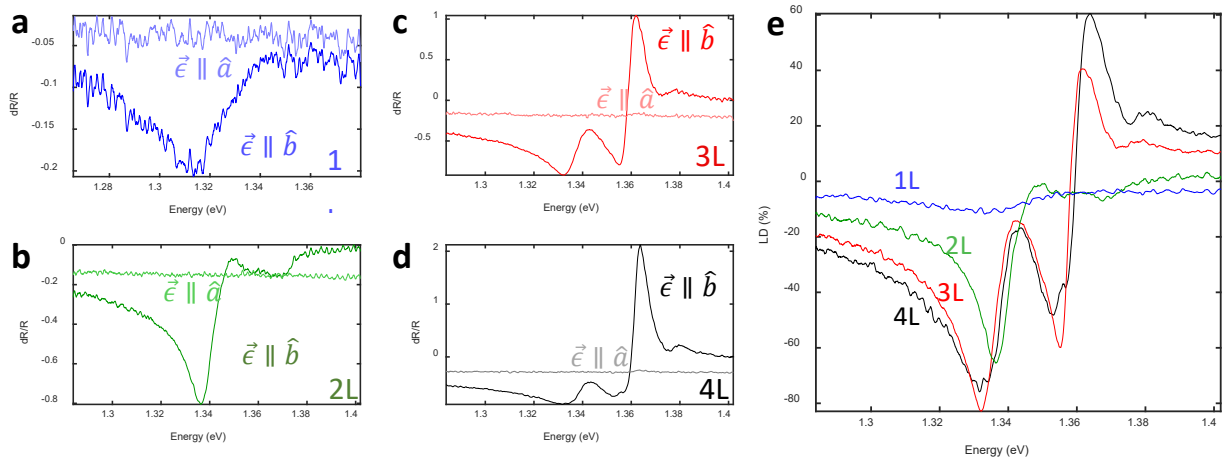

Figure 7.1.3 Linear dichroism in CrSBr. **a-d** Differential reflectance spectra of 1-4 layer CrSBr with the reflected polarization analyzed along the crystal $\hat{a}$ and $\hat{b}$ directions in the vicinity of the ground state exciton manifold. **e** linear dichroism of 1-4 layer CrSBr, with linear dichroism (LD) defined as $(I_b - I_a)/(I_b + I_a)$, where I_j is the reflected intensity of light along the j^{th} crystal axis.

When the polarization of the reflected light is analyzed in the vector basis corresponding to the **a** and **b** crystal directions, substantial linear dichroism is evident for the monolayer absorption resonance (fig. 7.1.3 a). In fact, the resonance peak is completely absent from the **a** direction and maximized along the **b** direction. And once again, this behavior is replicated in the bilayer, trilayer, four layer, and thicker samples (figs. 7.1.3 b-d, appendix c, supplementary data for chapter 7, respectively). The degree of linear dichroism, defined as $(I_b - I_a)/(I_b + I_a)$, remains very high across all samples, reaching over 80% in the four layer (fig. 7.1.3 e). This strong optical anisotropy cannot be explained by band curvature anisotropy[236], and suggests instead that the optical dipole has a fixed orientation along the **b** direction, perhaps resulting from reduced crystal field symmetry due to octahedral distortion.

This hypothesis is further reinforced by photoluminescence (PL) measurements. The normalized photoluminescence spectra of monolayer through four layer CrSBr are shown in figure 7.1.4 a. The PL data were taken using a helium-neon laser at 632.8 nm with excitation polarization along the **b** crystal direction and detection of all PL polarizations by a spectrometer with CCD array. The evolution of the peak energy from 1.31 eV in monolayer to 1.34 eV in bilayer is consistent with the absorption data, as is the sudden appearance of an additional high energy peak around 1.36 eV in samples thicker than two layers. However, a PL emission line above 1.36

eV, which would presumably correspond to the absorption resonance around 1.38 eV observed in four-layer and thicker samples, is absent. Rather, a number of *lower energy* PL peaks below the dominant 1.34 eV peak emerge in thicker samples, with the complexity of the spectrum increasing with sample layer number (see appendix c, supplementary data for chapter 7 for PL data from samples thicker than four layers.) As was the case for the reflectance resonances, the PL emission has a fixed polarization axis along the **b** direction when analyzed in the **a**/**b** basis, with zero detectable PL intensity polarized along the **a** direction (fig. 7.1.4 b). When the integrated PL intensity is plotted as a function of polarization angle (fig. 7.1.4b, inset), it fits well to a $\sin^2\theta$ distribution, consistent with dipolar radiation emission with dipole orientation along the **b** direction. It follows from the reflectance dichroism that there should be some excitation polarization dependence of the PL emission. Figure 7.1.4 c presents the PL spectrum of bilayer CrSBr with the PL collection polarization fixed along the **b** direction with excitation polarization along either **a** or **b**. The spectral distribution is identical for either excitation polarization, but the intensity with excitation along **a** is about 60% lower than with excitation along **b**. The excitation polarization dependence can't be explained by linear dichroism alone, as the linear dichroism at the laser wavelength is only about 2% (fig 7.1.4 d).

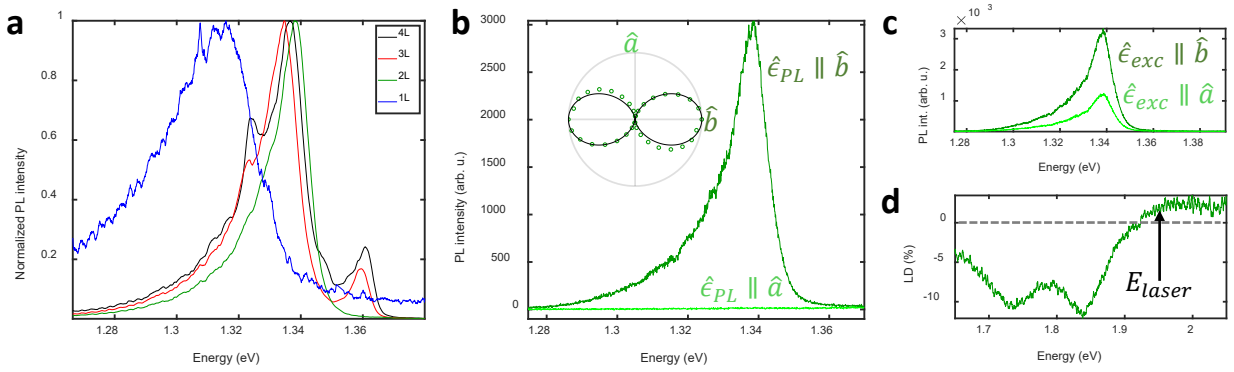

Figure 7.1.4 Photoluminescence of CrSBr. **a** Normalized photoluminescence of 1-4 layer CrSBr. **b** PL spectrum of bilayer CrSBr analyzed for PL polarization $\hat{\epsilon}_{PL}$ along the $\hat{a}$ and $\hat{b}$ crystal axes with excitation polarization along $\hat{b}$. Inset: Integrated PL intensity analyzed as a function of collection angle with a $\sin^2$ function for reference. **c** PL intensity analyzed along the $\hat{b}$ polarization direction with excitation polarization $\hat{\epsilon}_{exc}$ along the $\hat{a}$ and $\hat{b}$ crystal axes. **d** Linear dichroism spectrum in the vicinity of the laser energy E_{laser} showing the low degree of linear dichroism at E_{laser}.

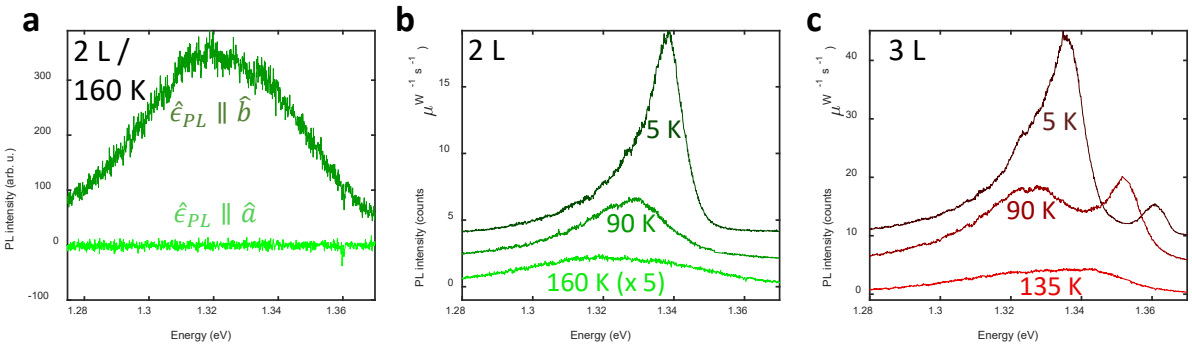

Figure 7.1.5 Temperature dependence of photoluminescence. **a** Photoluminescence of bilayer CrSBr at a temperature of 160 K with polarization analyzed along the $\hat{a}$ and $\hat{b}$ crystal axes. **b** Photoluminescence spectrum of bilayer CrSBr at two temperature below the magnetic ordering temperature (5 K and 90 K) and at one temperature above (160 K). **c** Photoluminescence of trilayer CrSBr at select temperatures showing the emergence of a high-energy PL peak (near 1.36 eV at 5 K) below the ordering temperature.

Aside from the high degree of optical anisotropy, the other feature of interest in the optical response of CrSBr is the layer-number dependent evolution of its PL and reflectance spectra. A valuable clue to help us understand the origin of the anisotropy and the layered behavior comes in the form of the PL temperature dependence. Figure 7.1.5 a shows the polarization-resolved PL spectrum of bilayer CrSBr at 160 K, well above the expected magnetic ordering temperature of 125-130 K for CrSBr. The PL remains linearly polarized to very high degree, indicating that the optical anisotropy is unconnected to magnetic order. Though the spectrum redshifts and becomes dimmer at the elevated temperature, it remains qualitatively similar to the low temperature spectrum (fig. 7.1.5 b). The redshift is expected from thermal expansion[237,238], and the decrease in intensity is consistent with the behavior of a direct optical transition, which brighten at low temperature due to decreased thermal activation of carriers[79]. Indirect gap transitions darken at low temperature due to the lower availability of phonons to assist the transition from the momentum-mismatched VBM and CBM. On the other hand, the PL spectrum of samples of 3 layers or great show dramatic qualitative changes from the low temperature spectrum to the high temperature spectrum (fig. 7.1.5 c). Specifically, they present with a single broad PL peak at high temperature, rather than multiple peaks as seen at 90 K and below. The width of the PL peak at high temperature is still comparable to the energy range spanned by the multiple peaks at low temperature, and if multiple peaks were present they

would likely still be distinguishable. This suggests that the peaks have either merged into a single peak or that the extra peaks have disappeared above the magnetic ordering temperature. Given that the most dramatic change in the PL spectrum occurs between 90 K and 135 K, a temperature range straddling the magnetic ordering temperature[234,235], it seems plausible that the appearance of additional peaks at low temperatures may correlate with the onset of magnetic ordering.

7.2 Layered magnetism in chromium sulfur bromide

Theoretical predictions and initial experimental results on the magnetic properties of CrSBr are in good agreement[205,232,234,235]. The magnetic easy-axis is along the **b** direction, while ferromagnetism (FM) is favored over antiferromagnetism (AFM) due to the threefold crystal field splitting of the half-filled Cr^{3+} t_{2g} orbital being small compared to the spin pairing energy, resulting in in-plane ferromagnetic order within a single layer[233]. The **a** axis has been identified the intermediate axis, and the **c** axis as the hard axis. The interlayer exchange coupling (IEC) is such that antiferromagnetic alignment of adjacent layers is preferred, resulting in layered antiferromagnetic order similar to that of CrI_3 (albeit with an in-plane, rather than out-of-plane easy axis)[234,235]. Application of an external magnetic field along the easy axis (**a**) produces stairstep like magnetization, with zero net magnetization along a low field plateau, jumping up to saturation magnetization at a critical field. When applied along the intermediate axis (**b**), spin canting occurs in which the projection of the magnetic moment along the **b** axis depending linearly on the applied field up to a saturating field. However, when applied along the hard axis, the spin canting is nonlinear, with a slower onset near zero field, increasing rapidly at higher fields, perhaps the result of spin-flopping behavior in which the spins first rotate towards the intermediate axis before finally rotating towards the hard axis.

Given the rich magnetic behavior of the bulk crystals and highly suggestive result of the PL temperature dependence presented in section 7.1, in which a single PL peak observed at high temperature transitions to a series of peaks below the magnetic ordering temperature of CrSBr, it is prudent to explore the connection between its magnetic order and optical properties by

controlling the magnetic order (i.e. by an external magnetic field) and measuring the response of the optical spectra (either by PL or reflectance). The response of the monolayer and bilayer PL spectra to a magnetic field along the easy axis are shown in figures 7.2.1 a and 7.2.1 b, respectively. Most notable is the strong field dependence of the bilayer and complete lack of field dependence of the monolayer. As the magnetic field is swept from 0 T upward or downward, the spectrum of the bilayer remains constant up to a critical field, at which the single peak at 1.338 eV either disappears or jumps to lower energy. The spectrum at high positive or negative field, beyond the critical field, is potentially composed of two overlapping peaks which are too strongly

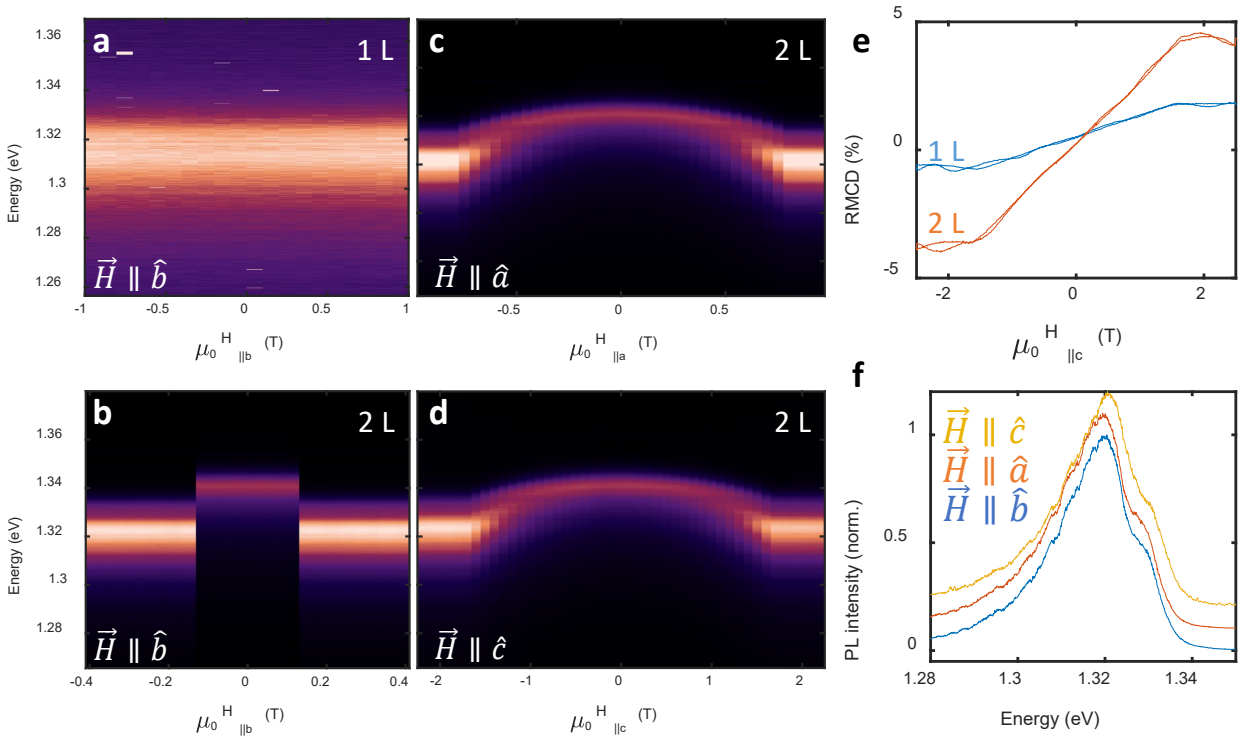

Figure 7.2.1 Magnetic response of photoluminescence in atomically thin CrSBr. **a** Normalized PL spectrum of monolayer CrSBr in a magnetic field applied along the magnetic easy axis ($\hat{b}$ direction) showing no dependence on magnetic field. **b** Normalized PL of bilayer CrSBr with a magnetic field along the magnetic easy axis showing step-like changes at a critical field. **c, d** Bilayer PL with a magnetic field swept along the intermediate ($\hat{a}$) and hard ($\hat{c}$) axes, exhibiting continuous spectral changes up to a critical field. **e** Reflectance magneto-circular dichroism of monolayer and bilayer CrSBr showing linear change in the magnetization along $\hat{c}$ up to a critical field in response to a magnetic field along $\hat{c}$, indicating spin canting behavior and confirming that the monolayer is magnetically ordered. **F** PL spectra of bilayer CrSBr at saturating fields along each crystal axis. The similarity between the spectra suggest that, although the evolution of the spectrum is different during field sweeps along each direction, the final emitting state(s) at saturating field are identical.

overlapped to distinguish by regression fitting uniquely (fig. 7.2.1 b, inset). The monolayer lacks any magnetic field response whatsoever. When the magnetic field is swept along the intermediate and hard axes (figs. 7.2.1 c-d), the bilayer PL responds by changing continuously from the zero-field spectrum up to a terminal spectrum at a critical field, beyond which the spectrum no longer evolves. As with the easy-axis field sweep, the monolayer shows no response to the application of a magnetic field along the other two axes. On the other hand, reflectance magneto-circular dichroism (RMCD) measurements show that magnetization of both the monolayer and bilayer respond similarly to the application of a magnetic field along the hard axis (figs. 7.2.1 e). Since RMCD is insensitive to in-plane magnetic moments, it cannot be used to probe the magnetic response of CrSBr to applied magnetic fields along the easy and intermediate axes. The measured RMCD signals are consistent with bulk magnetometry measurements performed by others[235], indicating that the monolayer is indeed magnetically ordered. Together with the magneto-PL measurements, this suggests that not only is the PL coupled to the magnetic order, but it is specifically coupled to the *interlayer* magnetic order, and tentatively appears to be governed by the angle between the magnetic moments of adjacent layers. This explains the sudden change in the PL spectrum when a magnetic field is swept across a the critical field along the easy axis, as the angle between the magnetic moments of the two layers of the bilayer jumps from 180° to 0°, and why the PL spectrum changes continuously when the field is swept along the intermediate or hard axes, as a result of the continuous rotation (canting) of the magnetic moments of the two layers[235]. Because the angle between the magnetic moments of adjacent layers is 0° at a saturating magnetic field, regardless of the direction, this hypothesis is compatible with the near identicality of the bilayer PL spectra at saturating fields along the three principle axes (fig. 7.2.1 f).

The behavior of the trilayer follows much the same pattern as the bilayer, with abrupt spectral changes when the magnetic field is swept along the easy axis, corresponding to layer flipping transitions, and continuous changes when the magnetic field is swept along the easy and hard axes, corresponding to continuous canting of the magnetic moments of the layers (figs. 7.2.2 a-c). Of particular interest is the magnetic field response of the high energy, 1.36 eV peak which is present below the magnetic ordering temperature in samples thicker than bilayer. The energy

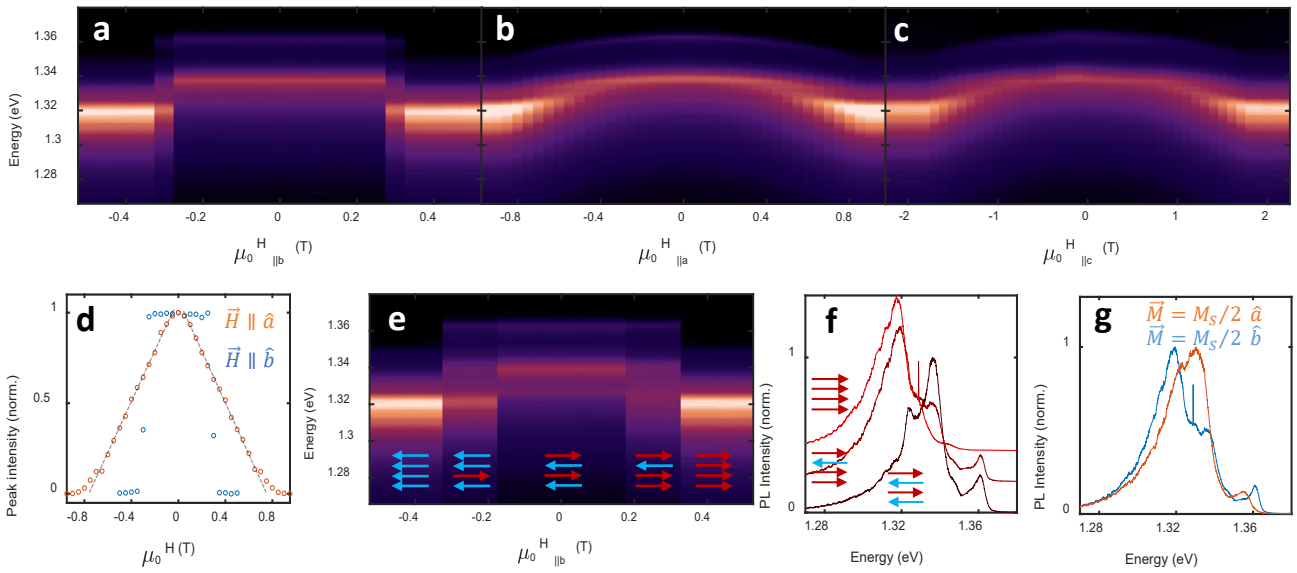

Figure 7.2.2 Layered magnetism and magneto-photoluminescence of 3 and 4 layer CrSBr. **a, b, c** Trilayer magneto-photoluminescence magnetic field sweep with the magnetic field along the easy axis, intermediate axis, and hard axis, respectively. **d** Intensity of the trilayer high energy peak (near 1.36 eV) as a function of magnetic field along the easy and intermediate axes. Straight lines are visual guides. **e** Four layer magneto-photoluminescence field sweep with magnetic field along the easy axis showing layer flipping behavior. Arrows denote magnetization direction of individual layers in the stack and represent only a few of the possible permutations. **f** Four layer PL spectra at easy-axis magnetic field values of 0.15 T, 0.3 T, and 0.45 T, corresponding to zero, half, and saturated sample magnetization. **g** PL spectra of four layer CrSBr at half magnetization along the easy and intermediate axes.

shift of this peak roughly follows the trend of the lower energy peaks during spin canting; however, as the absolute value of the magnetic field increases, the intensity of this peak falls off linearly up to the saturating magnetic field, at which point the peak vanishes completely (fig. 7.2.2 d). During easy axis sweeps, the intensity of the 1.36 eV peak doesn't change until the critical field, at which point the peak disappears. Given that it appears only in samples with 3 or more layers in the presence of layered antiferromagnetic order, we hypothesize that it arise when parallel-aligned layers are coupled to each other through an intermediate anti-aligned layer, perhaps from next-nearest-neighbor interlayer exchange interactions. Furthermore, the linearly decreasing intensity of the peak during spin canting and sudden disappearance with layer flipping suggests that the corresponding electronic state scatters efficiently into a lower energy state in the absence of AFM order. This would imply that scattering between these two states at

zero field is spin-forbidden, thus preventing the higher energy state from scattering into the lower energy state and brightening its PL emission.

The behavior of the four layer is more complicated. The easy axis field sweep reveals an extra magnetic field transition through the magneto-PL, the first transition (0.15 T) occurring at approximately half the magnetic field of the second transition (0.31 T) (fig. 7.2.2 e). This behavior is consistent with layer-by-layer flipping. Since, at zero field, the four layer consists of two layers magnetically aligned in the **b** direction interleaved with two layers antialigned in the **-b** direction, the first transition may correspond to the flipping of one antialigned layer, resulting in half magnetization, and the second transition corresponding to the remaining antialigned layer flipping to give fully saturated magnetization. The PL spectrum in the half-magnetized state is largely a mixture of the peaks found at zero magnetization and those found at saturation, albeit with reduced intensity (fig. 7.2.2 f). If the magnetic response of the PL spectrum depended on net magnetization or any other global magnetic property, this would not be the case, as the half-magnetized configuration would be expected to give a unique and distinctive spectrum. Rather, this result suggests that the coupling between the magnetic order and PL depends on the interlayer configuration *local* to each individual layer, such that when a single layer in the four layer flips to produce half magnetization, reducing the number of AFM interlayer interfaces, the PL features which are signatures of the AFM order persist due to the remaining AFM interfaces.

The layer-by-layer flipping also gives us a chance to compare the PL spectra in the case of half magnetization brought about by the flip of a single layer versus the case of half magnetization resulting from spin canting. Based on bulk measurements[235], we expect the net magnetic moment along the **a** direction M_a to be at half the saturated value $M_{a,sat}/2$ at magnetic field along the **a** direction B_a equal to half the saturation field along that axis $B_{a,sat}/2$. Since the magnetic moments in the **b** direction cancel in the four layer, this means that half *net* magnetization $|\boldsymbol{M}_{sat}|/2$ occurs at $B_{a,sat}/2$. Comparison of the half-magnetization spectra along the **a** and **b** directions, unsurprisingly, shows that they are rather different (fig. 7.2.2 g). It is obvious that this should be the case *a priori* from the fact that no energy shift of the 1.36 eV peak occurs during easy axis field sweeps, whereas during intermediate and hard axis field sweeps, the energy changes continuously. This comparison nevertheless highlights these two distinct

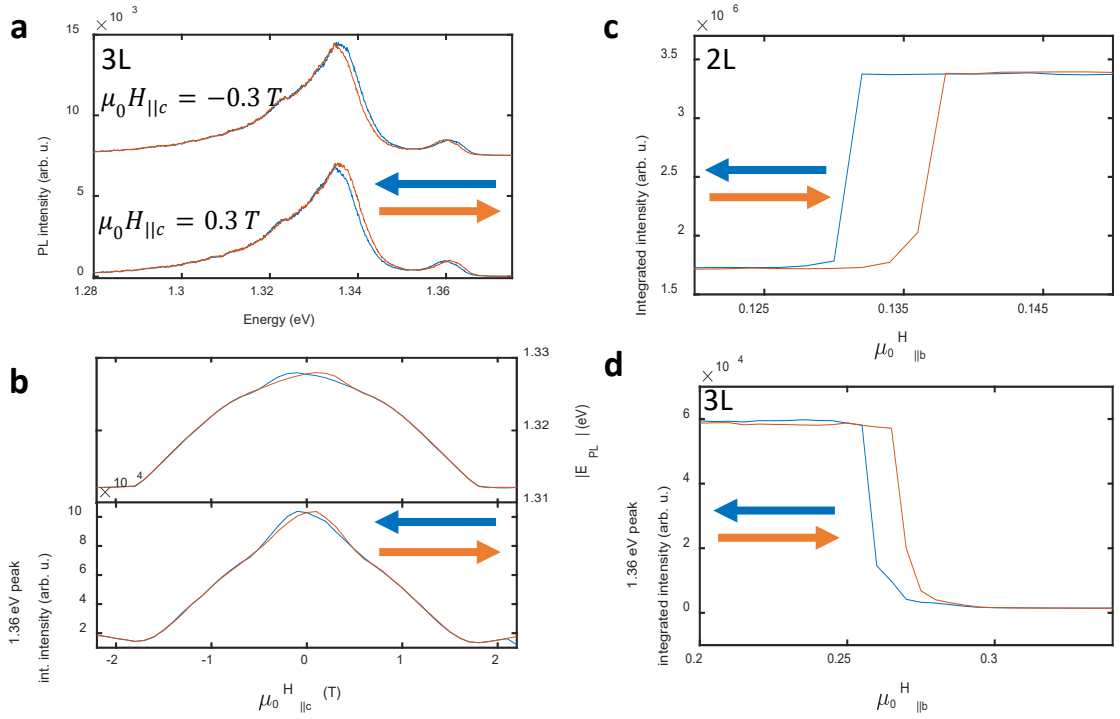

Figure 7.2.3 Hysteretic magnetic behavior observed through magneto-photoluminescence. **a** PL spectra of trilayer CrSBr in positive and negative magnetic fields (partial magnetization) along the hard axis for both directions of field sweep (indicated by colored arrows. The different sweep directions and field values constitute antisymmetric time reversal pairs. **b** Extracted PL center-of-mass energy (top) and peak intensity of 1.36 eV peak (bottom) during a bidirectional hard-axis field sweep, showing explicit hysteretic behavior. **c, d** Total integrated intensity and integrated intensity of 1.36 eV peak (respectively) of bilayer and trilayer CrSBr PL during easy-axis field sweeps, showing small hysteresis loops at the layer flip transition.

effects: intensity of a given PL peak depends on the *degree* of antiferromagnetic interlayer coupling or the number of antiferromagnetic interfaces, whether due to layer flipping or magnetization canting, while energy shifts seem to be governed by exclusively by canting behavior.

One unusual aspect of the hard axis magnetic field response is the appearance of antisymmetric (with respect to sweep direction) hysteresis observed in the shifting PL spectrum. This is most clearly seen when the field-dependent center of mass energy $E_{CoM}(B)$ or integrated intensity (fig. 7.2.3 a-b) are plotted, in which the data depart from one another for the two different sweep directions in an antisymmetric fashion at low fields, before once again overlapping at a field value somewhere below the saturating magnetic field. We speculate that

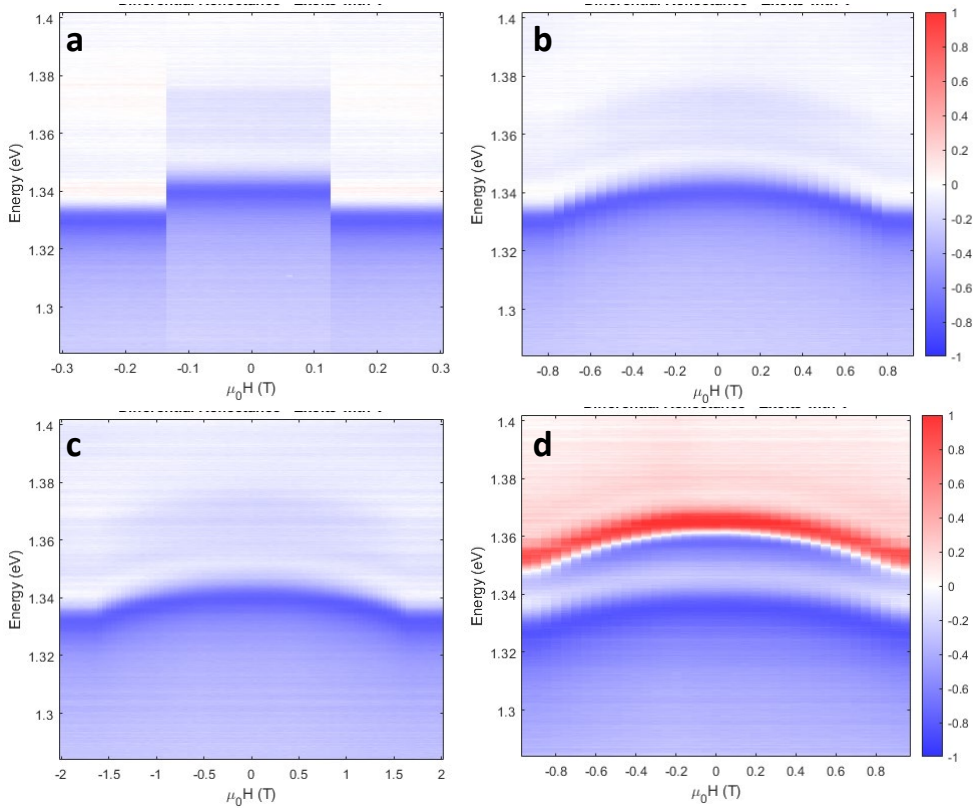

Figure 7.2.4 Magneto-reflectance spectroscopy. **a-c** Differential reflectance of bilayer CrSBr as a function of easy, intermediate, and hard axis magnetic field. **D** Differential reflectance of trilayer CrSBr as a function of intermediate axis magnetic field. Note that at no point do any resonance features appear or disappear, in contrast to the field-dependent PL spectrum of trilayer.

this might be a signature of the intermediate-axis spin-flop transition, in which the sample plane is slightly tilted, allowing coupling between the easy-axis crystal direction and the magnetic field vector nominally corresponding to the hard axis direction. Careful inspection of easy-axis sweeps of bilayer (fig. 7.2.3 c) and trilayer (fig. 7.2.3 d) reveal that the layer-flip transitions are slightly hysteretic as well, with coercive fields of a few mT.

The evolution of the differential reflectance spectrum as a function of magnetic field largely mirrors the behavior of the PL, highlighting the deep connection between the magnetic order and the optical transitions in CrSBr. The easy, intermediate, and hard axis field sweeps trace out the same qualitative behavior, with abrupt energy jumps visible across layer flips in easy axis field sweeps and gradual redshift in off-axis field sweeps (fig. 7.2.4). An important distinction, though, is that in intermediate and hard axis field sweeps, no reflectance resonances disappear

(unlike in the PL, where certain peaks diminish linearly with field). This further supports the hypothesis that the vanishing PL peaks arise from interlayer exchange rather than another effect like interlayer hybridization, as the exchange effect is purely excitonic.

Systematic analysis of the saturating fields recorded by the temperature-dependent magneto-PL or magneto-absorption can potentially provide an estimate of the transition temperature, similar to the analysis of previously reported CrSBr bulk transport measurements. By extracting the center-of-mass energy of the magneto-PL as a function of magnetic field, we can define the saturating fields for intermediate and hard axis sweeps by a peak in the second derivative, d^2E_{CoM}/dB^2. For easy axis sweeps, we define the saturating field by the centroid of the hysteresis loop corresponding to the layer flip transition to saturated magnetization (fig. 7.2.5 a). The extracted critical fields of trilayer as a function of temperature are plotted for the **a**, **b**, and **c** directions in figure 7.2.5 b. The **a** and **c** axis critical fields fit well to a linear model with an x-intercept of around 155-160 K. However, based on the previously reported field dependent transport measurements[235], we expect the linear fit to overestimate the critical fields as temperature approaches the transition temperature; thus the extracted x-intercepts overestimate the transition temperature. We can therefore conclude only that for thin exfoliated flakes, the critical temperature lies between our highest-measured temperature at which magnetic response was observed, 130 K, and the overestimate provided by linear extrapolation of the critical field data, 155-160 K, consistent with theoretical and experimental estimates in bulk.

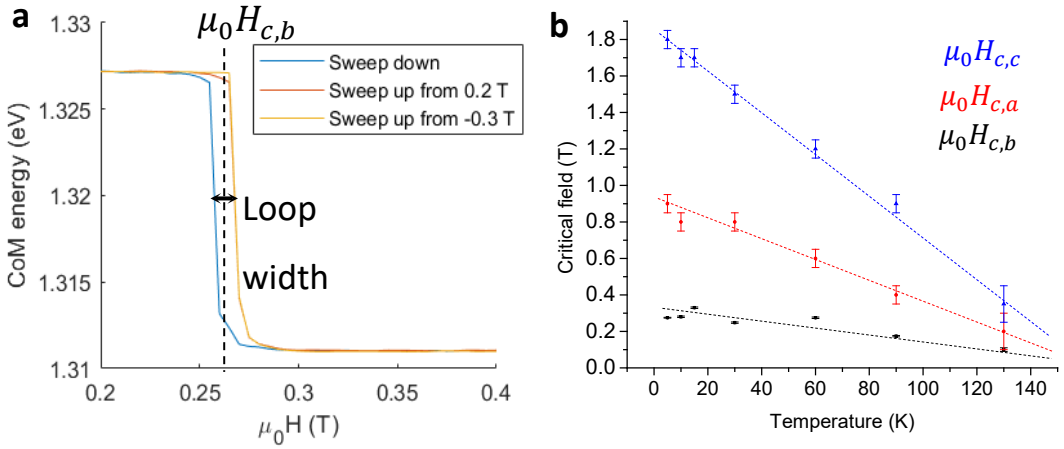

Figure 7.2.5 Critical field temperature dependence **a** Determination of the critical field $\mu_0 H_{c,b}$ along the easy axis, accounting for directional hysteresis. **b** Determined critical fields for magnetization along all three crystal directions. Straight lines are guides to the eye.

Adapted figures

Figures listed below have been adapted from the following publications, with all relevant and necessary rights to reproduce/adapt the figures granted by their respective copyright holders.

Figure 2.1.1 d adapted from ref.[206], courtesy of WILEY-VCH Verlag GmbH.

Figure 3.2.1 a adapted from ref.[11], courtesy of American Chemical Society.
Figure 3.3.1 a adapted from ref.[11], courtesy of American Chemical Society.
Figure 3.3.1 c adapted from ref.[67], courtesy of Springer Nature.
Figure 3.3.1 d adapted from ref.[68] , courtesy of Springer Nature.
Figure 3.3.2 a adapted from ref.[84], courtesy of Springer Nature.
Figure 3.3.2 b adapted from ref.[86], licensed under Creative Commons Attribution 4.0*.
Figure 3.3.2 c adapted from ref.[90], courtesy of Springer Nature.

Figure 4.4.1 a adapted from ref.[49], courtesy of American Chemical Society.
Figure 4.4.1 b-c adapted from ref.[118], licensed under Creative Commons Attribution 4.0*.
Figure 4.5.1 b-d adapted from ref.[49], courtesy of American Chemical Society.
Figure 4.6.1 a adapted from ref.[239], courtesy of American Physical Society.
Figure 4.6.1 b adapted from ref.[141], courtesy of American Physical Society.
Figure 4.6.1 c adapted from ref.[142], licensed under Creative Commons Attribution 4.0*.
Figure 4.6.3 a-c adapted from ref.[240], courtesy of American Physical Society.

Figure 5.1.1 e adapted from ref.[152], courtesy of Springer Nature.
Figure 5.1.2 a adapted from ref.[65], courtesy of AIP Publishing.
Figure 5.1.3 a adapted from ref.[20], courtesy of Springer Nature.
Figure 5.1.3 b-d adapted from ref.[241], courtesy of IOP Publishing.
Figure 5.1.3 e adapted from ref.[166], courtesy of AAAS.

Figure 6.1.1 a adapted from ref.[13], courtesy of Springer Nature.
Figure 6.1.1 b adapted from ref.[242], courtesy of American Chemical Society.
Figure 6.1.1 c-d adapted from ref.[188], courtesy of Springer Nature.
Figure 6.1.2 a-b adapted from ref.[13], courtesy of Springer Nature.
Figure 6.1.2 c-d adapted from ref.[35], courtesy of AAAS.
Figure 6.1.3 c adapted from ref.[201], courtesy of American Chemical Society.

Figure 7.1.1 b adapted from ref.[233], courtesy of X. Qian.
*License text can be found at http://creativecommons.org/licenses/by/4.0/

Bibliography

1. Bernal, J. D. & Bragg, W. *The Structure of Graphite. The Structure of Graphite*. *The Royal Society* **106**, (1924).

2. Novoselov, K. S. *et al.* Two-dimensional gas of massless Dirac fermions in graphene. *Nature* **438**, 197–200 (2005).

3. Lifshitz, E. M. The Theory of Molecular Attractive Forces between Sol ids. *J. Exp. Theor. Phys.* **29**, 94–110 (1955).

4. Pease, R. S. Crystal structure of boron nitride. *Nature* **165**, 722–723 (1950).

5. Goodenough, J. B. Spin-orbit-coupling effects in transition-metal compounds. *Phys. Rev.* **171**, 466–479 (1968).

6. Bromley, R. A. A semi-empirical tight-binding calculation of the band structure of MoS2. *Phys. Lett. A* **33**, 242–243 (1970).

7. Dillon, J. F., Kamimura, H. & Remeika, J. P. Magneto-optical properties of ferromagnetic chromium trihalides. *J. Phys. Chem. Solids* **27**, 1531–1549 (1966).

8. Novoselov, K. S. *et al.* Electric field in atomically thin carbon films. *Science (80-.).* **306**, 666–669 (2004).

9. Mottas, M. L. *et al.* Semimetal-to-semiconductor transition and charge-density-wave suppression in 1T-TiSe2-x Sx single crystals. *Phys. Rev. B* **99**, 155103 (2019).

10. Zhao, S. *et al.* Two-dimensional metallic NbS2: growth, optical identification and transport properties. *2D Mater.* **3**, 025027 (2016).

11. Splendiani, A. *et al.* Emerging photoluminescence in monolayer MoS2. *Nano Lett.* **10**, 1271–1275 (2010).

12. Zhang, K., Feng, Y., Wang, F., Yang, Z. & Wang, J. Two dimensional hexagonal boron nitride (2D-hBN): Synthesis, properties and applications. *Journal of Materials Chemistry C* **5**, 11992–12022 (2017).

13. Huang, B. *et al.* Layer-dependent ferromagnetism in a van der Waals crystal down to the monolayer limit. *Nature* **546**, 270–273 (2017).

14. Wang, H. *et al.* High-quality monolayer superconductor NbSe2 grown by chemical vapour deposition. *Nat. Commun.* **8**, 1–8 (2017).

15. Qian, X., Liu, J., Fu, L. & Li, J. Quantum spin hall effect in two - Dimensional transition metal dichalcogenides. *Science (80-.).* **346**, 1344–1347 (2014).

16. Deng, Y. *et al.* Quantum anomalous Hall effect in intrinsic magnetic topological insulator MnBi2Te4. *Science (80-.).* **367**, 895–900 (2020).

17. Du, L. *et al.* 2D proximate quantum spin liquid state in atomic-thin α-RuCl3. *2D Mater.* **6**, 015014 (2019).

18. Koma, A. Van der Waals epitaxy-a new epitaxial growth method for a highly lattice-mismatched system. *Thin Solid Films* **216**, 72–76 (1992).

19. Yankowitz, M. *et al.* Emergence of superlattice Dirac points in graphene on hexagonal boron nitride. *Nat. Phys.* **8**, 382–386 (2012).

20. Rivera, P. *et al.* Observation of long-lived interlayer excitons in monolayer MoSe2–WSe2 heterostructures. *Nat. Commun.* **6**, 6242 (2015).

21. Seyler, K. L. *et al.* Signatures of moiré-trapped valley excitons in $MoSe_2/WSe_2$ heterobilayers. *Nature* **567**, 66–70 (2019).

22. Jin, C. *et al.* Observation of moiré excitons in WSe_2/WS_2 heterostructure superlattices. *Nature* **567**, 76–80 (2019).

23. Zhu, L. & Yang, L. Quasiparticle energies and excitonic effects of chromium trichloride: From two dimensions to bulk. *Phys. Rev. B* **101**, 245401 (2020).

24. Shinagawa, K., Sato, H., Ross, H. J., McAven, L. F. & Butler, P. H. Charge-transfer transitions in chromium trihalides. *J. Phys. Condens. Matter* **8**, 8457–8463 (1996).

25. Huang, Y. *et al.* Universal mechanical exfoliation of large-area 2D crystals. *Nat. Commun.*

11, 1–9 (2020).

26. Jayasena, B. & Melkote, S. N. An Investigation of PDMS Stamp Assisted Mechanical Exfoliation of Large Area Graphene. in *Procedia Manufacturing* **1**, 840–853 (Elsevier B.V., 2015).

27. Li, X. *et al.* Stretchable and highly sensitive graphene-on-polymer strain sensors. *Sci. Rep.* **2**, 1–6 (2012).

28. Li, Z. *et al.* Efficient strain modulation of 2D materials via polymer encapsulation. *Nat. Commun.* **11**, 1–8 (2020).

29. Huang, Y. *et al.* Reliable Exfoliation of Large-Area High-Quality Flakes of Graphene and Other Two-Dimensional Materials. *ACS Nano* **9**, 10612–10620 (2015).

30. Yamashita, T. *et al.* Impact of Surface Treatment of SiO2/Si Substrate on Mechanically Exfoliated Graphene. in (2015). doi:10.7567/ssdm.2010.j-5-3

31. Wang, Y., Zhou, V., Xie, Y., Zheng, X. & Feng, P. X.-L. Optical contrast signatures of hexagonal boron nitride on a device platform. *Opt. Mater. Express* **9**, 1223 (2019).

32. Etzler, F. M. & Drelich, J. Atomic Force Microscopy for Characterization of Surfaces, Particles, and Their Interactions. in *Developments in Surface Contamination and Cleaning: Detection, Characterization, and Analysis of Contaminants* 307–331 (Elsevier Inc., 2012). doi:10.1016/B978-1-4377-7883-0.00006-7

33. Zhao, Y. *et al.* Interlayer breathing and shear modes in few-trilayer MoS2 and WSe2. *Nano Lett.* **13**, 1007–1015 (2013).

34. Lui, C. H. *et al.* Observation of layer-breathing mode vibrations in few-layer graphene through combination raman scattering. *Nano Lett.* **12**, 5539–5544 (2012).

35. Song, T. *et al.* Giant tunneling magnetoresistance in spin-filter van der Waals heterostructures. *Science* **360**, 1214–1218 (2018).

36. Ranjan, A. *et al.* Mechanism of soft and hard breakdown in hexagonal boron nitride 2D

dielectrics. in *IEEE International Reliability Physics Symposium Proceedings* **2018**-**March**, 4A.11-4A.16 (Institute of Electrical and Electronics Engineers Inc., 2018).

37. Hattori, Y., Taniguchi, T., Watanabe, K. & Nagashio, K. Layer-by-layer dielectric breakdown of hexagonal boron nitride. *ACS Nano* **9**, 916–921 (2015).

38. Deng, J. X. *et al.* Optical properties of hexagonal boron nitride thin films deposited by radio frequency bias magnetron sputtering. *Chinese Phys. B* **18**, 4013–4018 (2009).

39. Zhang, Y., Small, J. P., Pontius, W. V. & Kim, P. Fabrication and electric-field-dependent transport measurements of mesoscopic graphite devices. *Appl. Phys. Lett.* **86**, 1–3 (2005).

40. Craciun, M. F. *et al.* Trilayer graphene is a semimetal with a gate-tunable band overlap. *Nat. Nanotechnol.* **4**, 383–388 (2009).

41. Oostinga, J. B., Heersche, H. B., Liu, X., Morpurgo, A. F. & Vandersypen, L. M. K. Gate-induced insulating state in bilayer graphene devices. *Nat. Mater.* **7**, 151–157 (2008).

42. Zhang, Y. *et al.* Direct observation of a widely tunable bandgap in bilayer graphene. *Nature* **459**, 820–823 (2009).

43. Nair, R. R. *et al.* Fine structure constant defines visual transparency of graphene. *Science (80-.).* **320**, 1308 (2008).

44. Dawlaty, J. M. *et al.* Measurement of the optical absorption spectra of epitaxial graphene from terahertz to visible. *Appl. Phys. Lett.* **93**, 131905 (2008).

45. Yakubovsky, D. I. *et al.* Thin films, optical properties; (310.1860) Deposition and fabrication; (160.4670) Optical materials. (2017). doi:10.1364/OE.25.025574

46. Sambles, J. R., Elsom, K. C. & Jarvis, D. J. The electrical resistivity of gold films. *Philos. Trans. R. Soc. London. Ser. A, Math. Phys. Sci.* **304**, 365–396 (1982).

47. Frisenda, R. *et al.* Recent progress in the assembly of nanodevices and van der Waals heterostructures by deterministic placement of 2D materials. *Chemical Society Reviews* **47**, 53–68 (2018).

48. Zomer, P. J., Guimarães, M. H. D., Brant, J. C., Tombros, N. & Van Wees, B. J. Fast pick up technique for high quality heterostructures of bilayer graphene and hexagonal boron nitride. *Appl. Phys. Lett.* **105**, 013101 (2014).

49. Stier, A. V., Wilson, N. P., Clark, G., Xu, X. & Crooker, S. A. Probing the Influence of Dielectric Environment on Excitons in Monolayer WSe_2 : Insight from High Magnetic Fields. *Nano Lett.* **16**, 7054–7060 (2016).

50. Kinoshita, K. *et al.* Dry release transfer of graphene and few-layer h-BN by utilizing thermoplasticity of polypropylene carbonate. *npj 2D Mater. Appl.* **3**, 22 (2019).

51. Ribeiro-Soares, J. *et al.* Second Harmonic Generation in WSe_2. *2D Mater.* **2**, 045015 (2015).

52. Wang, G. *et al.* Giant Enhancement of the Optical Second-Harmonic Emission of WSe2 Monolayers by Laser Excitation at Exciton Resonances. *Phys. Rev. Lett.* **114**, (2015).

53. Kumar, N. *et al.* Second harmonic microscopy of monolayer MoS2. *Phys. Rev. B - Condens. Matter Mater. Phys.* **87**, 161403 (2013).

54. Malard, L. M., Alencar, T. V., Barboza, A. P. M., Mak, K. F. & De Paula, A. M. Observation of intense second harmonic generation from MoS2 atomic crystals. *Phys. Rev. B - Condens. Matter Mater. Phys.* **87**, 201401 (2013).

55. Wilson, P. T., Jiang, Y., Aktsipetrov, O. A., Mishina, E. D. & Downer, M. C. Frequency-domain interferometric second-harmonic spectroscopy. *Opt. Lett.* **24**, 496 (1999).

56. Kim, K. *et al.* van der Waals Heterostructures with High Accuracy Rotational Alignment. *Nano Lett.* **16**, 1989–1995 (2016).

57. Fors, H. Elements in the Melting Pot: Merging Chemistry, Assaying, and Natural History, Ca. 1730-60. *Osiris* **29**, 230–44 (2014).

58. S., A. The Chemical Essays of Charles-William Scheele. *Nature* **65**, 3–4 (1901).

59. Gibb, B. C. Hard-luck Scheele. *Nat. Chem.* **7**, 855–856 (2015).

60. Winer, W. O. Molybdenum disulfide as a lubricant: A review of the fundamental knowledge. *Wear* **10**, 422–452 (1967).

61. MOAZAMI-GOUDARZI, M. & NEMATI, A. Tribological behavior of self lubricating Cu/MoS2 composites fabricated by powder metallurgy. *Trans. Nonferrous Met. Soc. China (English Ed.* **28**, 946–956 (2018).

62. Jones, G. Thickness dependence of the ground-state exciton energy in WSe2. *Physical Review B* **4**, 2069–2071 (1971).

63. Wilson, J. A. & Yoffe, A. D. The transition metal dichalcogenides discussion and interpretation of the observed optical, electrical and structural properties. *Adv. Phys.* **18**, 193–335 (1969).

64. Bronger, W. The Layered Structures of Ternary Chalcogenides with Alkali and Transition Metals. in *Crystallography and Crystal Chemistry of Materials with Layered Structures* 93–125 (Springer Netherlands, 1976). doi:10.1007/978-94-010-1433-5_3

65. Kang, J., Tongay, S., Zhou, J., Li, J. & Wu, J. Band offsets and heterostructures of two-dimensional semiconductors. *Appl. Phys. Lett.* **102**, 012111 (2013).

66. Xiao, D., Liu, G. Bin, Feng, W., Xu, X. & Yao, W. Coupled spin and valley physics in monolayers of MoS 2 and other group-VI dichalcogenides. *Phys. Rev. Lett.* **108**, 196802 (2012).

67. Mak, K. F., He, K., Shan, J. & Heinz, T. F. Control of valley polarization in monolayer MoS2 by optical helicity. *Nat. Nanotechnol.* **7**, 494–498 (2012).

68. Jones, A. M. *et al.* Optical generation of excitonic valley coherence in monolayer WSe 2. *Nat. Nanotechnol.* **8**, 634–638 (2013).

69. Goryca, M., Wilson, N. P., Dey, P., Xu, X. & Crooker, S. A. Detection of thermodynamic “valley noise” in monolayer semiconductors: Access to intrinsic valley relaxation time scales. *Sci. Adv.* **5**, eaau4899 (2019).

70. Liu, G. Bin, Xiao, D., Yao, Y., Xu, X. & Yao, W. Electronic structures and theoretical

modelling of two-dimensional group-VIB transition metal dichalcogenides. *Chemical Society Reviews* **44**, 2643–2663 (2015).

71. Schaibley, J. R. *et al.* Valleytronics in 2D materials. *Nat. Rev. Mater.* **1**, (2016).

72. Yao, W., Xiao, D. & Niu, Q. Valley-dependent optoelectronics from inversion symmetry breaking. *Phys. Rev. B - Condens. Matter Mater. Phys.* **77**, 235406 (2008).

73. Xiao, D., Yao, W. & Niu, Q. Valley-contrasting physics in graphene: Magnetic moment and topological transport. *Phys. Rev. Lett.* **99**, 236809 (2007).

74. You, J. S., Fang, S., Xu, S. Y., Kaxiras, E. & Low, T. Berry curvature dipole current in the transition metal dichalcogenides family. *Phys. Rev. B* **98**, 121109 (2018).

75. Zhou, J., Shan, W. Y., Yao, W. & Xiao, D. Berry Phase Modification to the Energy Spectrum of Excitons. *Phys. Rev. Lett.* **115**, 166803 (2015).

76. Aivazian, G. *et al.* Magnetic control of valley pseudospin in monolayer WSe 2. *Nat. Phys.* **11**, 148–152 (2015).

77. Feng, W. *et al.* Intrinsic spin Hall effect in monolayers of group-VI dichalcogenides: A first-principles study. *Phys. Rev. B - Condens. Matter Mater. Phys.* **86**, 165108 (2012).

78. Selbmann, P. E., Gulia, M., Rossie, F., Molinari, E. & Lugli, P. Dynamics of Exciton Formation and Relaxation in Semiconductors. in *Hot Carriers in Semiconductors* 19–22 (Springer US, 1996). doi:10.1007/978-1-4613-0401-2_5

79. Fox, M. *Optical Properties of Solids*. (OUP Oxford).

80. Zhang, X. X., You, Y., Zhao, S. Y. F. & Heinz, T. F. Experimental Evidence for Dark Excitons in Monolayer WSe2. *Phys. Rev. Lett.* (2015). doi:10.1103/PhysRevLett.115.257403

81. Zhang, X. X. *et al.* Magnetic brightening and control of dark excitons in monolayer WSe 2. *Nat. Nanotechnol.* **12**, 883–888 (2017).

82. Zeng, H. *et al.* Optical signature of symmetry variations and spin-valley coupling in atomically thin tungsten dichalcogenides. *Sci. Rep.* **3**, 1–5 (2013).

83. Mak, K. F. *et al.* Tightly bound trions in monolayer MoS 2. *Nat. Mater.* **12**, 207–211 (2013).

84. Ross, J. S. *et al.* Electrically tunable excitonic light-emitting diodes based on monolayer WSe2 p-n junctions. *Nat. Nanotechnol.* **9**, 268–272 (2014).

85. Nagler, P. *et al.* Interlayer Excitons in Transition-Metal Dichalcogenide Heterobilayers. *Phys. Status Solidi Basic Res.* **256**, (2019).

86. He, M. *et al.* Valley phonons and exciton complexes in a monolayer semiconductor. *Nat. Commun.* **11**, 1–7 (2020).

87. Haldar, S., Vovusha, H., Yadav, M. K., Eriksson, O. & Sanyal, B. Systematic study of structural, electronic, and optical properties of atomic-scale defects in the two-dimensional transition metal dichalcogenides MX2 (M = Mo, W; X = S, Se, Te). *Phys. Rev. B - Condens. Matter Mater. Phys.* **92**, 235408 (2015).

88. Clark, G. *et al.* Single defect light-emitting diode in a van der Waals heterostructure. *Nano Lett.* **16**, 3944–3948 (2016).

89. Jeong, T. Y. *et al.* Spectroscopic studies of atomic defects and bandgap renormalization in semiconducting monolayer transition metal dichalcogenides. *Nat. Commun.* **10**, 1–10 (2019).

90. He, Y. M. *et al.* Single quantum emitters in monolayer semiconductors. *Nat. Nanotechnol.* **10**, 497–502 (2015).

91. Plechinger, G. *et al.* Trion fine structure and coupled spin-valley dynamics in monolayer tungsten disulfide. *Nat. Commun.* **7**, 1–9 (2016).

92. Gao, S., Liang, Y., Spataru, C. D. & Yang, L. Dynamical Excitonic Effects in Doped Two-Dimensional Semiconductors. doi:10.1021/acs.nanolett.6b02118

93. Quattropani, A. & Forney, J. J. Theory of excitonic molecules. *Nuovo Cim. B Ser. 11* **39**, 569–578 (1977).

94. Ivanov, A. L., Haug, H. & Keldysh, L. V. Optics of excitonic molecules in semiconductors and semiconductor microstructures. *Physics Report* **296**, 237–336 (1998).

95. Goodenough, J. B. *Magnetism And The Chemical Bond*. (Interscience Publishers, 1963).

96. Pikus, G. & Bir, G. Exchange Interaction in Excitons in Semiconductors. *Sov. J. Exp. Theor. Phys.* **33**, 108 (1971).

97. Guo, L. *et al.* Exchange-driven intravalley mixing of excitons in monolayer transition metal dichalcogenides. *Nat. Phys.* **15**, 228–232 (2019).

98. Kühn, M. & Kliem, H. Microscopic versus macroscopic calculation of dielectric nanospheres. *J. Phys. Conf. Ser.* **142**, (2008).

99. Onodera, Y. Microscopic Dielectric Constant in Insulators. *Prog. Theor. Phys.* **49**, 37–45 (1973).

100. La Rocca, G. . Wannier–Mott Excitons in Semiconductors. in **31**, 97–128 (Academic Press, 2003).

101. Takeno, S. Theory of Frenkel Excitons Using a Two-Level-Atom Model. in *Energy and Charge Transfer in Organic Semiconductors* 69–73 (Springer US, 1974). doi:10.1007/978-1-4684-2109-5_10

102. Vos, M. & Grande, P. L. Modelling the contribution of semi-core electrons to the dielectric function. *J. Phys. Chem. Solids* **124**, 242–249 (2019).

103. Kelly, M. J. & Nicholas, R. J. The physics of quantum well structures. *Reports Prog. Phys.* **48**, 1699 (1985).

104. Fox, M. & Ispasoiu, R. Quantum wells, superlattices, and band-gap engineering. in *Springer Handbooks* 1 (Springer, 2017). doi:10.1007/978-3-319-48933-9_40

105. Ando, T., Fowler, A. B. & Stern, F. Electronic properties of two-dimensional systems. *Rev. Mod. Phys.* **54**, 437–672 (1982).

106. Van Tuan, D., Yang, M. & Dery, H. Coulomb interaction in monolayer transition-metal

dichalcogenides. *Phys. Rev. B* **98**, 125308 (2018).

107. Berkelbach, T. C., Hybertsen, M. S. & Reichman, D. R. Theory of neutral and charged excitons in monolayer transition metal dichalcogenides. *Phys. Rev. B - Condens. Matter Mater. Phys.* **88**, 045318 (2013).

108. Sakurai, J. J. & Napolitano, J. *Modern Quantum Mechanics*. (Addison-Wesley, 2011).

109. Grechikhin, L. I. & El'yashevich, M. A. Use of the quadratic Stark effect to determine the concentration of charged particles in a plasma from the broadening of lithium and sodium lines. *J. Appl. Spectrosc.* **3**, 145–150 (1965).

110. Nolting, W. & Ramakanth, A. *Quantum Theory of Magnetism*. (Springer-Verlag Berlin Heidelberg, 2009).

111. Soule, D. E., McClure, J. W. & Smith, L. B. Study of the Shubnikov-de Haas effect. Determination of the fermi surfaces in graphite. *Phys. Rev.* **134**, A453 (1964).

112. Lerner, L. S. Shubnikov-de Haas effect in bismuth. *Phys. Rev.* **127**, 1480–1492 (1962).

113. Frederikse, H. P. R., Hosler, W. R., Thurber, W. R., Babiskin, J. & Siebenmann, P. G. Shubnikov-de haas effect in SrTiO3. *Phys. Rev.* **158**, 775–778 (1967).

114. Shaw, R. W. & Hill, D. E. Shubnikov-de haas oscillations in n-type GaAs. *Phys. Rev. B* **1**, 658–662 (1970).

115. Klitzing, K. V., Dorda, G. & Pepper, M. New method for high-accuracy determination of the fine-structure constant based on quantized hall resistance. *Phys. Rev. Lett.* **45**, 494–497 (1980).

116. Wang, Z., Shan, J. & Mak, K. F. Valley- and spin-polarized Landau levels in monolayer WSe_2. *Nat. Nanotechnol.* | **12**, (2017).

117. Kylänpää, I. & Komsa, H. P. Binding energies of exciton complexes in transition metal dichalcogenide monolayers and effect of dielectric environment. *Phys. Rev. B - Condens. Matter Mater. Phys.* **92**, 205418 (2015).

118. Stier, A. V., McCreary, K. M., Jonker, B. T., Kono, J. & Crooker, S. A. Exciton diamagnetic shifts and valley Zeeman effects in monolayer WS2 and MoS2 to 65 Tesla. *Nat. Commun.* **7**, 1–8 (2016).

119. Miura, N. *Physics of Semiconductors in High Magnetic Fields*. (Oxford University Press, 2008).

120. Bugajski, M., Kuszko, W. & Regiński, K. Diamagnetic shift of exciton energy levels in GaAs-Ga1-xAlxAs quantum wells. *Solid State Commun.* **60**, 669–673 (1986).

121. Duque, C. A., de Dios-Leyva, M. & Oliveira, L. E. Exciton diamagnetic shift in GaAs / Ga1 - x Alx As quantum wells under in-plane magnetic fields. *Microelectronics J.* **39**, 407–410 (2008).

122. Kulakovskfi, V. D., Malyavkin, A. V & Timofeev, V. B. *Diamagnetism of excitons and excitonic molecules in silicon*. *Phys. JETP* **50**, (1979).

123. Stpnicki, P., Pitka, B., Morier-Genoud, F., Deveaud, B. & Matuszewski, M. Analytical method for determining quantum well exciton properties in a magnetic field. *Phys. Rev. B - Condens. Matter Mater. Phys.* **91**, 195302 (2015).

124. Lee, K. S., Lee, C. D., Kim, Y. & Kyu Noh, S. Dependence of the heavy-hole exciton reduced mass on quantum-well size in InGaAs/GaAs heterostructures. *Solid State Commun.* **128**, 177–180 (2003).

125. Fowler, C. M., Garn, W. B. & Caird, R. S. Production of very high magnetic fields by implosion. *J. Appl. Phys.* **31**, 588–594 (1960).

126. Werst, M. D., Ingram, S. K., Wehrlen, D. J. & Weldon, W. F. High Magnetic Field Generation Using Single-Turn Coils. *IEEE Trans. Magn.* **30**, 2550–2553 (1994).

127. Portugall, O., Puhlmann, N. & Von Ortenberg, M. *Megagauss magnetic field generation in single-turn coils: new frontiers for scientific experiments*. *J. Phys. D: Appl. Phys* **32**, (1999).

128. Matula, R. A. Electrical resistivity of copper, gold, palladium, and silver. *J. Phys. Chem.*

Ref. Data **8**, 1147–1298 (1979).

129. Zafar, A. *et al.* Probing the intrinsic optical quality of CVD grown MoS2. *Nano Res.* **10**, 1608–1617 (2017).

130. Zhang, X. *et al.* Defect-Controlled Nucleation and Orientation of WSe 2 on hBN: A Route to Single-Crystal Epitaxial Monolayers. *ACS Nano* **13**, 3341–3352 (2019).

131. Fang, L. *et al.* Quick Optical Identification of the Defect Formation in Monolayer WSe2 for Growth Optimization. *Nanoscale Res. Lett.* **14**, 1–10 (2019).

132. Cadiz, F. *et al.* Excitonic linewidth approaching the homogeneous limit in MoS2-based van der Waals heterostructures. *Phys. Rev. X* **7**, (2017).

133. Moody, G. *et al.* Intrinsic homogeneous linewidth and broadening mechanisms of excitons in monolayer transition metal dichalcogenides. *Nat. Commun.* **6**, 1–6 (2015).

134. Malitson, I. H. Interspecimen Comparison of the Refractive Index of Fused Silica*,†. *J. Opt. Soc. Am.* **55**, 1205 (1965).

135. Geick, R., Perry, C. H. & Rupprecht, G. Normal modes in hexagonal boron nitride. *Phys. Rev.* **146**, 543–547 (1966).

136. Zhang, X., Qiu, J., Li, X., Zhao, J. & Liu, L. Complex refractive indices measurements of polymers in visible and near-infrared bands. *Appl. Opt.* **59**, 2337 (2020).

137. Wilson, N. R. *et al.* Determination of band offsets, hybridization, and exciton binding in 2D semiconductor heterostructures. *Sci. Adv.* **3**, (2017).

138. Rasmussen, F. A. & Thygesen, K. S. Computational 2D Materials Database: Electronic Structure of Transition-Metal Dichalcogenides and Oxides. (2015). doi:10.1021/acs.jpcc.5b02950

139. Müller-Kirsten, H. J. W. & Bose, S. K. Solution of the wave equation for the logarithmic potential with application to particle spectroscopy. *J. Math. Phys.* **20**, 2471–2480 (1979).

140. Roy, A. K. Calculation of the bound states of power-law and logarithmic potentials

through a generalized pseudospectral method. *J. Phys. G Nucl. Part. Phys.* **30**, 269–278 (2004).

141. Chernikov, A. *et al.* Exciton binding energy and nonhydrogenic Rydberg series in monolayer WS2. *Phys. Rev. Lett.* **113**, 076802 (2014).

142. Manca, M. *et al.* Enabling valley selective exciton scattering in monolayer WSe 2 through upconversion. *Nat. Commun.* **8**, 1–7 (2017).

143. Chow, C. M. *et al.* Unusual Exciton-Phonon Interactions at van der Waals Engineered Interfaces. *Nano Lett.* **17**, 1194–1199 (2017).

144. Amani, M. *et al.* Near-unity photoluminescence quantum yield in MoS2. *Science (80-.).* **350**, 1065–1068 (2015).

145. Gay, J. G. Screening of excitons in semiconductors. *Phys. Rev. B* **4**, 2567–2575 (1971).

146. Zhu, H. *et al.* Observation of chiral phonons. *Science (80-.).* **359**, 579–582 (2018).

147. Austin, E. J. & Jaros, M. *Carrier lifetimes and localisation in coupled GaAs-GaAlAs quantum wells in high electric fields*. *J. Phys. C: Solid State Phys* **19**, (1986).

148. Bayer, M., Timofeev, V. B., Faller, F., Gutbrod, T. & Forchel, A. *Direct and indirect excitons in coupled GaAs/Al 0.30 Ga 0.70 As double quantum wells separated by AlAs barriers*. (1996).

149. Ishibashi, A., Mori, Y., Itabashi, M. & Watanabe, N. Optical properties of (AlAs)n(GaAs)n superlattices grown by metalorganic chemical vapor deposition. *J. Appl. Phys.* **58**, 2691–2695 (1985).

150. Chen, Y. J., Koteles, E. S., Elman, B. S. & Armiento, C. A. Effect of electric fields on excitons in a coupled double-quantum-well structure. *Phys. Rev. B* **36**, 4562–4565 (1987).

151. Charbonneau, S., Thewalt, M. L. W., Koteles, E. S. & Elman, B. Transformation of spatially direct to spatially indirect excitons in coupled double quantum wells. *Phys. Rev. B* **38**, 6287–6290 (1988).

152. Larionov, A. V., Timofeev, V. B., Hvam, J. & Soerensen, K. Interwell excitons in GaAs/AlGaAs double quantum wells and their collective properties. *J. Exp. Theor. Phys.* **90**, 1093–1104 (2000).

153. Campman, K. L. & Gossard, A. C. Photoluminescence kinetics of indirect excitons in (formula presented) coupled quantum wells. *Phys. Rev. B - Condens. Matter Mater. Phys.* **59**, 1625–1628 (1999).

154. Sivalertporn, K., Mouchliadis, L., Ivanov, A. L., Philp, R. & Muljarov, E. A. Direct and indirect excitons in semiconductor coupled quantum wells in an applied electric field. *Phys. Rev. B - Condens. Matter Mater. Phys.* **85**, 45207 (2012).

155. Hammack, A. T. *et al.* Excitons in electrostatic traps. *J. Appl. Phys.* **99**, 066104 (2006).

156. Remeika, M. *et al.* Localization-Delocalization Transition of Indirect Excitons in Lateral Electrostatic Lattices. *Phys. Rev. Lett.* **102**, 186803 (2009).

157. Remeika, M., Fogler, M. M., Butov, L. V, Hanson, M. & Gossard, A. C. Two-dimensional electrostatic lattices for indirect excitons. (2012). doi:10.1063/1.3682302

158. Remeika, M. *et al.* Measurement of exciton correlations using electrostatic lattices. *Phys. Rev. B* **92**, 115311 (2015).

159. Fogler, M. M., Butov, L. V. & Novoselov, K. S. High-temperature superfluidity with indirect excitons in van der Waals heterostructures. *Nat. Commun.* **5**, 1–5 (2014).

160. Hong, X. *et al.* Ultrafast charge transfer in atomically thin MoS2/WS2 heterostructures. *Nat. Nanotechnol.* **9**, 682–686 (2014).

161. Palummo, M., Bernardi, M. & Grossman, J. C. Exciton radiative lifetimes in two-dimensional transition metal dichalcogenides. *Nano Lett.* **15**, 2794–2800 (2015).

162. Ehrenreich, H. Band structure and electron transport of GaAs. *Phys. Rev.* **120**, 1951–1963 (1960).

163. Zhu, H. *et al.* Interfacial Charge Transfer Circumventing Momentum Mismatch at Two-

Dimensional van der Waals Heterojunctions. *Nano Lett.* **17**, 3591–3598 (2017).

164. Song, Z. *et al.* Interlayer coupling in two-dimensional semiconductor materials. *Semicond. Sci. Technol.* **34**, 093001 (2019).

165. Ruiz-Tijerina, D. A. & Fal'Ko, V. I. Interlayer hybridization and moiré superlattice minibands for electrons and excitons in heterobilayers of transition-metal dichalcogenides. *Phys. Rev. B* **99**, 125424 (2019).

166. Rivera, P. *et al.* Valley-polarized exciton dynamics in a 2D semiconductor heterostructure. *Science (80-.).* **351**, 688–691 (2016).

167. Jauregui, L. A. *et al.* Electrical control of interlayer exciton dynamics in atomically thin heterostructures. *Science (80-.).* **366**, 870–875 (2019).

168. Jin, C. *et al.* Ultrafast dynamics in van der Waals heterostructures. *Nature Nanotechnology* **13**, 994–1003 (2018).

169. Kim, J. *et al.* Observation of ultralong valley lifetime in WSe2/MoS2 heterostructures. *Sci. Adv.* **3**, e1700518 (2017).

170. Fox, A. M., Miller, D. A. B., Livescu, G., Cunningham, J. E. & Jan, W. Y. Excitonic effects in coupled quantum wells. *Phys. Rev. B* **44**, 6231–6242 (1991).

171. Sivalertporn, K. Effect of barrier width on the exciton states in coupled quantum wells in an applied electric field. *Physics Letters, Section A: General, Atomic and Solid State Physics* **380**, 1990–1994 (2016).

172. McGuire, M. A., Dixit, H., Cooper, V. R. & Sales, B. C. Coupling of crystal structure and magnetism in the layered, ferromagnetic insulator cri3. *Chem. Mater.* **27**, 612–620 (2015).

173. Duine, R. A., Lee, K. J., Parkin, S. S. P. & Stiles, M. D. Synthetic antiferromagnetic spintronics. *Nature Physics* **14**, 217–219 (2018).

174. Lin, C. Y., Yang, S. W., Ou, K. L. & Jones, B. A. Activated layered magnetism from bulk TiN.

Phys. Rev. Mater. **3**, 124412 (2019).

175. Ruderman, M. A. & Kittel, C. Indirect exchange coupling of nuclear magnetic moments by conduction electrons. *Phys. Rev.* **96**, 99–102 (1954).

176. Kasuya, T. A Theory of Metallic Ferro- and Antiferromagnetism on Zener's Model. *Prog. Theor. Phys.* **16**, 45–57 (1956).

177. Yosida, K. Magnetic properties of Cu-Mn alloys. *Phys. Rev.* **106**, 893–898 (1957).

178. Baibich, M. N. *et al.* Giant magnetoresistance of (001)Fe/(001)Cr magnetic superlattices. *Phys. Rev. Lett.* **61**, 2472–2475 (1988).

179. Binasch, G., Grünberg, P., Saurenbach, F. & Zinn, W. Enhanced magnetoresistance in layered magnetic structures with antiferromagnetic interlayer exchange. *Phys. Rev. B* **39**, 4828–4830 (1989).

180. Fernando, G. W. Chapter 1 GMR in Metallic Multilayers - A Simple Picture. in *Handbook of Metal Physics* **4**, 1–32 (Elsevier, 2008).

181. Mao, S. *et al.* Commercial TMR heads for hard disk drives: Characterization and extendibility at 300 Gbit/in2. in *IEEE Transactions on Magnetics* **42**, 97–102 (2006).

182. Meiklejohn, W. H. & Bean, C. P. New magnetic anisotropy. *Phys. Rev.* **105**, 904–913 (1957).

183. Nogués, J. & Schuller, I. K. Exchange bias. *J. Magn. Magn. Mater.* **192**, 203–232 (1999).

184. Yi, S. S. & Kuech, T. F. Selective Area Epitaxy on Structures and Surfaces. in *Encyclopedia of Materials: Science and Technology* 8295–8299 (Elsevier, 2001). doi:10.1016/b0-08-043152-6/01484-4

185. Dillon, J. F. Ferromagnetic Resonance in CrBr3. in *Proceedings of the Seventh Conference on Magnetism and Magnetic Materials* 1191–1192 (Springer US, 1962). doi:10.1007/978-1-4899-6391-8_64

186. Kim, M. *et al.* Micromagnetometry of two-dimensional ferromagnets. *Nat. Electron.* **2**,

457–463 (2019).

187. Wang, H., Eyert, V. & Schwingenschlögl, U. Electronic structure and magnetic ordering of the semiconducting chromium trihalides CrCl3, CrBr3, and CrI3. *J. Phys. Condens. Matter* **23**, (2011).

188. Seyler, K. L. *et al.* Ligand-field helical luminescence in a 2D ferromagnetic insulator. *Nat. Phys.* **14**, 277–281 (2018).

189. Zhang, W. B., Qu, Q., Zhu, P. & Lam, C. H. Robust intrinsic ferromagnetism and half semiconductivity in stable two-dimensional single-layer chromium trihalides. *J. Mater. Chem. C* **3**, 12457–12468 (2015).

190. Gibertini, M., Koperski, M., Morpurgo, A. F. & Novoselov, K. S. Magnetic 2D materials and heterostructures. *Nature Nanotechnology* **14**, 408–419 (2019).

191. Goodenough, J. B. Theory of the role of covalence in the perovskite-type manganites [La,M(II)]MnO3. *Phys. Rev.* **100**, 564–573 (1955).

192. Kanamori, J. Superexchange interaction and symmetry properties of electron orbitals. *J. Phys. Chem. Solids* **10**, 87–98 (1959).

193. Anderson, P. W. Antiferromagnetism. Theory of superexchange interaction. *Phys. Rev.* **79**, 350–356 (1950).

194. and, H. W. & Güdel*, H. U. Quantitative Interpretation of the Goodenough−Kanamori Rules: A Critical Analysis. (1997). doi:10.1021/IC961502+

195. Tong, Q., Liu, F., Xiao, J. & Yao, W. Skyrmions in the Moiré of van der Waals 2D Magnets. *Nano Lett.* **18**, 7194–7199 (2018).

196. Matsuda, T. *et al.* Observation of a Devil's Staircase in the Novel Spin-Valve System SrCo6 O11. *Phys. Rev. Lett.* **114**, 236403 (2015).

197. Cai, X. *et al.* Atomically Thin CrCl3: An In-Plane Layered Antiferromagnetic Insulator. *Nano Lett.* **19**, 3993–3998 (2019).

198. Tsubokawa, I. On the Magnetic Properties of a CrBr3 Single Crystal. *J. Phys. Soc. Japan* **15**, 1664–1668 (1960).

199. Sato, K. Measurement of magneto-optical kerr effect using piezo-birefringent modulator. *Jpn. J. Appl. Phys.* **20**, 2403–2409 (1981).

200. Li, W. *et al.* Improved longitudinal magneto-optic Kerr effect signal contrast from nanomagnets with dielectric coatings. *Phys. Chem. Chem. Phys* **165**, 438–447 (1997).

201. Shcherbakov, D. *et al.* Raman Spectroscopy, Photocatalytic Degradation, and Stabilization of Atomically Thin Chromium Tri-iodide. *Nano Lett.* **18**, 4214–4219 (2018).

202. Huang, B. *et al.* Electrical control of 2D magnetism in bilayer CrI3. *Nat. Nanotechnol.* **13**, 544–548 (2018).

203. Zhong, D. *et al.* Van der Waals engineering of ferromagnetic semiconductor heterostructures for spin and valleytronics. *Sci. Adv.* **3**, 1–7 (2017).

204. Seyler, K. L. *et al.* Valley Manipulation by Optically Tuning the Magnetic Proximity Effect in WSe_2 /CrI_3 Heterostructures. *Nano Lett.* **18**, 3823–3828 (2018).

205. Wang, H., Eyert, V. & Schwingenschlögl, U. Electronic structure and magnetic ordering of the semiconducting chromium trihalides CrCl 3 , CrBr 3 , and CrI 3. *J . Phys . Condens . Matter* **23**, 116003–8 (2011).

206. Abramchuk, M. *et al.* Controlling Magnetic and Optical Properties of the van der Waals Crystal CrCl 3− x Br x via Mixed Halide Chemistry. *Adv. Mater.* **30**, 1801325 (2018).

207. Bertoldi, D. S., Bringa, E. M. & Miranda, E. N. Analytical solution of the mean field Ising model for finite systems. *J. Phys. Condens. Matter* **24**, 6 (2012).

208. Zhong, D. *et al.* Layer-resolved magnetic proximity effect in van der Waals heterostructures. *Nature Nanotechnology* **15**, 187–191 (2020).

209. Webster, L. & Yan, J. A. Strain-tunable magnetic anisotropy in monolayer CrCl3, CrBr3, and CrI3. *Phys. Rev. B* **98**, 144411 (2018).

210. Opilik, L., Schmid, T. & Zenobi, R. Modern Raman Imaging: Vibrational Spectroscopy on the Micrometer and Nanometer Scales. *Annu. Rev. Anal. Chem.* **6**, 379–398 (2013).

211. Song, T. *et al.* Switching 2D magnetic states via pressure tuning of layer stacking. *Nat. Mater.* **18**, 1298–1302 (2019).

212. Dietl, T. A ten-year perspective on dilute magnetic semiconductors and oxides. *Nature Materials* **9**, 965–974 (2010).

213. Spaldin, N. A. & Ramesh, R. Advances in magnetoelectric multiferroics. *Nature Materials* **18**, 203–212 (2019).

214. Hu, J. M., Duan, C. G., Nan, C. W. & Chen, L. Q. Understanding and designing magnetoelectric heterostructures guided by computation: Progresses, remaining questions, and perspectives. *npj Comput. Mater.* **3**, 18 (2017).

215. Barmawi, M. Spin injection using diluted magnetic semiconductor. in *International Conference on Instrumentation, Communication, Information Technology, and Biomedical Engineering 2009, ICICI-BME 2009* 45–49 (2009). doi:10.1109/ICICI-BME.2009.5417237

216. Saito, H., Yamagata, S. & Ando, K. Magnetoresistance in a room temperature ferromagnetic diluted magnetic semiconductor Zn1-xCrxTe. in *Journal of Applied Physics* **95**, 7175–7177 (American Institute of PhysicsAIP, 2004).

217. Bedair, S. M., Zavada, J. M. & El-Masry, N. Spintronic Memories to Revolutionize Data Storage. *IEEE Spectr.* 45–49 (2010).

218. Akimov, A. V., Yakovlev, D. R., Scherbakov, A. V. & Merkulov, I. A. Luminescence studies of spin dynamics in magnetic semiconductor nanostructures. *J. Lumin.* **125**, 1–10 (2007).

219. Dorokhin, M. V. *et al.* Spin injection of electrons in GaMnAs/GaAs/InGaAs light-emitting diode structures with a tunnel junction. *Tech. Phys.* **59**, 1839–1843 (2014).

220. Ananth, K. P., Gielisse, P. J. & Rockett, T. J. Synthesis and characterization of europium sulfide. *Mater. Res. Bull.* **9**, 1167–1171 (1974).

221. Hao, X., Moodera, J. S. & Meservey, R. Spin-filter effect of ferromagnetic europium sulfide tunnel barriers. *Phys. Rev. B* **42**, 8235–8243 (1990).

222. Hasegawa, Y. *et al.* Remarkable magneto-optical properties of europium selenide nanoparticles with wide energy gaps. *J. Am. Chem. Soc.* **130**, 5710–5715 (2008).

223. El Ghandoor, H., Zidan, H. M., Khalil, M. M. H. & Ismail, M. I. M. *Synthesis and Some Physical Properties of Magnetite (Fe 3 O 4) Nanoparticles*. *Int. J. Electrochem. Sci* **7**, (2012).

224. Munekata, H. *et al.* Diluted magnetic III-V semiconductors. *Phys. Rev. Lett.* **63**, 1849–1852 (1989).

225. Morkoc, H. & Ozgur, U. *ZnO-Based Dilute Magnetic Semiconductors, in Zinc Oxide: Fundamentals, Materials and Device Technology*. *Zinc Oxide* (Wiley, 2009). doi:10.1002/9783527623945.ch5

226. Misra, P. K. Semiconductors. in *Physics of Condensed Matter* 275–303 (Elsevier, 2012). doi:10.1016/B978-0-12-384954-0.00009-8

227. Bellingeri, E. *et al.* Influence of free charge carrier density on the magnetic behavior of (Zn,Co)O thin film studied by Field Effect modulation of magnetotransport. *Sci. Rep.* **9**, (2019).

228. Han, W. *et al.* Li(Cd,Mn)P: a new cadmium based diluted ferromagnetic semiconductor with independent spin & charge doping. *Sci. Rep.* **9**, 1–6 (2019).

229. Simserides, C., Majewski, J. A., Trohidou, K. N. & Dietl, T. Theory of ferromagnetism driven by superexchange in dilute magnetic semi-conductors. doi:10.1051/C

230. Katscher, H. & Hahn, H. Über Chalkogenidhalogenide des dreiwertigen Chroms. *Naturwissenschaften* **53**, 361 (1966).

231. Göser, O., Paul, W. & Kahle, H. G. Magnetic properties of CrSBr. *J. Magn. Magn. Mater.* **92**, 129–136 (1990).

232. Guo, Y., Zhang, Y., Yuan, S., Wang, B. & Wang, J. Chromium sulfide halide monolayers: Intrinsic ferromagnetic semiconductors with large spin polarization and high carrier mobility. *Nanoscale* **10**, 18036–18042 (2018).

233. Qi, J., Wang, H. & Qian, X. Electrically Tunable, High Curie Temperature 2D Ferromagnetism in Van der Waals Layered Crystals. (2018).

234. Lee, K. *et al.* Magnetic Order and Symmetry in the 2D Semiconductor CrSBr. (2020).

235. Telford, E. J. *et al.* Layered Antiferromagnetism Induces Large Negative Magnetoresistance in the van der Waals Semiconductor CrSBr. (2020).

236. Qiao, J., Kong, X., Hu, Z. X., Yang, F. & Ji, W. High-mobility transport anisotropy and linear dichroism in few-layer black phosphorus. *Nat. Commun.* **5**, 1–7 (2014).

237. Varshni, Y. P. Temperature dependence of the energy gap in semiconductors. *Physica* **34**, 149–154 (1967).

238. Ünlü, H. A thermodynamic model for determining pressure and temperature effects on the bandgap energies and other properties of some semiconductors. *Solid State Electron.* **35**, 1343–1352 (1992).

239. Wang, G. *et al.* Giant Enhancement of the Optical Second-Harmonic Emission of WSe2 Monolayers by Laser Excitation at Exciton Resonances. *Phys. Rev. Lett.* **114**, 097403 (2015).

240. Stier, A. V. *et al.* Magnetooptics of Exciton Rydberg States in a Monolayer Semiconductor. *Phys. Rev. Lett.* **120**, 057405 (2018).

241. Nagler, P. *et al.* Interlayer exciton dynamics in a dichalcogenide monolayer heterostructure. *2D Mater.* **4**, (2017).

242. Paudel, T. R. & Tsymbal, E. Y. Spin Filtering in CrI 3 Tunnel Junctions. *ACS Appl. Mater. Interfaces* **11**, 15781–15787 (2019).

Appendix A: The role of stamp geometry in van der Waals transfers

During the assembly of a multilayer van der Waals structure by mechanical transfer, in-plane strain on the sample is of particular concern as it could cause the layers to crack or shift relative to one another. The role of stamp geometry in producing (or minimizing) in-plane strains introduced by a van der Waals transfer is discussed below.

Consider a flat slab of elastic material being pressed into a rigid substrate at an angle θ along the z direction (fig. A1). The elastic slab must necessarily deform at the interface with the substrate if θ is fixed as they are brought further and further into contact. Assuming θ is small, the portion of the elastic material in contact with the substrate will be compressed along the z direction, nearly normal to the elastic slab. This will cause a corresponding *expansion* of the elastic in the x-y plane according to its tensor modulus ν_{ij}. Furthermore, the compressive strain will be nonuniform, being greatest at the lowest point of the elastic which made contact with the substrate first, decreasing linearly towards the contact point.

To simplify this model, we impose certain boundary conditions, marked by yellow dashed lines: first, that the top of the elastic is held rigidly (i.e. expansion along the top plane is forbidden); second, that the elastic is prohibited from slipping along the substrate in the region in which they have come into contact. Under these boundary conditions, the transverse strain caused by the compression will cause the material to bulge outward from the middle of the slab at the edge which first made contact, as both the top and the bottom of the slab are constrained here. On the opposite side of the contact region, the bottom surface of the elastic will be pushed away from the interface. These forces are indicated by red arrows. The latter strain, directed to the left in the diagram, is cumulative: When the elastic is first brought into contact, a small leftward strain is produced in the material adjacent to the contact point. When the elastic is lowered a bit more, this strain will be trapped in the newly contacted area (according to the second boundary conditions), and the strain in the material next to the *new* contact point will increase further due to the compression of the newly contacted area. Thus, as the two are brought further into contact, the transverse strain grows superlinearly from the original contact point up to the current contact point. The strain then decays to zero towards

the free edge of the elastic slab as it is unconstrained. The magnitude of the transverse strain *for a given contact length* is proportional to $\tan\theta$, as the contact length is given by $\Delta z \cot\theta$. Thus, if one's goal is to bring as much of the elastic into contact with the substrate while minimizing strain, a small contact angle is desirable.

However, if the surface of the elastic is rough, a sufficiently small contact angle will result in voids forming at the interface (fig. A2). If contact is made in a gas environment, gas will then become trapped in these voids to form pressurized bubbles. If the contact angle is sufficiently large, larger than the typical angular deviation of the surface topography of the elastic, the voids will be "squeezed out," resulting in fewer bubbles. Put another way, bubbles can only form where there is a local maximum in the separation between the elastic and the substrate, and by tilting the elastic, the separation can be made monotonic in x. Therefore, the requirements to produce a uniform interface and an unstrained interface are at odds with one another in this model of a van der Waals transfer.

One could of course perform a transfer using the edge of a stamp, i.e. pick up the 2D layers directly at the point where the stamp first meets the substrate to minimized strain despite a larger contact angle. There are practical limitations to this approach, though, namely poor visibility at the edge of the stamp, and the tendency for the PC membrane to relax near the edge of the PDMS block throughout a multi-step transfer, often resulting in the formation of small wrinkles in the PC. It is therefore desirable to do the transfer as close to the center of the stamp as possible. To this end, a domed stamp is beneficial: initial contact may be made in the center of the stamp, and the contact angle increases continuously away from the center. Since the contact angle is small (to vanishing) at the center, the transverse strain caused by initial contact is negligible; and since the transverse strain is cumulative and superlinear, reduction of the *initial* strain propagates throughout the contact process. Moreover, versus a flat slab in which the transverse strain is distributed along one axis (in fig. A1, the x axis), the transverse strain in a domed stamp is distributed along both the x and y axes and is thus overall reduced for a given contact area.

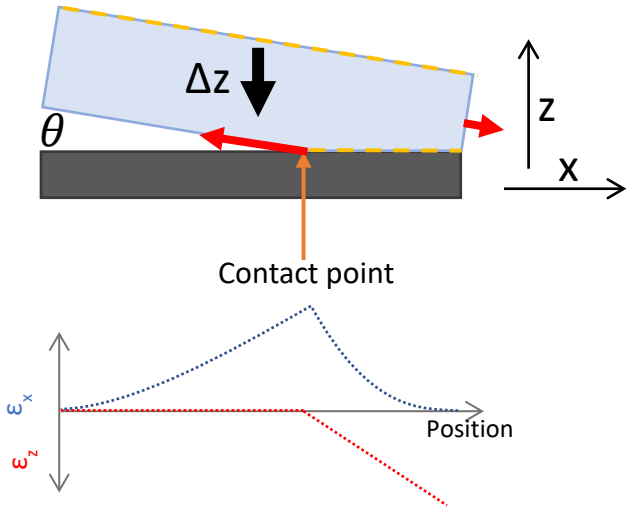

Figure A1 An elastic slab (blue) is brought into contact with a rigid substrate (gray) by pressing along the z direction, causing longitudinal and transverse strain (bottom)

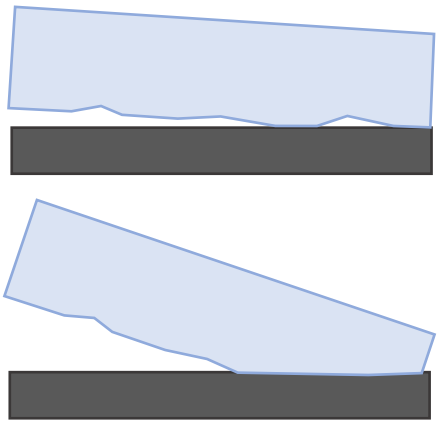

Figure A2 Contact angle plays a role in evening out roughness and reducing voids/bubbles in the interface.

Appendix B: Description of select experimental techniques

Description of magnetization measurements using magneto-optical effects

The magneto-optical Kerr effect (MOKE) and reflectance magneto-circular dichroism (RMCD) occur due to coupling the real and imaginary parts (respectively) of the off-diagonal terms of a material's polarizability tensor ε_{ij} $(i \neq j)$ and an incident optical field. They serve to retard or attenuate (respectively) one circularly polarized component of light relative to the other, resulting, for example, in the rotation of linearly polarized light or the conversion of linearly polarized light into elliptically polarized light (respectively). The off-diagonal elements of the polarizability vanish in an isotropic material and in the absence of broken time reversal symmetry; however, any type of spin or orbital polarization can cause these tensor elements to become nonzero. Thus, if linearly polarized light passes through a spin-polarized or magnetized material *parallel to the polarization/magnetization vector*, it may undergo rotation (the Faraday effect) or acquire elliptical polarization (magneto-circular dichroism). Light which reflects off the material may be rotated as well (MOKE) or acquire elliptical polarization (RMCD). These two polarization effects may therefore be used as probes of a material's spin polarization or magnetization.

A sensitive technique for measuring MOKE and RMCD has been described by Sato[199], which makes use of polarization modulation and lock-in amplification to make possible the measurement of very small Kerr rotation angles and small degrees of ellipticity. Polarization modulation is carried out by means of a photoelastic modulator (PEM), in which an isotropic slab of refractive medium is made *anisotropic* by a time-varying uniaxial strain produced by a piezoelectric transducer. The amplitude of the strain can be varied by adjusting the driving amplitude of the transducer, while the modulation frequency Ω is fixed by the mechanical resonance of the refractive slab. Defining the strain axis as $\hat{x}$, collimated monochromatic light is transmitted through the PEM along the $\hat{z}$ direction with polarization along the $\hat{D} = (\hat{x} + \hat{y})/\sqrt{2}$ direction. The refractive index of the refractive slab is $\vec{n} = n_0\hat{y} + n_0\hat{z} + (n_0 + \Delta n \sin(\Omega t))\hat{x}$. As a result, a time-varying retardance is imprinted on the $\hat{x}$ component of the polarization (relative to the $\hat{y}$ component) which is proportional to $d\Delta n$, where d is the thickness of the slab along the

optical axis. Δn is tuned such that a particular retardance, in this case $\lambda/4$, is achieved. As a result, the polarization of the outgoing light will be modulated such that it is $\widehat{D}$ polarized (unmodulated) at the strain nodes and circularly polarized with opposite helicities ($\widehat{+}$ and $\widehat{-}$) at the positive and negative strain antinodes. Thus, during each modulation cycle, the light takes on $\widehat{D}$ polarization twice and $\widehat{+}$ and $\widehat{-}$ once each.

The modulated light is then directed toward an objective lens which focuses it onto the sample. Upon reflection, MOKE and RMCD act on the light's polarization state. The reflected light is then recollimated by the objective lens and split off from the ingoing light by a beamsplitter before being directed through a linear polarizer and onto a photodiode. The key to this technique is that the Kerr effect does not affect circularly polarized light, while circular dichroism does not cause the major axis of polarization to rotate (even if it causes linearly polarized light to become elliptical). Consequently, if the light is subject only to MOKE, only the $\widehat{D}$ portion of the polarization modulation cycle will be affected, and since $\widehat{D}$ polarization is achieved twice per cycle, MOKE will affect the light polarization at a frequency of 2Ω. On the other hand, RMCD will enhance reflectance for $\widehat{+}$ while reducing it for $\widehat{-}$ (or vice versa for opposite magnetic polarization). Thus RMCD produces a modulation of the reflected intensity with a one maximum per modulation period and one minimum per modulation period, rendering an oscillating signal at Ω. Strictly speaking, the polarizer is not necessary for RMCD as it produces a time-oscillating intensity in the modulated beam. The polarizer *is* necessary for measuring MOKE; it should be oriented along the $\hat{x}$ or $\hat{y}$ directions. Thus, as $\widehat{D}$ polarized light passes through the analyzer, the intensity will be reduced by $\sin \pi/4$. The same reduction applies to both circular polarizations of light. However, when the $\widehat{D}$ light is rotated by an angle θ_K, the intensity is reduced by $\sin(\pi/4 + \theta_K)$ when it passes through the polarizer, hence converting the Kerr rotation signal from a polarization effect to an intensity effect, which can be read off by the photodiode. The two effects can therefore be distinguished from one another by means of a lock-in amplifier tuned either to Ω for RMCD or 2Ω for MOKE.

Description of Raman scattering spectroscopy

Phonons are quantized lattice vibrations in molecular matter. Certain vibrational normal modes in matter can produce an electric dipole moment and are called optical phonons (as compared to acoustic phonons, which do not produce an electric dipole moment). Raman scattering occurs when a photon incident on matter excites a virtual electronic state, which can either absorb or emit an optical phonon by coupling to its electromagnetic field. When the virtual state decays, light is emitted with an energy that has increased (phonon absorption) or decreased (phonon emission). At low temperatures, the phonon population is low, and thus phonon absorption is much less likely than phonon emission. The typical energies of optical phonons in crystalline solids range from a few meV to tens of meV. Thus, spectroscopic measurement of Raman scattering, or Raman scattering spectroscopy, benefits from the use of narrowband single-frequency light in order to spectrally separate the Raman modes from the un-scattered light. This is typically accomplished by using an interference filter such as a Fabry-Perot interferometer, etalon, multilayered dielectric filter, or Bragg filter.

In our case, a series of Bragg filters are needed for the following reason: The strength of Raman scattering is directly proportional to the interaction length of the light with the material being studied. In atomically thin samples, the interaction length is necessarily very small, and thus the Raman scattering is weak. Thus, laser sidebands must and unscattered light must be suppressed to a high degree in order to resolve the weak Raman signal.

Laser light from a 633 nm HeNe laser or a 532 nm diode pumped solid state laser are employed. First, the light is reflected off a Bragg reflective bandpass filter, tuned to the Bragg angle corresponding to the laser line such that the reflected power is maximized and sidebands are suppressed by a factor of 10^4. The light is then reflected off a Bragg notch filter, again tuned to the laser line, before being sent to an objective lens to be focused onto the sample. Upon reflection, Raman scattering occurs. The objective lens recollimates the reflected light which then intercepts the aforementioned Bragg notch filter. At this point, the unscattered laser light is rejected by the notch filter with a rejection ratio of 10^4 and the Raman scattered light passes through. However, at this point, the amount of laser light overwhelms the Raman scattered light and will overwhelm any detector which is sensitive enough to detect the weak Raman signal.

Therefore, the light is passed through another pair of Bragg notch filters to extinguish the unscattered light by an additional factor of 10^8 total. Thus, the laser sidebands undergo a total suppression of 10^8 before reaching the sample, and the unscattered light undergoes a total suppression of 10^{12} before reaching the spectrometer/detector. The Raman spectrum is then analyzed by dispersal in a high-resolution spectrometer (500 mm focal length, 1200 or 1800 lines/mm diffraction grating in Czerny-Turner geometry).

Appendix C: Supplementary data

Supplementary data for chapter 5

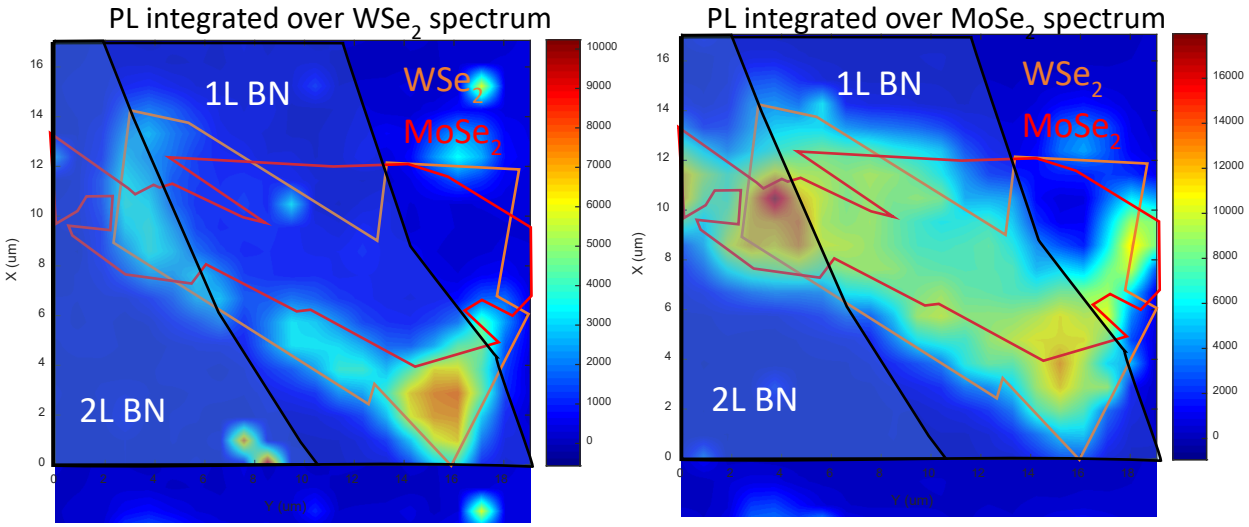

(Left) photoluminescence map of FHBL-4 integrated from 700-720 nm (over the WSe_2 neutral exciton). (Right) photoluminescence map of FHBL-4 integrated from 750-765 nm (over the $MoSe_2$ neutral exciton).

Supplementary data for chapter 7

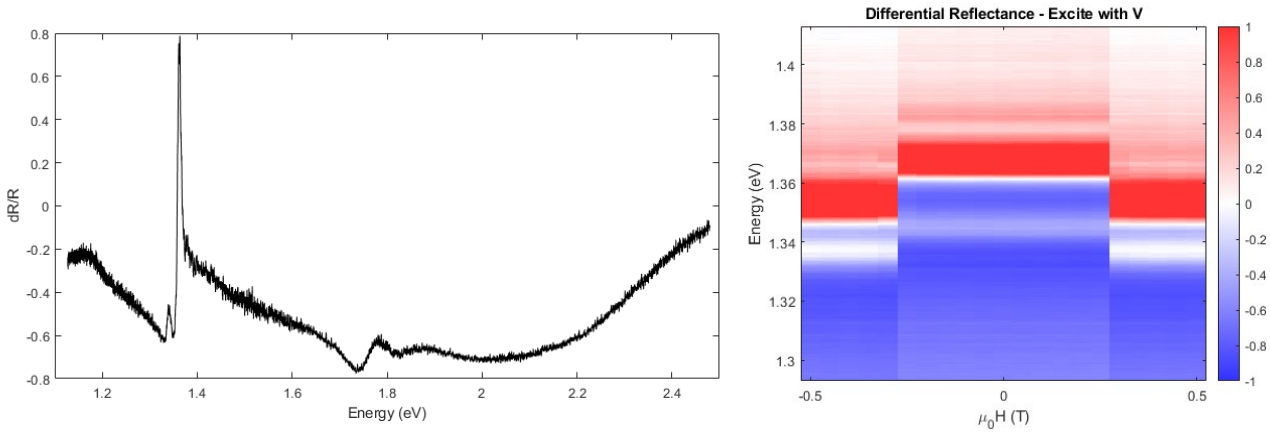

(left) Differential reflectance spectrum of 5L CrSBr at 5K and B=0 using light polarized along the **b** direction. (right) Magnetic field dependence of differential reflectance, with field swept along magnetic easy axis.

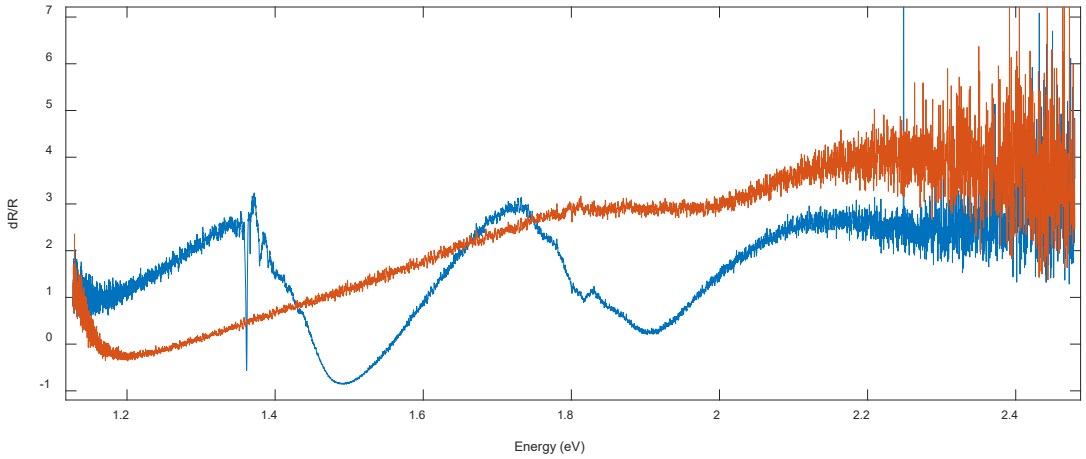

(left) Differential reflectance spectrum of bulk exfoliated CrSBr at 5K and B=0 using light polarized along the **a** (orange) and **b** (blue) direction.

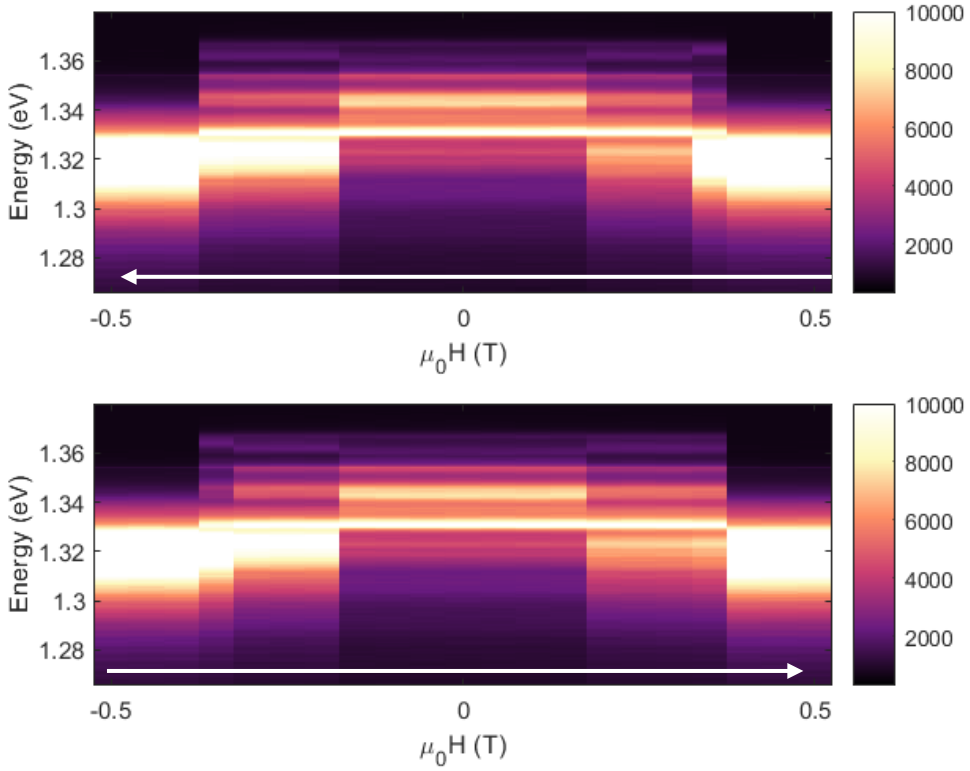

Magneto-photoluminescence spectrum of bulk CrSBr at 5K with the magnetic field swept along the easy axis. Bidirection sweep reveals hysteretic behavior.